10-31-2013

MRI Characterization of Radiation Necrosis in an Animal Model: Time to Onset, Progression, and Therapeutic Response

Xiaoyu Jiang
Washington University in St. Louis

Recommended Citation

Jiang, Xiaoyu, "MRI Characterization of Radiation Necrosis in an Animal Model: Time to Onset, Progression, and Therapeutic Response" (2013). *All Theses and Dissertations (ETDs)*. 1186.
https://openscholarship.wustl.edu/etd/1186

WASHINGTON UNIVERSITY IN ST. LOUIS

Department of Chemistry

Dissertation Examination Committee:

Joseph J.H. Ackerman, Chair
Joel R. Garbow
Dennis E. Hallahan
Joshua Maurer
Demetrios Sarantites
Joseph R. Simpson
John-Stephen Taylor

MRI Characterization of Radiation Necrosis in an Animal Model: Time to Onset, Progression, and Therapeutic Response

By

Xiaoyu Jiang

A dissertation presented to the
Graduate School of Arts and Sciences
of Washington University in
partial fulfillment of the
requirements for the degree
of Doctor of Philosophy

December 2013
St. Louis, Missouri

Table of Contents

Acknowledgement

I thank my two advisors, Prof. Joseph J. H. Ackerman and Prof. Joel R. Garbow, for their guidance and support during this thesis research and graduate study at Washington University. They provided expert direction, a state-of-art research environment and the ability to work with distinguished collaborators. Thanks to Prof. Dmitriy A. Yablonskiy and Dr. Alexander L. Sukstanskii, for their help in qBOLD study and data analysis. Thanks to John A. Engelbach for his help in animal operations. My thanks are extended to those members, both current and past, of the Biomedical Magnetic Resonance Laboratory at Washington University in St. Louis: Xiaoqi Wang, Donghan Yang, Chong Duan, Jeff R. Anderson, Kathleen E. Chaffee, Carlos Perez-Torres, Scott Beeman.

I also thank my collaborators: Dr. Liya Yuan, Jeremy Cates, Dr. Feng Gao, Dr. Robert E. Drzymala, Dr. Keith M. Rich and Dr. Dinesh Thotala.

This thesis research has been supported by NIH grants R01 CA155365 (JRG), R01 CA174966 (DEH), and R01 CA140220-01 (DEH), and funding from the Alvin J. Siteman Cancer Center, an NCI-comprehensive cancer center, P30 CA091842, the Barnes-Jewish Hospital Foundation Cancer Frontier Fund, and Elekta Instruments AB (Stockholm, Sweden). I gratefully acknowledge Genentech (South San Francisco, CA) for donation of anti-VEGF antibody B20-4.1.1.

I thank my Dissertation Advisory and Examination Committee members, Prof. Joseph J.H. Ackerman, Prof. Joel R. Garbow, Prof. Joshua Maurer, Prof. John-Stephen Taylor, Prof. Demetrios Sarantites, Prof. Joseph R. Simpson, and Prof. Dennis E. Hallahan.

Lastly a lot of thanks to my parents for their continued support, love, and encouragement

throughout my graduate study. Many thanks to my wife for her fabulous cooking skills and my 20-month old daughter for her lovely smile.

Xiaoyu Jiang
Washington University in St. Louis
August 2013

ABSTRACT OF THE DISSERTATION

MRI characterization of radiation necrosis in an animal model: time to onset, progression, and therapeutic response

By

Xiaoyu Jiang

Doctor of Philosophy in Chemistry

Washington University in St. Louis, 2013

Professor Joseph Ackerman, Chair

Radiation necrosis is a severe, but late occurring type of injury to normal tissue, within and surrounding a radiation treatment field, which can lead to significant complications for neurooncology patients. Radiation necrosis is difficult to distinguish from recurrent tumor by either neurologic examination or clinical imaging protocols. Concerns for the development of radiation necrosis often limit therapeutic radiation doses. Current treatment options for radiation necrosis are limited. The development of solutions to these clinical challenges has been hampered by an appropriate animal model of radiation necrosis.

With a novel mouse model of radiation necrosis developed in our lab employing a Gamma Knife, which enables high-dose, fractionated, hemispherical irradiation in the mouse brain, the objectives were to i) optimise radiation dosing schemes (total dose, fractionation) for this Gamma-Knife mouse-model of radiation necrosis; ii) determine the efficacy of bevacizumab (Avastin) and its murine analog B20-4.1.1, both vascular endothelial growth factor (VEGF) inhibitors, as mitigators of radiation necrosis in mice; iii) validate the neuroprotective effect of SB 415286, an inhibitor of glycogen synthase kinase 3β (GSK-3β□), in mouse brain following

high-dose radiation treatment; and iv) identify and validate the quantitative blood oxygen level dependent (qBOLD) method as an imaging marker of radiation necrosis.

For these purposes, a series of experiments were performed, including monitoring the onset and progression of radiation necrosis in mice receiving different dose schedules, comparing the development of radiation necrosis in irradiated mice with or without treatments, and mapping the irradiated and non-irradiated mouse brains using qBOLD method.

It was found that i) radiation dose schedules affect the onset and progression of radiation necrosis; ii) anti-VEGF antibodies slow the progression of radiation necrosis in irradiated brain tissue; iii) SB 415286 protects against and mitigates radiation necrosis in irradiated brain tissue; and iv) a high SNR (400 at least) is required to decouple oxygen extraction fraction (OEF) and deoxyhemoglombin cerebral blood volume (dCBV) in mouse brain using qBOLD method. In qBOLD, the voxel spread function (VSF) reduces the effect of macroscopic magnetic field inhomogeneities. However, with current shimming methods, imaging parameters, and post-processing algorithms, the resulting OEF and dCBV maps in the mouse brain are not reliable.

These results demonstrated that the development of radiation necrosis in this Gamma Knife mouse model can be characterized by both anatomic MR imaging and histology. Both anti-VEGF therapy and GSK-3β inhibition could be potential therapeutic managements for radiation necrosis, but further studies are needed to optimize dosing schemes and treatment periods and elucidate mechanisms of action. Characterizing radiation necrosis in mouse brain using qBOLD remains a challenge due to the imperfect correction for macro magnetic field inhomogeneities.

Chapter 1 Introduction

1.1 Motivation

Radiotherapy is the most efficient treatment for curing or mitigating malignant tumors with approximately 50% of all cancer patients receiving radiation therapy during their course of illness. However, despite the use of sophisticated, fractionated, high-dose radiation or radiosurgery methods designed to spare normal tissue, about 20% of patients experience radiation necrosis (RN) three or more months following therapy. Further, the presence of RN complicates/masks the identification/diagnosis of recurrent tumor. To date, no single imaging modality has been shown to reliably distinguish RN from recurrent tumor and no standard therapy has been shown to protect against, or effectively mitigate, RN [1]. Identification of necrosis and development of therapeutics to treat necrosis are challenging clinical problems. The development of solutions to these critical clinical challenges has been hampered by the lack of a well-developed, small-animal model of RN. A Gamma-Knife mouse-model of RN, in concert with MRI monitoring, provides a powerful and translatable platform to i) elucidate the critical determinants governing the onset and progression of injury; ii) evaluate neuroprotective/mitigative agents; and iii) define the MR signatures distinguishing necrosis from recurrent tumor.

1.2 State of Research

1.2.1 Radiation necrosis following radiation treatment of central nervous system

Radiation is a key component in the treatment of both benign and malignant central nervous system (CNS) tumors, including gliomas, metastases, meningiomas, schwanomas, pituitary adenomas, and other less common neoplasms. Multiple radiation-treatment schemes have been developed to treat various neoplasms in the brain. These treatment protocols utilize a variety of different fractionation and conformational schemes designed to deliver focused radiation to regions in the brain to maximize control of tumor growth and minimize deleterious effects on normal brain tissue. Outcomes of these clinical protocols may be complicated by radiation-induced injury on non-neoplastic tissue. Based on the time of clinical expression, radiation-induced injury is described as 'acute', 'early delayed' or 'late delayed injury' [2]. Acute injury, occurring in days to weeks after irradiation, is rare with current radiation therapy techniques. Early delayed injury occurs 1–6 months post-irradiation and can involve transient demyelination with somnolence. Although both of these early injuries can produce severe reactions, they are normally reversible and resolve spontaneously. In contrast, late delayed injury, characterized histopathologically by vascular abnormalities, demyelization, and ultimately white matter necrosis, is usually observed more than 6 months post irradiation. These delayed effects from radiation are generally considered as irreversible and progressive. They may produce cerebral edema and necrosis of normal brain parenchyma, resulting in untoward neurologic effects that are difficult to differentiate from recurrent tumor growth.

Radiation necrosis (RN), a delayed radiation injury that can occur after radiation treatment of the CNS, can develop between 3 months and 10 years after radiotherapy, with most cases occurring in the first two years. Necrosis following radiation is not uncommon, occurring in 3-24% of patients receiving focal irradiation. Several studies have suggested a direct relationship between radiation-induced injury and different radiation doses, fractionation schemes, and adjuvant treatments. Total radiation dose was determined to be the most important risk factor. In cases where fractionated therapy is used, larger fractional doses are more likely to cause subsequent RN. The incidence of RN may be threefold higher with concurrent chemotherapy [3]. Other risk factors include lesion volume and location, old age, and vascular risk factors, including diabetes.

1.2.1.1 Pathobiology of radiation necrosis

The biology of RN is poorly understood. Two mechanisms have been proposed to explain cerebral RN: the glial injury hypothesis and the vascular injury hypothesis [4].

The glial injury hypothesis

The glial injury hypothesis initially focused on oligodendrocytes, which are required for the formation of myelin sheaths. Oligodendrocyte type-2 astrocyte (O-2A) progenitor cells, the key cells for generating mature oligodendrocytes, lose their reproductive capacity after whole brain irradiation in the rat, ultimately leading to a failure to replace oligodendrocytes. But the hypothesis that oligodendrocytes depletion results in demyelination and white matter necrosis, is questionable. It has been reported that no changes in the number of myelinated axons, the thickness of myelin sheaths, and the cross-sectional area of myelinated axons have been measured in cognitively impaired rats 12 months post irradiation [7]. In addition, although the kinetics of oligodendrocyte depletion is consistent with an early transient demyelination, it is inconsistent with the late onset of white matter necrosis. Thus, the relationship between radiation damage to oligodendrocytes and late radiation-induced injury is still unclear.

Astrocytes, constituting approximately 50% of the total glial cell population in the brain, are recognized as a heterogeneous class of cells that perform diverse functions, including biochemical support of endothelial cells that form the blood-brain barrier (BBB), provision of nutrients to the nervous tissue, maintenance of extracellular ion balance, and a role in the repair and scarring process of the brain and spinal cord following traumatic injuries. In response to radiation injury, astrocytes undergo proliferation and exhibit hypertrophic nuclei/cell bodies. These reactive astrocytes produce vascular endothelial growth factor (VEGF) and hypoxia-inducible factor 1α (HIF-1α), which also potentiates the upregulation of VEGF [5]. As a result of VEGF upregulation, BBB dysfunction becomes worse and increases cerebral edema and hypoxia [6]. Although, their exact role in the overall pathogenesis of late delayed radiation-induced brain injury is still unclear, astrocytes likely contribute by interacting with both vascular and other parenchymal elements in the brain.

Microglia, representing 10-15% of the total glial cell population within the brain, act as the first and main form of active immune defense in the CNS. After injury, microglia become activated, a process characterized by rounding of the cell body, retraction of cell processes, proliferation, and increased production of reactive oxygen species, cytokines, and chemokines that mediate neuroinflammation [7]. Radiation-induced microglia activation plays an important role in the formation of RN. An increased percentage of activated microglia has been detected in the irradiated rat brain before the expression of late radiation-induced brain injury [8]. Anti-inflammatory agents, such as ramipril and indomethacin, reduce the number of activated microglia in the hippocampus and/or perirhinal cortex and prevent radiation-induced cognitive impairment in rodents [9]. However, there is evidence that the reduction of radiation-induced brain injury is not necessarily associated with the change in number of activated microglia. The anti-inflammatory agent, L-158, 809, has no effect on microglial activation, but still prevents radiation-induced cognitive impairment [10]. Orthotopic injections of fetal neuronal stem cells that form new neurons without affecting the number of activated microglia reverse radiation-induced cognitive impairment in rodents [11]. Thus, the exact role that activated microglia play in generating late delayed radiation-induced brain injury, including cognitive impairment, is still an open question.

The vascular injury hypothesis

It has been suggested that vascular damage leads to ischemia and, secondarily, to white matter necrosis. Many studies have reported radiation-induced vascular structural changes, including vessel wall thickening, vessel dilation, and endothelial cell nuclear enlargement [12, 13]. Quantitative studies in irradiated rat brains have also demonstrated time- and dose-dependent reductions in the number of endothelial cell nuclei, blood vessel density, and blood vessel length [12, 14]. Moreover, white matter necrosis occurs in boron neutron capture studies where nearly all of the radiation damage is to the vasculature [15]. In contrast, radiation-induced necrosis has been reported in the absence of vascular changes [13]. Also, the PPARγ agonist, pioglitazone, and the ACE inhibitor, ramipril, which prevent radiation-induced cognitive impairment in the rat, do not reverse the reduction in vascular density and length that occurs after radiation treatment. Consequently, vascular damage is not the only contributor to the late delayed radiation-induced injury.

To sum, there is no single cell or tissue associated with either the glial or vascular injury hypotheses that can fully explain the development of RN. The late delayed radiation-induced injury is more likely developed due to dynamic interactions between the multiple cell types in the brain [16]. Vascular endothelial cells, oligodendrocytes, astrocytes, microglia, and neurons are all actively involved in the development of RN that, theoretically, allow one to change the response/outcome by intervening at numerous points in the process to prevent or ameliorate the development of RN.

1.2.1.2 Diagnosis of radiation necrosis

The clinical presentation and radiological appearance of radiation necrosis is remarkably similar to that of recurrent tumor. Distinguishing between these two clinical different entities is a significant challenge for treating physicians. Various imaging techniques have been investigated for differentiation of recurrent tumor and necrosis. The following is a discussion of the imaging modalities utilized to diagnosis RN.

Conventional MRI

Conventional, anatomic MRI, refers to T_1-weighted post-gadolinium enhanced imaging and T_2-weighted/fluid-attenuated inversion recovery (FLAIR) imaging. Details about these two methods will be provided later. T_1-weighted post-gadolinium enhanced imaging is a non-specific biomarker of BBB breakdown, which can result from post-operative inflammation, seizures, tumor recurrence, radiation necrosis or other adjuvant treatment effects. The enhancement on T_2-weighted image is associated with increased water content in tissues, and can result from necrosis or recurrent tumor. Some studies have suggested that the pattern of the enhancement may aid in the differentiation between necrosis and recurrent tumor. The morphologic features of enhancement such as Swiss cheese and soap bubble enhancement have been suggested to be more consistent with radiation necrosis [17]. In addition, a combination of lesion multiplicity, corpus callosum invasion, and sub-ependymal spread has been noted to be correlated with tumor recurrence [18]. The lesion quotient, which is the ratio of the lesion area on T_2-weighted image divided by the total area of enhancement on contrast-enhanced T_1-weighted image, has been reported to separate tumor from necrosis [19]. Although these finding may improve the diagnostic accuracy, the limitation of diagnosis based solely on conventional MRI is well documented [20].

Diffusion weighted imaging and (DWI) and diffusion tensor imaging (DTI)

In biological tissue, structural barriers such as cell membranes and myelin can restrict the mobility of water molecules or favor the movement of water molecules in a specific direction. The magnitude and direction of free water movement are quantified with DWI and DTI, respectively, by calculating apparent diffusion coefficient (ADC) for magnitude and fractional/relative anisotropy for direction [21]. Recurrent tumor often has high cellularity, which slows the movement of water molecules (decreased ADC), while necrosis exhibits region of low cellularity and, consequently, increased ADC. Several small cohort studies showed the potential of ADC measurement for differentiating between tumor and necrosis [22-24]. But the presence of edema, which has a high ADC, in both lesions complicates the use of diffusion measurements [25, 26]. Further, primary malignant brain tumors usually show lower cellularity and, consequently, larger ADC than normal tissue. The sensitivity and specificity of DWI and DTI need to be more fully characterized.

MR perfusion imaging

Perfusion-weighted MRI measures perfusion, including blood flow and relative cerebral blood volume (rCBV) [27]. As a result of increased metabolic activity and angiogenesis due to upregulation of VEGF, hyperperfusion is usually seen with recurrent tumor [28, 29]. In contrast, CBV decreases in necrotic regions due to occlusive vasculopathy [30]. A prospective study of 20 patients indicated that an enhancing lesion with a normalized rCBV ratio lower than 0.6 is suggestive of radiation necrosis, and an rCBV value higher than 2.6 suggests tumor recurrence [31]. When the normalized rCBV ratio is between 0.6 and 2.6, perfusion imaging does not have sufficient sensitivity and specificity to distinguish tumor from necrosis. However, a fast growing tumor could exceed its blood supply and result in a state of hypoperfusion. Also, it is hard to estimate the perfusion in a mixed necrosis/tumor region [32]. Further, anti-angiogenesis therapy, a commonly used tumor treatment [33], can change the perfusion in tissue, thereby complicating the interpretation of the results from perfusion-weighted MRI.

Magnetic resonance spectroscopy (MRS)

Proton MR spectroscopy determines the metabolic profile in tissue and has been widely investigated for differentiation between recurrent tumor and radiation necrosis [34-37]. It has been suggested that a low concentration of creatine (Cr) in tissue is more likely correlated to radiation necrosis, while a high concentration of choline (Cho) is associated with tumor progression [38-40]. As a result, the ratio of Cho and Cr provides a useful variable for recurrent tumor diagnosis with high sensitivity and high specificity. However, these studies are all human studies and limited by the lack of histology confirmation. The relatively low spatial resolution for the current MRS imaging is also a shortcoming, especially for cases of heterogeneous lesions consisting of both tumor and necrosis [36].

Molecular MR imaging

Amide proton transfer (APT) imaging, a specific chemical exchange-based saturation transfer MRI technique, which can be used to detect the amide protons of endogenous, low-concentration mobile proteins and peptides in tissue, has been utilized to differentiate radiation necrosis from recurrent tumor [41]. The APT imaging signal in tissue is primarily related to two factors: the mobile amide proton content and the amide proton exchange rate. Tumors have a higher cellular content of proteins and peptides than normal tissue, showing hyperintensities on APT images. Radiation necrosis, conversely, exhibits the loss of mobile cytosolic proteins and peptides, showing hypointensities on APT images. APT imaging has been limited by its poor multi-slice capability, with single slice imaging being used in most of the APT studies.

Computerized tomography (CT)

CT is a conventional imaging technique, available at most hospitals, and CT scans are easy to perform. But CT scans rarely distinguish between recurrent tumor and RN [42]. Both types of lesions are typically hypo or iso-intense to brain on non-contrasted CT images. With administration of contrast, the solid component of the lesion will generally be enhanced [43, 44].

Nuclear medicine scans

Both SPECT and PET have been utilized for differentiating between recurrent tumor and necrosis in many patients. SPECT scans use radionuclide tracers to assess lesions for their degree of metabolic activity indirectly by measuring uptake of a specific tracer within the tissue, which is elevated in metabolically active cells, including inflammatory and tumor cells. Increased uptake also tends to indicate increased cellularity. Necrosis has no significant metabolic activity and should have minimal or no radiotracer uptake [45]. Thallium-201 has been reported to evaluate the degree of malignancy or cellular activity quantitatively within the region of interest [46]. Various other radiotracers have been investigated, including 99mTc-hexamethy-propylene-amine oxime (99mTc-HMPAO), and 99mTc-sestamibi. Using SPECT, several groups have reported sensitivity of more than 90% in the detection of tumor recurrence, but with specificities closer to 60% [47]. Reports of patients with thallium-avid cerebral RN raise questions about the clinical utility of these techniques [48, 49]. PET can be used to measure glucose metabolism within the brain, using an 18F analog such as fluorine-18 fluorodeoxyglucose (18F-FDG). RN should characteristically have low glucose consumption because of the absence of metabolically active cells. A near 100% accuracy in a large series of glioma patients has been reported using 18F-FDG PET scans [50, 51]. Various other investigators have shown less robust sensitivities of 85% and specificities of 80% [52-54]. However, these results lacked histopathological validation.

1.2.1.3 Management of radiation necrosis

Clinicians have had few options for therapeutic invention when patients develop symptomatic radiation necrosis. The following is a discussion of the current managements used to mitigate/protect against RN.

Medical treatment

Corticosteroids play a significant role in the medical management of radiation necrosis by counteracting the radiation-induced vascular endothelial damage and suppressing inflammation [55]. However, prolonged treatment with corticosteroids is often employed, and is complicated by Cushingnoid side-effects, including weight gain, myopathy, immunosuppression, psychiatric disturbances, and occasionally arthritic sequelae, such as avascular necrosis affecting the shoulders and hips [56].

Hyperbaric oxygen (HBO) treatment has also been considered as a therapeutic modality. It involves breathing pure oxygen that has been pressurized at 2-3 times normal atmospheric pressure. The tissue oxygen pressure increases under these conditions, which potentiates angiogenesis, fibroblast and osteoblast proliferation, and collagen formation. The benefit of HBO in the treatment of RN has been reported in several reports [57-59]. But most of these studies are small, retrospective, and most patients received steroids concurrently [57, 58]. In addition, HBO is cumbersome to deliver, expensive, and available in only a few medical centers.

Bevacizumab, a humanized monoclonal antibody against VEGF [60], has been reported to substantially decrease the effects of radiation necrosis [61-64]. A recent randomized double-blind study of bevacizumab therapy for the patients with radiation necrosis provided evidence of its efficacy in mitigating radiation necrosis [64]. However, these studies relied on MR imaging, and, in particular, T1 post-gadolinium enhancement to characterize radiation necrosis, which is complicated by the presence of recurrent tumor. Also, because it is generally not possible to correlate time-course MR observations with histologic findings in patients, these human studies lack information regarding the mechanism of action of bevacizumab. Thus, further studies are needed to validate the effects and mechanisms of bevacizumab in the treatment of radiation necrosis.

Surgical management

Surgical resection of necrotic tissue reduces mass effect, edema and lowers intracranial pressure, resulting in lasting clinical improvement in the majority of patients. Although it is the only definitive treatment of brain necrosis, it is often not possible due to the location of the necrosis in eloquent regions of the brain.

Laser interstitial thermal therapy (LITT)

As discussed in section 1.2.1.1, upregulation of VEGF likely plays an important role in the development of RN. It has been suggested that the perinecrotic region of gliosis is responsible for most of the VEGF release. As a result, targeting this gliotic region with LITT can remove most of the active VEGF and replace these lesions with a region of inactive, factor-depleted coagulative necrosis. A recent study demonstrated the possibility of using LITT to safely treat a patient with cerebral RN [65].

1.2.2 Magnetic Resonance Imaging (MRI) in characterizing radiation necrosis

MRI is a medical imaging technique used extensively to visualize detailed internal structures of the body. It makes use of the property of nuclear magnetic resonance (NMR) to image nuclei of atoms inside the body. MRI provides excellent contrast between the different soft tissues of the body, which makes it especially useful in monitoring the brain, muscle, the heart, and cancers, compared with other imaging modalities such as CT and x-ray imaging. The following introduces the basic working theory of MRI and all the MR methods used in my PhD research. A more detailed discussion of the content of section 1.2.2.1 can be found in most classical textbooks on the subject [66, 67].

1.2.2.1 Introduction to MRI basics

Nuclear spin

Spin is a form of angular momentum. However, it is not produced by a rotation of the particle, but is an intrinsic property of the particle itself. The spin angular momentum S of any physical system and the component of S measured along any direction are:

$$S = \frac{h}{4\pi}\sqrt{s(s+1)}$$
$$S_i = \frac{h}{2\pi} s_i, s_i \in \{-s, -s+1, \ldots, s-1, s\}$$

Where h is Planck's constant and s is the spin quantum number. The spin quantum number takes values of the form N/2, where N can be any non-negative integer. The spin quantum number of protons, the most common signal source in MRI experiment, is 1/2.

Particles with spin possess an intrinsic magnetic moment. The magnetic moment is proportional to the spin angular momentum:

$$\mu = \gamma S$$

For atomic nuclei, the proportionality constant γ is called the gyromagnetic ratio. The magnetic energy of an object depends on the interaction between its magnetic moment and the external magnetic field:

$$E = -\vec{\mu} \bullet \vec{B}$$

Assuming that the external magnetic field B is applied along z direction, the magnetic energy of spin-1/2 nuclei can be simplified as:

$$E = -\gamma S_z B_z = \pm \frac{h}{4\pi} \gamma B_z$$

There are two energy states, one representing alignment parallel to the field, another anti-parallel. According to Boltzmann statistics, the population ratio of the two states is determined by:

$$\frac{Population(anti - parallel)}{Population(parallel)} = \exp(-\frac{\Delta E}{kT}) = \exp(-\frac{h\gamma B_z}{2\pi kT})$$

Where k is the Boltzmann constant and T is the absolute temperature. The spin population difference between two energy states generates a net magnetization parallel to the field, which is the source of MR signal. With the common temperature in biological tissues and currently available magnets, this population difference is extremely small—on the order of 1 in a million spins. Fortunately, the human body is made up of approximately 60% water and each molecule of water (H_2O) contains two hydrogen atoms. These hydrogen atoms provide a sufficient signal to enable MRI experiments.

Free induction decay

Spin is a quantum-mechanical property. However, for describing the mechanism of MR signal generation, it is often convenient to consider the analogue of spin in classical physics. Just as a spinning top processes around the gravitational field, nuclear spin precesses about the axis of the external magnetic field B_0. The precession frequency is $\omega_0=\gamma B_0$, also known as the Larmor Frequency.

In the presence of an external magnetic field B_0, nuclear spins at equilibrium produce a net magnetization M_0 along the B_0 field (Z direction). In MR, the detectors are only able to measure magnetization processing in the plane perpendicular to the static magnetic field.

An electromagnetic radio frequency (RF) pulse in the XY plane is applied at or near the Larmor Frequency to nutate the net magnetization towards the XY plane. At the quantum level, nuclear spins absorb the RF energy and transition to the higher energy state. Once the RF pulse is turned off, three things begin to happen simultaneously:

1. The magnetization in the XY plane continues to precess in transverse plane around the B_0 field, and induces an oscillating electric current in the wire, which can be picked up by a receiver coil and becomes NMR signal, also known as free induction decay, or FID.
2. The energy absorbed by the excited spins is released back into the surrounding lattice (spin-lattice relaxation), reestablishing thermal equilibrium. In the classical description, the Z component of the magnetization (M_z) grows back to M_0. The time course of spin-lattice relaxation can often be described by an exponential curve. The recovery rate is characterized by the relaxation time constant T_1, which is unique to every tissue and varies with magnetic field strength. This uniqueness in M_z recovery rates is what generates contrast enabling MRI to differentiate between different types of tissue. In MRI experiments, the signal of a single voxel contains spins having different T_1. The longitudinal relaxation is then described by muti-exponential curve.
3. Initially in phase, the excited spins begin to dephase. How fast a spin precesses depends on the magnetic field that it experiences. Interactions between spins generate fluctuating magnetic fields at the sites of the nuclear spins, leading to different precession frequencies. The frequency differences cause a cumulative loss of phase across the excited spins, and results in an overall loss of signal. The signal decay due to spin-spin relaxation is often also described by an exponential curve, whose decay rate is characterized by the relaxation time constant T_2, which is unique to every tissue and is

determined primarily by its chemical environment, with little dependence on field strength. In reality, many fixed factors, such as the imperfect magnet and field distortion resulting from air/tissue interfaces, create inhomogeneities of a magnetic field and cause signal to decay even quicker. The sum total of all of these random and fixed effects is called T_2^* relaxation.

Spin/gradient echo

The signal decay due to fixed effects (e.g., the imperfect magnet and field distortion resulting from air/tissue interfaces) can be compensated for using a spin echo. The pulse sequence diagram for a spin echo (SE) experiment is shown in Figure 1.1:

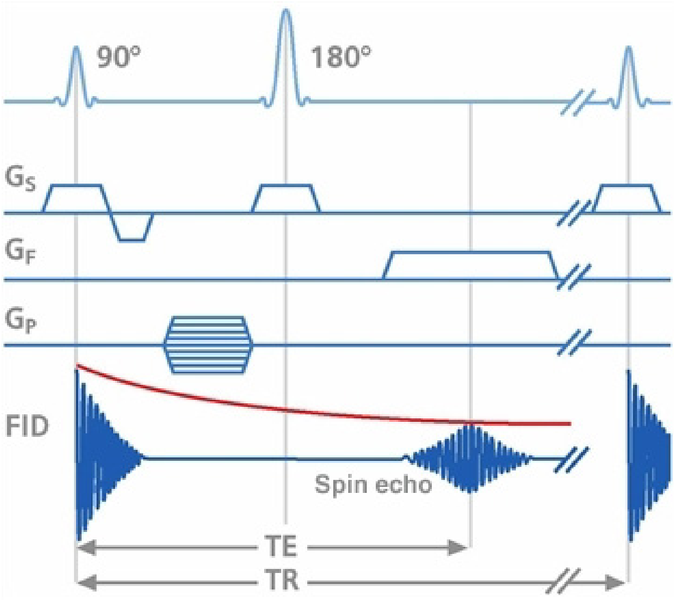

Figure 1.1. Spin echo pulse sequence diagram.

The net magnetization is flipped by a 90 degree RF pulse into the XY plane;

A time of TE/2 (TE refers to time to echo) is allowed to elapse while the spins dephase due to T_2^* effects;

At t = TE/2, a 180 degree RF pulse is applied to flip the dephased vectors;

Another TE/2 time is allowed to pass while the vectors rephase;

At t = TE, the vectors have rephased and a spin echo forms.

The signal intensity equation in a standard spin-echo sequence is expressed as follows:

$$S_{T1W} = S_0 \cdot \exp(-TE/T_2) \cdot [1 - \exp(-TR/T_1)],$$

where S_0 is the proton density and TR is the repetition time. This expression indicates that T_1-weighted, T_2-weighted and proton density weighted (PDW) images can be generated depending on the choice of values for TR and TE. Long TR and short TE yield PDW images; long TR and long TE yield T_2-weighted images; short TR and short TE yield T_1-weighted images.

The formation of gradient echo (GE) does not utilize the 180 degree rephasing RF pulse. As a result, the GE signal suffers from T_2^* decay. However, small flip angles are employed, which, in turn, allow very short repetition time (TR) values, thus decreasing the scan time.

1.2.2.2 MR contrast agent/tracers

MRI techniques exist that utilize both exogenous and endogenous tracers. In this dissertation, the focus is on exogenous MR contrast agents (CA). Interestingly, MR CAs are not directly MR detectable, but their effects are indirectly observed. For example, a T_1-weighted contrast-enhanced image is an image of the bulk water in which a hyperintense region due to water with short, CA-induced T_1 reflects high CA concentration at that region. The signal intensity of these contrast-enhanced MR images includes anatomic information and dynamic data may include more information.

The vast majority of all exogenous MR CAs, used both clinically and preclinically, utilize the gadolinium ion Gd^{3+}. These chelated gadolinium compounds (examples of currently used chelates are shown in Figure 1.2) affect the nuclear magnetic relaxation times of the water protons in surrounding tissues. The relaxivity enhancement of water protons in aqueous solutions of Gd^{3+} complexes arises from time fluctuation of the dipolar coupling between the electron magnetic moment of the metal ion and the nuclear magnetic moment of the solvent nuclei. This interaction is traditionally described with a two-component, inner sphere and outer-sphere [68, 69]. Inner sphere refers to the water molecules present in the coordination sites of the Gd^{3+} ion and outer sphere involves all the solvent molecules diffusing past the complex. The measured relaxation rate (R^{obs}) can be written as the sum of the relaxation rate of the solvent (R^{w}) in the absence of the paramagnetic complex, inner-sphere relaxation rate (R^{inner}) and outer-sphere relaxation rate (R^{outer}):

$$R^{obs} = R^{w} + R^{inner} + R^{outer}$$

Further, the sum of R^{inner} and R^{outer} is proportional to the concentration of Gd^{3+} ions.

$$R^{obs} = R^{w} + \text{constant}*[Gd^{3+}] \qquad ,$$

where the constant is relaxivity, a measure of the effectiveness of the CA.

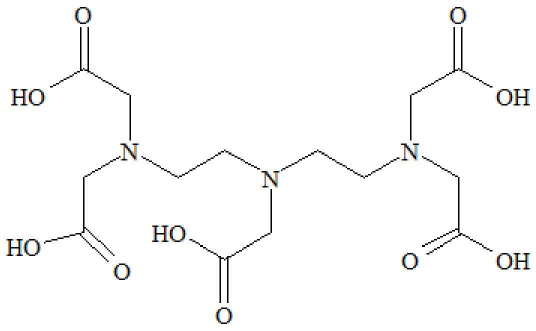

DTPA

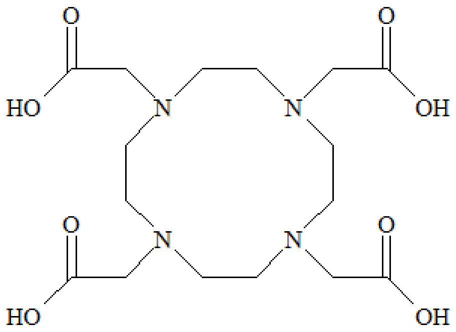

DOTA

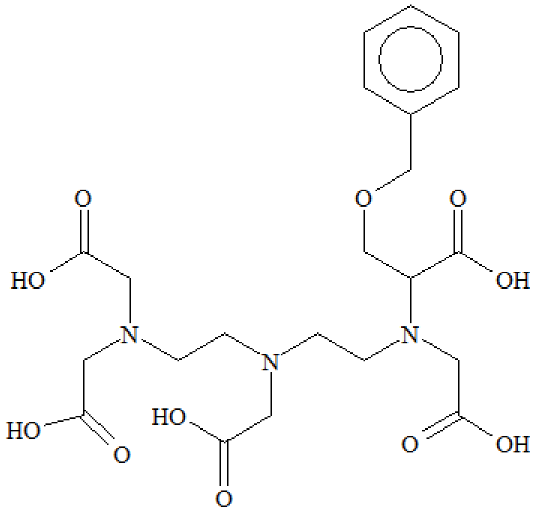

BOPTA

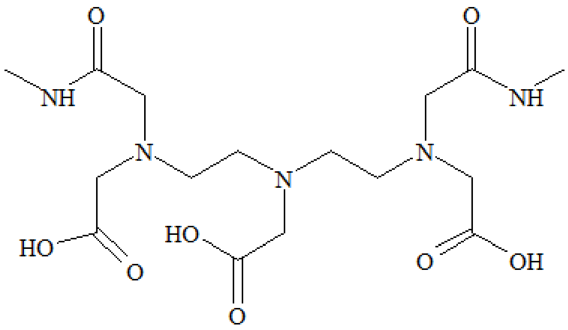

BMA

Figure 1.2. Example chelates for Gd-based contrast agents.

1.2.2.3 T_1-weighted post-gadolinium and T_2-weighted imaging

As mentioned, the time constant T_1 is unique to every tissue and can be affected by the exogenous MR CA. This enables T_1 as a very important contrast in MR imaging. Water with a short T_1, either caused by high CA concentration at that location or a short native T_1, appears bright on a T_1-weighted post-Gd image. Chelated gadolinium compounds, the most commonly used CA, cannot pass the intact blood-brain barrier (BBB) in normal tissue because they are hydrophilic, but can leak into the surrounding tissue through a compromised BBB. Thus, T1-weighted post-Gd imaging is a commonly used biomarker to identify BBB breakdown, which can result from post-operative inflammation, tumor recurrence, radiation necrosis or other adjuvant treatment effects. A large number of studies demonstrate the sensitivity of T_1-weighted post-Gd to various lesions [70-73]. In contrast, the specificity is poor. For example, radiation necrosis and recurrent tumor are both highlighted as bright regions on T_1-weighted post-Gd images [20]. Fortunately, our animal model is a radiation necrosis-only model. The onset, progression and therapeutic response of radiation necrosis in chapter 2 and 4 were well characterized by T_1-weighted post-Gd imaging. Chapter 3 focuses on the validation of the efficacy of anti-VEGF therapy in the treatment of radiation necrosis. Anti-VEGF therapy can decrease the permeability of abnormal vasculature, and can potentially decrease the intensity of necrotic regions in T_1-weighted post-Gd images because a longer time is needed to accumulate the sufficient CA in the necrotic region. To avoid the confusion between decrease of vasculature permeability and decrease of necrosis, T_1-weighted post-Gd data were not used to demonstrate the mitigative effect of anti-VEGF antibodies.

In the clinical setting, T_2-weighted images generally highlight pathology. T_2-weighted imaging has been widely utilized to locate various tumors due to the increased ‘free’ water content in tumor, which has longer T_2 than that of tissue water [74-78]. Although T_2-weighted imaging cannot differentiate radiation necrosis from recurrent tumor, it can be used to characterize the progression of radiation necrosis in our necrosis-only animal model.

1.2.2.4 Dynamic Contrast Enhanced imaging (DCE)

DCE is a noninvasive quantitative method of investigating microvascular structure and function by tracking the pharmacokinetics of injected paramagnetic contrast agents as they pass through the lesion vasculature [79]. This technique is sensitive to alterations in vascular permeability, extracellular extravascular and vascular volumes, and blood flow.

In DCE measurement, an intravenous bolus of gadolinium contrast agent enters tissue arteries, passes through capillary beds and then drains via veins. In normal brain tissue, the paramagnetic ions do not enter extravascular space and pass through the tissue vasculature rapidly compared with the usual temporal resolution of DCE. As a result, the T1-weighted DCE signal does not change with time. In tumor, gadolinium ions leak into extravascular extracellular space and leads to an increase in T1-weighted signal intensity within each single voxel. The degree of signal enhancement depends on physiological and physical factors, including tissue perfusion, the arterial input function (AIF), which is the concentration-time course of contrast agent in the artery supplying the vascular bed, the capillary surface area, capillary permeability and the volume of the extracellular extravascular leakage space (EES). The T1-weighted DCE signal intensity will return to its initial value as the ions drain via veins.

T_1-weighted DCE signal can be converted into contrast agent concentration assuming that the relaxation rate constant, R_1 (=$1/T_1$), is proportional to the contrast agent concentration. The time course of changes in concentration is described as [80]:

$$\frac{dC_t}{dt} = K^{trans}(C_p - V_e C_t)$$

Where V_e is the volume of extravascular extracellular space, K^{trans} is the volume transfer rate between blood plasma and V_e, C_t is the concentration of contrast agent in the tissue and C_p is the concentration of contrast agent in the blood, also known as arterial input function (AIF). High K^{trans} values indicate that the BBB is not intact, while low K^{trans} values indicate that the BBB is intact. It is evident that both K^{trans} amd V_e can be obtained if the C_t and AIF are measured accurately. Ideally, the AIF is a "delta" function, but, in practice, it is more like a bell curve due to the time to inject contrast agent and the fact that the agent is mixed with blood. AIF measurement has a major impact on DCE data analysis. Unfortunately, direct AIF measurement is technically demanding and, at best, obtained from a nearby large artery which may differ from the vessel supplying the tissue of interest. There have also been attempts to use a mathematical function describing AIF [81]. In our DCE experiments conducted in mouse brain, it is hard to define a high quality AIF region. Instead, a reference region approach was employed [82, 83]. The reference region is composed of muscle outside the skull. The reference region (RR) model establishes a relationship between C_t and C_{RR} (CA concentration in the reference region) that allows the derivation of a model that is independent of C_p:

$$C_t = \frac{K^{trans,t}}{K^{trans,RR}} \cdot C_{RR} + \frac{K^{trans,t}}{K^{trans,RR}} \cdot \left(\frac{K^{trans,RR}}{V_{e,RR}} - \frac{K^{trans,t}}{V_{e,t}}\right) \cdot \int_0^T C_{RR} \cdot \exp\left[-\frac{K^{trans,t}}{V_{e,t}} \cdot (T-t)\right] dt$$

Where $K^{trans,RR}$ and $K^{trans,t}$ are K^{trans} for the RR and tissue of interest, respectively; $V_{e,RR}$ and $V_{e,t}$ are V_e for the RR and tissue of interest, respectively. With fixed $K^{trans,RR}$ and $V_{e,RR}$, both $K^{trans,t}$ and $V_{e,t}$ are obtained by performing a two-parameter fit.

In this dissertation, in order to validate the hypothesis that anti-VEGF antibodies repair the abnormal vasculature in necrotic region, K^{trans} maps for non-antibody-treated and antibody-treated mice at 13 weeks following a single 50-Gy dose of radiation were compared. Further, K^{trans} maps pre and post a single antibody treatment for the same animal were compared to study the immediate effect of the anti-VEGF antibody.

1.2.2.5 Quantitative blood oxygen level dependent (qBOLD)

Remarkable changes in cerebral blood flow and oxygen consumption are observed in the region of tumor. Quantitative evaluation of these changes, such as cerebral blood flow (CBF), cerebral blood volume (CBV), oxygen extraction fraction (OEF) and other important hemodynamic parameters, has been shown to provide *in vivo* functional information [84, 85] and increase the accuracy of tumor diagnosis [86-88]. Benefits of the measurements targeting these hemodynamic parameters in differentiating recurrent tumor from radiation necrosis have been reported [89-91]. However, there is no current clinically accepted MRI-based method for measuring OEF, the major parameter characterizing brain hemodynamics, *in vivo*. Currently, the only clinically accepted OEF measurement relies on PET techniques [92]. But the PET-based methods are limited in human study and clinical practice due to their low spatial resolution and the need for radionuclides.

qBOLD imaging technique (details discussed in chapter 5), recently developed by Dr. Dmitriy Yablonskiy, provides an MRI-based method to measure deoxyhemoglobin-containing (veins and ravenous section of capillaries) cerebral blood volume fraction (dCBV) and OEF *in vivo*. qBOLD has been validated in phantoms [93]. *In vivo* human studies [94] have also demonstrated the feasibility of this approach, but also revealed that obtaining reliable results requires high SNR data and accurate correction for macroscopic magnetic field inhomogeneities. Therefore, qBOLD could be potentially useful in differentiating tumor from radiation necrosis. In this dissertation, qBOLD was investigated in order to evaluate the feasibility of this approach in characterizing radiation necrosis in mouse brain.

1.2.3 Animal model of radiation necrosis

Animal model of specific disease provides a significant opportunity for diagnostic and therapeutic studies with imaging findings directly supported by correlative histology and statistical power, which allows positive results to be readily translated to clinical research investigation. Animal models of brain tumors and stroke have been extensively reported in the literature [95]. Also, there have been attempts to induce radiation necrosis in the brains of large animals, such as pig [96] and cat [97], using various high-dose irradiation, including linear accelerator radiosurgical device and electron beam. In contrast, few small-animal models of radiation necrosis in brain tissue had been reported [98]. Previous animal models were developed primarily in rats [99, 100]. Irradiation of small animals, particularly mice, was performed by irradiating a large portion of the animal's body with selective shielding, rather than by directing radiation doses to focal targets. These approaches do not allow specific targeting of focal regions of mouse brain, a *sine qua non* for such studies.

The recent development of a conformal preclinical irradiation system demonstrated that high-dose, focal, fractionated brain irradiation in small animals is feasible. We recently described a murine model of radiation necrosis using micro-radiotherapy (microRT) system [101]. The progression of necrosis was characterized by contrast-enhanced T1- and T2-weighted MRI and histology reflected changes typically seen in radiation necrosis in human. A brain radiation necrosis model in rats has been established using a small animal radiation research platform, in which the necrosis began to appear at about 5 months post a single 40-Gy dose of x-ray radiation [41]. A mixed rodent model of radiation necrosis and tumor has been developed using a 4-mm radiosurgery cone to deliver a single 60-Gy dose of radiation to an implanted GBM cell line in the brains of rats [102]. Histological evaluation of the brains of rats with implanted irradiated GBM cells showed central liquefaction necrosis in high-dose regions, consistent with necrosis and viable tumor growth in low-dose regions.

Although these studies demonstrated the feasibility of generating radiation necrosis in mouse/rat brain employing stereotactic radiosurgery, they were performed on a small number of animals. Further, determinants of the onset and progression of radiation necrosis in that specific animal model (e.g., radiation dose and fractionation), which are crucial for the design of studies aimed at developing methods to identify/detect, monitor, protect against, and mitigate radiation necrosis, have not been well investigated.

Severity of radiation injury is affected by several factors, including total dose absorbed (dose rate and duration of exposure time), number of exposures, interval between exposures, extent and part of body irradiated, and age of subject exposed [103]. The radiation dose-response relationship has been demonstrated graphically through a curve that maps the biologic effects observed in relation to the dose of radiation received. The curve is either linear or non linear and depicts either a threshold dose or a non-threshold dose [104]. Currently, the committee on the Biological Effects of Ionizing Radiation (BEIR) recommends the use of the linear, non-threshold curve of radiation dose-response for describing most types of cancer [105-107], which implies that the biologic response is directly proportional to the dose and any radiation dose will produce a biologic effect. Also, the BEIR committee believes the linear-quadratic, non-threshold curve is a more accurate reflection of biologic effects at low-dose levels from low-linear-energy-transfer (low LET), such as X and gamma rays. The risk of radiation-induced cancer (e.g., leukemia, breast cancer), and heritable damage are considered to follow this curve. The sigmoid, threshold curve of radiation dose-response is commonly employed in radiotherapy to demonstrate high-dose cellular response. As shown in Figure 1.2, there is a minimal dose of radiation below which observable effects will not occur. At high radiation doses, the curve gradually levels off because the irradiated living specimen or tissue dies before the observable effects appear. An ideal protective agent will move the dose-response curve for normal tissue to the right without affecting that for the lesion. The therapeutic ratio is determined by the horizontal separation between the curves.

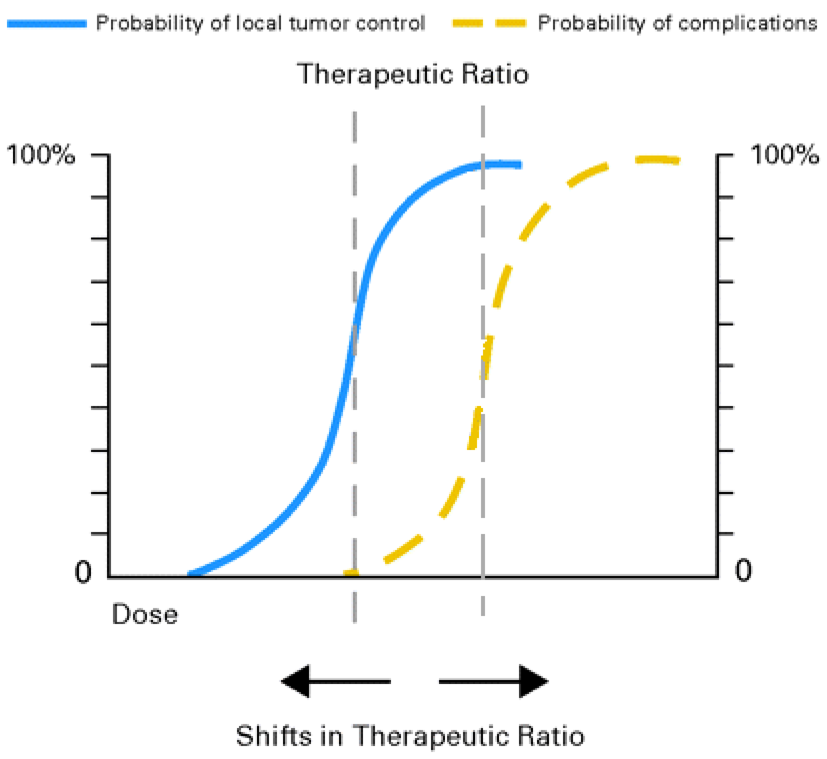

Figure 1.3. Sigmoid dose-response curves showing the relationship between increasing dose and lesion control probability (yellow) and normal tissue complication probability (blue). The therapeutic ratio is determined by the horizontal separation between the curves. An ideal protective agent will move the dose-response curve to the right without affecting the lesion control curve.

Radiation necrosis has been suggested to follow a sigmoid, threshold curve [108]. As a result, the therapeutic effect of any neuroprotective/mitigative agents could be maximized in animals irradiated with radiation doses corresponding to the steep rise in the curve. In this dissertation, a novel animal model of radiation necrosis was developed. Injuries were produced in a large number of mice and critical determinants (dose and fractionation) governing the onset and development of injury were elucidated.

1.2.4 Gamma-Knife irradiation

As mentioned, high-dose, focal, fractionated brain irradiation is the key for developing an animal model of radiation necrosis. The Leksell Gamma Knife® Perfexion™ (Elekta; Stockholm, Sweden; http://www.elekta.com/), is a state-of-the-art unit used for stereotactic irradiation of patients with diseased brain tissue.

A Gamma Knife typically contains 192 cobalt-60 sources of approximately 30 curies each, placed in a circular array in a heavily shielded assembly. Gamma Knife therapy uses doses of radiation to kill cancer cells and shrink tumors, delivered precisely to avoid damaging healthy brain tissue. The device is able to accurately focus multiple beams of gamma radiation on one or more tumors. Each individual beam is of relatively low intensity, so the radiation has little effect on the intervening surrounding healthy brain tissue and is concentrated only at the tumor itself.

Gamma Knife radiosurgery has become an indispensable tool in the primary and adjuvant management of various intracranial pathologies, including meningiomas, pituitary tumors, and arteriovenous malformations [109, 110]. But, as a focused treatment, the role of Gamma Knife radiosurgery in treating a highly invasive tumor, such as a glioblastoma multiforme (GBM), is limited [111].

The device allows reproducible treatment of tumors as small as 1 cm^3 and the geometrical accuracy is approximately 0.5mm. As the volume of a mouse brain is about 3-4 cm^3, gamma knife permits high dose, fractionated, hemispherical irradiation of mouse brain.

The dose of gamma radiation is measured in the unit of gray (Gy), which is defined as the absorption of one joule of gamma energy by one kilogram of matter. The gray is defined independently of the target material. The absorbed dose for biological tissue at a specific location decreases with the distance from the center of radiation focus. The term “xx Gy at the 50% isodose” is frequently used to characterize the distribution of gamma radiation in the tissue, which indicates the half dose of the maximum dose delivered to tissue.

In radiation therapy, the amount of radiation varies depending on the type and stage of cancer being treated. For curative cases, the typical dose for a solid epithelial tumor ranges from 60 to 80 Gy, while lymphomas are treated with 20 to 40 Gy. Preventive (adjuvant) doses are typically around 45–60 Gy, delivered in 1.8–2 Gy fractions (for breast, head, and neck cancers). In this dissertation, more aggressive radiation dose schedules were utilized to ensure a high occurrence of radiation necrosis.

1.3 Aims and Outline

The goals of the investigation are:

i) Develop a novel Gamma-Knife mouse-model of radiation necrosis and optimize the appropriate radiation dosing schemes (total dose, fractionation) for this model;

ii) Determine the efficacy of bevacizumab (Avastin) and B20-4.1.1, both vascular endothelial growth factor (VEGF) inhibitors, as mitigators of radiation necrosis in mice;

iii) Validate the neuroprotective effect of SB 415286, an inhibitor of glycogen synthase kinase 3β (GSK-3β), in mouse brain following high-dose radiation treatment;

iv) Identify and validate qBOLD method as an imaging marker of radiation necrosis.

Chapter 2 focuses on the development and optimization of an animal model of radiation necosis; Chapter 3 and 4 present the mitigation and neuroprotection studies of radiation necrosis in mouse brain, respectively. Chapter 5 discusses the possibility of using qBOLD method to characterize radiation necrosis. Chapter 6 provides a summary and discusses future studies.

References

1. Giglio, P. and M.R. Gilbert, *Cerebral radiation necrosis.* Neurologist, 2003. **9**(4): p. 180-188.
2. Mori, Y., et al., *Effects of stereotactic radiosurgery on an animal model of hippocampal epilepsy.* Neurosurgery, 2000. **46**(1): p. 157-165.
3. Stupp, R., et al., *Effects of radiotherapy with concomitant and adjuvant temozolomide versus radiotherapy alone on survival in glioblastoma in a randomised phase III study: 5-year analysis of the EORTC-NCIC trial.* Lancet Oncology, 2009. **10**(5): p. 459-466.
4. Perry, A. and R.E. Schmidt, *Cancer therapy-associated CNS neuropathology: an update and review of the literature.* Acta Neuropathologica, 2006. **111**(3): p. 197-212.
5. Wong, C.S. and A.J. Van der Kogel, *Mechanisms of radiation injury to the central nervous system: implications for neuroprotection.* Molecular Interventions, 2004. **4**(5): p. 273-284.
6. Remler, M.P., W.H. Marcussen, and J. Tiller-Borsich, *The late effects of radiation on the blood brain barrier.* Int J Radiat Oncol Biol Phys, 1986. **12**(11): p. 1965-9.
7. Garden, G.A. and T. Moller, *Microglia biology in health and disease.* J Neuroimmune Pharmacol, 2006. **1**(2): p. 127-37.
8. Monje, M.L., H. Toda, and T.D. Palmer, *Inflammatory blockade restores adult hippocampal neurogenesis.* Science, 2003. **302**(5651): p. 1760-5.
9. Lee, T.C., et al., *Chronic administration of the angiotensin-converting enzyme inhibitor, ramipril, prevents fractionated whole-brain irradiation-induced perirhinal cortex-dependent cognitive impairment.* Radiat Res. **178**(1): p. 46-56.
10. Robbins, M.E., et al., *The AT1 receptor antagonist, L-158,809, prevents or ameliorates fractionated whole-brain irradiation-induced cognitive impairment.* Int J Radiat Oncol Biol Phys, 2009. **73**(2): p. 499-505.
11. Acharya, M.M., et al., *Human neural stem cell transplantation ameliorates radiation-induced cognitive dysfunction.* Cancer Res. **71**(14): p. 4834-45.
12. Reinhold, H.S., et al., *Development of blood vessel-related radiation damage in the fimbria of the central nervous system.* Int J Radiat Oncol Biol Phys, 1990. **18**(1): p. 37-42.
13. Schultheiss, T.E. and L.C. Stephens, *Invited review: permanent radiation myelopathy.* Br J Radiol, 1992. **65**(777): p. 737-53.
14. Brown, W.R., et al., *Capillary loss precedes the cognitive impairment induced by fractionated whole-brain irradiation: a potential rat model of vascular dementia.* J Neurol Sci, 2007. **257**(1-2): p. 67-71.
15. Morris, G.M., et al., *Boron neutron capture irradiation of the rat spinal cord: histopathological evidence of a vascular-mediated pathogenesis.* Radiat Res, 1996. **146**(3): p. 313-20.
16. Greene-Schloesser, D., et al., *Radiation-induced brain injury: A review.* Front Oncol. **2**: p. 73.
17. Kumar, A.J., et al., *Malignant gliomas: MR imaging spectrum of radiation therapy- and chemotherapy-induced necrosis of the brain after treatment.* Radiology, 2000. **217**(2): p. 377-384.
18. Mullins, M.E., et al., *Radiation necrosis versus glioma recurrence: Conventional MR imaging clues to diagnosis.* American Journal of Neuroradiology, 2005. **26**(8): p. 1967-

1972.

19. Dequesada, I.M., et al., *Can Standard Magnetic Resonance Imaging Reliably Distinguish Recurrent Tumor from Radiation Necrosis after Radiosurgery for Brain Metastases? A Radiographic-Pathological Study.* Neurosurgery, 2008. **63**(5): p. 898-903.
20. Tsuruda, J.S., et al., *Radiation Effects on Cerebral White Matter - Mr Evaluation.* American Journal of Roentgenology, 1987. **149**(1): p. 165-171.
21. Schaefer, P.W., et al., *Assessing tissue viability with MR diffusion and perfusion imaging.* American Journal of Neuroradiology, 2003. **24**(3): p. 436-443.
22. Hein, P.A., et al., *Diffusion-weighted Imaging in the follow-up of treated high-grade gliomas: Tumor recurrence versus radiation injury.* American Journal of Neuroradiology, 2004. **25**(2): p. 201-209.
23. Wang, S.L., et al., *Evaluation of radiation necrosis and malignant glioma in rat models using diffusion tensor MR imaging.* Journal of Neuro-Oncology, 2012. **107**(1): p. 51-60.
24. Asao, C., et al., *Diffusion-weighted imaging of radiation-induced brain injury for differentiation from tumor recurrence.* American Journal of Neuroradiology, 2005. **26**(6): p. 1455-1460.
25. Castillo, M., et al., *Apparent diffusion coefficients in the evaluation of high-grade cerebral gliomas.* American Journal of Neuroradiology, 2001. **22**(1): p. 60-64.
26. Catalaa, I., et al., *Perfusion, diffusion and spectroscopy values in newly diagnosed cerebral gliomas.* Nmr in Biomedicine, 2006. **19**(4): p. 463-475.
27. Padhani, A.R. and J.E. Husband, *Dynamic contrast-enhanced MRI studies in oncology with an emphasis on quantification, validation and human studies.* Clinical Radiology, 2001. **56**(8): p. 607-620.
28. Aronen, H.J. and J. Perkio, *Dynamic susceptibility contrast MRI of gliomas.* Neuroimaging Clinics of North America, 2002. **12**(4): p. 501-+.
29. Covarrubias, D.J., B.R. Rosen, and M.H. Lev, *Dynamic magnetic resonance perfusion imaging of brain tumors.* Oncologist, 2004. **9**(5): p. 528-537.
30. Ellika, S.K., et al., *Role of perfusion CT in glioma grading and comparison with conventional MR imaging features.* American Journal of Neuroradiology, 2007. **28**(10): p. 1981-1987.
31. Sugahara, T., et al., *Posttherapeutic intraaxial brain tumor: the value of perfusion-sensitive contrast-enhanced MR imaging for differentiating tumor recurrence from nonneoplastic contrast-enhancing tissue.* AJNR Am J Neuroradiol, 2000. **21**(5): p. 901-9.
32. Jain, R.K., R.T. Tong, and L.L. Munn, *Effect of vascular normalization by antiangiogenic therapy on interstitial hypertension, peritumor edema, and lymphatic metastasis: insights from a mathematical model.* Cancer Res, 2007. **67**(6): p. 2729-35.
33. Jain, R.K., *Normalizing tumor vasculature with anti-angiogenic therapy: a new paradigm for combination therapy.* Nat Med, 2001. **7**(9): p. 987-9.
34. Ando, K., et al., *[Usefulness of Cho/Cr ratio in proton MR spectroscopy for differentiating residual/recurrent glioma from non-neoplastic lesions].* Nihon Igaku Hoshasen Gakkai Zasshi, 2004. **64**(3): p. 121-6.
35. Dowling, C., et al., *Preoperative proton MR spectroscopic imaging of brain tumors: correlation with histopathologic analysis of resection specimens.* AJNR Am J Neuroradiol, 2001. **22**(4): p. 604-12.
36. Rock, J.P., et al., *Associations among magnetic resonance spectroscopy, apparent diffusion coefficients, and image-guided histopathology with special attention to*

radiation necrosis. Neurosurgery, 2004. **54**(5): p. 1111-1117.

37. Zeng, Q.S., et al., *Multivoxel 3D proton MR spectroscopy in the distinction of recurrent glioma from radiation injury.* Journal of Neuro-Oncology, 2007. **84**(1): p. 63-69.
38. Sundgren, P.C., et al., *Differentiation of recurrent brain tumor versus radiation injury using diffusion tensor imaging in patients with new contrast-enhancing lesions.* Magnetic Resonance Imaging, 2006. **24**(9): p. 1131-1142.
39. Schlemmer, H.P., et al., *Proton MR spectroscopic evaluation of suspicious brain lesions after stereotactic radiotherapy.* American Journal of Neuroradiology, 2001. **22**(7): p. 1316-1324.
40. Chong, V.F.H., et al., *Temporal lobe changes following radiation therapy: imaging and proton MR spectroscopic findings.* European Radiology, 2001. **11**(2): p. 317-324.
41. Zhou, J.Y., et al., *Differentiation between glioma and radiation necrosis using molecular magnetic resonance imaging of endogenous proteins and peptides.* Nature Medicine, 2011. **17**(1): p. 130-U308.
42. Alexiou, G.A., et al., *Glioma recurrence versus radiation necrosis: accuracy of current imaging modalities.* J Neurooncol, 2009. **95**(1): p. 1-11.
43. Brismar, J., G.H. Roberson, and K.R. Davis, *Radiation necrosis of the brain. Neuroradiological considerations with computed tomography.* Neuroradiology, 1976. **12**(2): p. 109-13.
44. Mikhael, M.A., *Radiation Necrosis of the Brain - Correlation between Patterns on Computed-Tomography and Dose of Radiation.* Journal of Computer Assisted Tomography, 1979. **3**(2): p. 241-250.
45. Ogawa, T., et al., *Delayed radiation necrosis of brain evaluated positron emission tomography.* Tohoku J Exp Med, 1988. **155**(3): p. 247-60.
46. Black, K.L., et al., *Use of thallium-201 SPECT to quantitate malignancy grade of gliomas.* J Neurosurg, 1989. **71**(3): p. 342-6.
47. Kline, J.L., R.B. Noto, and M. Glantz, *Single-photon emission CT in the evaluation of recurrent brain tumor in patients treated with gamma knife radiosurgery or conventional radiation therapy.* AJNR Am J Neuroradiol, 1996. **17**(9): p. 1681-6.
48. Yoshii, Y., et al., *Cerebral radiation necrosis with accumulation of thallium 201 on single-photon emission CT.* AJNR Am J Neuroradiol, 1996. **17**(9): p. 1773-6.
49. Moody, E.B., et al., *Thallium-avid cerebral radiation necrosis.* Clin Nucl Med, 1994. **19**(7): p. 611-3.
50. Doyle, W.K., et al., *Differentiation of cerebral radiation necrosis from tumor recurrence by [18F]FDG and 82Rb positron emission tomography.* J Comput Assist Tomogr, 1987. **11**(4): p. 563-70.
51. Di Chiro, G., et al., *Cerebral necrosis after radiotherapy and/or intraarterial chemotherapy for brain tumors: PET and neuropathologic studies.* AJR Am J Roentgenol, 1988. **150**(1): p. 189-97.
52. Glantz, M.J., et al., *Identification of early recurrence of primary central nervous system tumors by [18F]fluorodeoxyglucose positron emission tomography.* Ann Neurol, 1991. **29**(4): p. 347-55.
53. Kim, E.E., et al., *Differentiation of residual or recurrent tumors from post-treatment changes with F-18 FDG PET.* Radiographics, 1992. **12**(2): p. 269-79.
54. Ogawa, T., et al., *Clinical value of PET with 18F-fluorodeoxyglucose and L-methyl-11C-methionine for diagnosis of recurrent brain tumor and radiation injury.* Acta Radiol,

1991. **32**(3): p. 197-202.

55. Shaw, P.J. and D. Bates, *Conservative Treatment of Delayed Cerebral Radiation Necrosis.* Journal of Neurology Neurosurgery and Psychiatry, 1984. **47**(12): p. 1338-1341.
56. Siu, A., et al., *Radiation necrosis following treatment of high grade glioma-a review of the literature and current understanding.* Acta Neurochirurgica, 2012. **154**(2): p. 191-201.
57. But, Q.C., et al., *The efficacy of hyperbaric oxygen therapy in the treatment of radiation-induced late side effects.* International Journal of Radiation Oncology Biology Physics, 2004. **60**(3): p. 871-878.
58. Kohshi, K., et al., *Successful treatment of radiation-induced brain necrosis by hyperbaric oxygen therapy.* Journal of the Neurological Sciences, 2003. **209**(1-2): p. 115-117.
59. Tibbles, P.M. and J.S. Edelsberg, *Medical progress - Hyperbaric-oxygen therapy.* New England Journal of Medicine, 1996. **334**(25): p. 1642-1648.
60. Ferrara, N., K.J. Hillan, and W. Novotny, *Bevacizumab (Avastin), a humanized anti-VEGF monoclonal antibody for cancer therapy.* Biochemical and Biophysical Research Communications, 2005. **333**(2): p. 328-335.
61. Gonzalez, J., et al., *Effect of bevacizumab on radiation necrosis of the brain.* International Journal of Radiation Oncology Biology Physics, 2007. **67**(2): p. 323-326.
62. Jeyaretna, D.S., et al., *Exacerbation of Cerebral Radiation Necrosis by Bevacizumab.* Journal of Clinical Oncology, 2011. **29**(7): p. E159-E162.
63. Torcuator, R., et al., *Initial experience with bevacizumab treatment for biopsy-confirmed cerebral radiation necrosis.* Neuro-Oncology, 2007. **9**(4): p. 580-581.
64. Levin, V.A., et al., *Randomized Double-Blind Placebo-Controlled Trial of Bevacizumab Therapy for Radiation Necrosis of the Central Nervous System.* International Journal of Radiation Oncology Biology Physics, 2011. **79**(5): p. 1487-1495.
65. Rahmathulla, G., et al., *Laser interstitial thermal therapy for focal cerebral radiation necrosis: a case report and literature review.* Stereotact Funct Neurosurg. **90**(3): p. 192-200.
66. Levitt, M.H., *Spin dynamics : basics of nuclear magnetic resonance*. 2nd ed. 2008, Chichester, England ; Hoboken, NJ: John Wiley & Sons. xxv, 714 p., [7] p. of plates.
67. Bernstein, M.A., K.F. King, and Z.J. Zhou, *Handbook of MRI pulse sequences*. 2004, Amsterdam ; Boston: Academic Press. xxii,1017 p.
68. Caravan, P., et al., *Gadolinium(III) chelates as MRI contrast agents: Structure, dynamics, and applications.* Chemical Reviews, 1999. **99**(9): p. 2293-2352.
69. Botta, M., *Second coordination sphere water molecules and relaxivity of gadolinium(III) complexes: Implications for MRI contrast agents.* European Journal of Inorganic Chemistry, 2000(3): p. 399-407.
70. Seltzer, S., A.S. Mark, and S.W. Atlas, *CNS sarcoidosis: evaluation with contrast-enhanced MR imaging.* AJNR Am J Neuroradiol, 1991. **12**(6): p. 1227-33.
71. Yuan, C., et al., *Contrast-enhanced high resolution MRI for atherosclerotic carotid artery tissue characterization.* J Magn Reson Imaging, 2002. **15**(1): p. 62-7.
72. Seki, H., M. Kimura, and K. Sakai, *Myometrial invasion of endometrial carcinoma: assessment with dynamic MR and contrast-enhanced T1-weighted images.* Clin Radiol, 1997. **52**(1): p. 18-23.
73. Rowley, H.A., et al., *Contrast-enhanced MR imaging of brain lesions: a large-scale intraindividual crossover comparison of gadobenate dimeglumine versus gadodiamide.* AJNR Am J Neuroradiol, 2008. **29**(9): p. 1684-91.

74. Herskovits, E.H., R. Itoh, and E.R. Melhem, *Accuracy for detection of simulated lesions: comparison of fluid-attenuated inversion-recovery, proton density--weighted, and T2-weighted synthetic brain MR imaging.* AJR Am J Roentgenol, 2001. **176**(5): p. 1313-8.
75. Arakia, Y., et al., *MR fluid-attenuated inversion recovery imaging as routine brain T2-weighted imaging.* Eur J Radiol, 1999. **32**(2): p. 136-43.
76. Bartzokis, G., et al., *The incidence of T2-weighted MR imaging signal abnormalities in the brain of cocaine-dependent patients is age-related and region-specific.* AJNR Am J Neuroradiol, 1999. **20**(9): p. 1628-35.
77. Okubo, T., et al., *Detection of brain metastasis: comparison of Turbo-FLAIR imaging, T2-weighted imaging and double-dose gadolinium-enhanced MR imaging.* Radiat Med, 1998. **16**(4): p. 273-81.
78. Hockings, P.D., et al., *Correlation between high-field T2-weighted MR imaging and histology of ischemic lesions in gerbil brain.* J Magn Reson Imaging, 1995. **5**(4): p. 437-42.
79. O'Connor, J.P.B., et al., *DCE-MRI biomarkers in the clinical evaluation of antiangiogenic and vascular disrupting agents.* British Journal of Cancer, 2007. **96**(2): p. 189-195.
80. Tofts, P.S., et al., *Estimating kinetic parameters from dynamic contrast-enhanced T(1)-weighted MRI of a diffusable tracer: Standardized quantities and symbols.* Journal of Magnetic Resonance Imaging, 1999. **10**(3): p. 223-232.
81. Patankar, T.F., et al., *Is volume transfer coefficient (K-trans) related to histologic grade in human gliomas?* American Journal of Neuroradiology, 2005. **26**(10): p. 2455-2465.
82. Yankeelov, T.E., et al., *Quantitative pharmacokinetic analysis of DCE-MRI data without an arterial input function: a reference region model.* Magnetic Resonance Imaging, 2005. **23**(4): p. 519-529.
83. Wang, B., Z.Q. Gao, and X. Yan, *Correlative study of angiogenesis and dynamic contrast-enhanced magnetic resonance imaging features of hepatocellular carcinoma.* Acta Radiol, 2005. **46**(4): p. 353-8.
84. Iadecola, C., *Neurovascular regulation in the normal brain and in Alzheimer's disease.* Nature Reviews Neuroscience, 2004. **5**(5): p. 347-360.
85. Raichle, M.E. and D.A. Gusnard, *Appraising the brain's energy budget.* Proceedings of the National Academy of Sciences of the United States of America, 2002. **99**(16): p. 10237-10239.
86. Derdeyn, C.P., et al., *Variability of cerebral blood volume and oxygen extraction: stages of cerebral haemodynamic impairment revisited.* Brain, 2002. **125**: p. 595-607.
87. Davda, S. and T. Bezabeh, *Advances in methods for assessing tumor hypoxia in vivo: Implications for treatment planning.* Cancer and Metastasis Reviews, 2006. **25**(3): p. 469-480.
88. Tatum, J.L., et al., *Hypoxia: Importance in tumor biology, noninvasive measurement by imaging, and value of its measurement in the management of cancer therapy.* International Journal of Radiation Biology, 2006. **82**(10): p. 699-757.
89. Barajas, R.F., et al., *Distinguishing Recurrent Intra-Axial Metastatic Tumor from Radiation Necrosis Following Gamma Knife Radiosurgery Using Dynamic Susceptibility-Weighted Contrast-Enhanced Perfusion MR Imaging.* American Journal of Neuroradiology, 2009. **30**(2): p. 367-372.
90. Dean, B.L., et al., *Cerebral Hemodynamics and Cerebral Blood-Volume - Mr Assessment Using Gadolinium Contrast Agents and T1-Weighted Turbo-Flash Imaging.* American

Journal of Neuroradiology, 1992. **13**(1): p. 39-48.

91. Schwartz, R.B., et al., *Radiation Necrosis Vs High-Grade Recurrent Glioma - Differentiation by Using Dual-Isotope Spect with Tl-201 and Tc-99m-Hmpao.* American Journal of Roentgenology, 1992. **158**(2): p. 399-404.
92. Mintun, M.A., et al., *Brain Oxygen Utilization Measured with O-15 Radiotracers and Positron Emission Tomography.* Journal of Nuclear Medicine, 1984. **25**(2): p. 177-187.
93. Yablonskiy, D.A., *Quantitation of intrinsic magnetic susceptibility-related effects in a tissue matrix. Phantom study.* Magnetic Resonance in Medicine, 1998. **39**(3): p. 417-428.
94. He, X. and D.A. Yablonskiy, *Quantitative BOLD: Mapping of human cerebral deoxygenated blood volume and oxygen extraction fraction: Default state.* Magnetic Resonance in Medicine, 2007. **57**(1): p. 115-126.
95. Fomchenko, E.I. and E.C. Holland, *Mouse models of brain tumors and their applications in preclinical trials.* Clinical Cancer Research, 2006. **12**(18): p. 5288-5297.
96. Miot, E., et al., *Experimental Mr Study of Cerebral Radiation-Injury - Quantitative T2 Changes over Time and Histopathologic Correlation.* American Journal of Neuroradiology, 1995. **16**(1): p. 79-85.
97. Blatt, D.R., et al., *Temporal Characteristics of Radiosurgical Lesions in an Animal-Model.* Journal of Neurosurgery, 1994. **80**(6): p. 1046-1055.
98. Tran, D.K. and R.L. Jensen, *Treatment-related brain tumor imaging changes: So-called "pseudoprogression" vs. tumor progression: Review and future research opportunities.* Surg Neurol Int. **4**(Suppl 3): p. S129-35.
99. Rabinov, J.D., et al., *MR spectroscopic changes in the rat hippocampus following proton radiosurgery.* Stereotactic and Functional Neurosurgery, 2006. **84**(4): p. 147-154.
100. Kondziolka, D., et al., *Radiobiology of Radiosurgery .2. The Rat-C6 Glioma Model.* Neurosurgery, 1992. **31**(2): p. 280-288.
101. Jost, S.C., et al., *A Novel Murine Model for Localized Radiation Necrosis and Its Characterization Using Advanced Magnetic Resonance Imaging.* International Journal of Radiation Oncology Biology Physics, 2009. **75**(2): p. 527-533.
102. Kumar, S., et al., *Development of a novel animal model to differentiate radiation necrosis from tumor recurrence.* Journal of Neuro-Oncology, 2012. **108**(3): p. 411-420.
103. Thames, H.D., Jr., et al., *Changes in early and late radiation responses with altered dose fractionation: implications for dose-survival relationships.* Int J Radiat Oncol Biol Phys, 1982. **8**(2): p. 219-26.
104. Altshuler, B., *Modeling of Dose-Response Relationships.* Environmental Health Perspectives, 1981. **42**(Dec): p. 23-27.
105. Assembly of Life Sciences (U.S.). Committee on the Biological Effects of Ionizing Radiations., *The Effects on populations of exposure to low levels of ionizing radiation, 1980.* 1980, Washington, D.C.: National Academy Press. xv, 524 p.
106. National Research Council (U.S.). Advisory Committee on the Biological Effects of Ionizing Radiations., United States. Environmental Protection Agency. Radiation Office., and National Academy of Sciences Washington D.C., *The effects on populations of exposure to low levels of ionizing radiation; report*. 1972, Washington,: National Academy of Sciences - National Research Council. xiii, 217 p.
107. National Research Council (U.S.). Advisory Committee on the Biological Effects of Ionizing Radiations., *The effects on populations of exposure to low levels of ionizing radiation*. 1976, Washington, D.C.: Division of Medical Sciences, National Academy of

Sciences, National Research Council. xiii, 216 p.
108. Schollnberger, H., et al., *Explanation of protective effects of low doses of gamma-radiation with a mechanistic radiobiological model.* International Journal of Radiation Biology, 2002. **78**(12): p. 1159-1173.
109. Donnet, A., D. Valade, and J. Regis, *Gamma knife treatment for refractory cluster headache: prospective open trial.* J Neurol Neurosurg Psychiatry, 2005. **76**(2): p. 218-21.
110. Herman, J.M., et al., *Repeat gamma knife radiosurgery for refractory or recurrent trigeminal neuralgia: treatment outcomes and quality-of-life assessment.* Int J Radiat Oncol Biol Phys, 2004. **59**(1): p. 112-6.
111. Crowley, R.W., N. Pouratian, and J.P. Sheehan, *Gamma knife surgery for glioblastoma multiforme.* Neurosurg Focus, 2006. **20**(4): p. E17.
112. Stupp, R., W.P. Mason, and M.J. van den Beuf, *Radiotherapy plus concomitant and adjuvant temozolomide for newly diagnosed glioblastoma (vol 352, pg 19, 2005).* Annals of Oncology, 2005. **16**(6): p. 949-949.
113. Tsuyuguchi, N., et al., *Methionine positron emission tomography for differentiation of recurrent brain tumor and radiation necrosis after stereotactic radiosurgery - In malignant glioma.* Annals of Nuclear Medicine, 2004. **18**(4): p. 291-296.
114. Rachinger, W., et al., *Positron emission tomography with O-(2-[F-18]fluoroethyl)-L-tyrosine versus magnetic resonance imaging in the diagnosis of recurrent gliomas.* Neurosurgery, 2005. **57**(3): p. 505-511.
115. Kumar, A.J., et al., *Malignant gliomas: MR imaging spectrum of radiation therapy- and chemotherapy-induced necrosis of the brain after treatment.* Radiology, 2000. **217**(2): p. 377-84.
116. Rahmathulla, G., N.F. Marko, and R.J. Weil, *Cerebral radiation necrosis: A review of the pathobiology, diagnosis and management considerations.* Journal of Clinical Neuroscience, 2013. **20**(4): p. 485-502.
117. Mergenthaler, P., U. Dirnagl, and A. Meisel, *Pathophysiology of stroke: lessons from animal models.* Metab Brain Dis, 2004. **19**(3-4): p. 151-67.
118. van der Worp, H.B., et al., *Hypothermia in animal models of acute ischaemic stroke: a systematic review and meta-analysis.* Brain, 2007. **130**(Pt 12): p. 3063-74.
119. Clarke, M.F., et al., *Cancer stem cells--perspectives on current status and future directions: AACR Workshop on cancer stem cells.* Cancer Res, 2006. **66**(19): p. 9339-44.
120. Jiang, X., et al., *Anti-VEGF antibodies mitigate the development of radiation necrosis in mouse brain.* Clinical Cancer Research, 2013: p. in revision.
121. Conover, W.J., *Practical nonparametric statistics*. 3rd ed. Wiley series in probability and statistics. Applied probability and statistics section. 1999, New York: Wiley. viii, 584 p.
122. Schollnberger, H., et al., *Explanation of protective effects of low doses of gamma-radiation with a mechanistic radiobiological model.* Int J Radiat Biol, 2002. **78**(12): p. 1159-73.
123. Rahmathulla, G., N.F. Marko, and R.J. Weil, *Cerebral radiation necrosis: A review of the pathobiology, diagnosis and management considerations.* Journal of clinical neuroscience : official journal of the Neurosurgical Society of Australasia, 2013. **20**(4): p. 485-502.
124. Remler, M.P., W.H. Marcussen, and J. Tiller-Borsich, *The late effects of radiation on the blood brain barrier.* International journal of radiation oncology, biology, physics, 1986. **12**(11): p. 1965-9.

125. Norden, A.D., J. Drappatz, and P.Y. Wen, *Antiangiogenic therapies for high-grade glioma.* Nature reviews. Neurology, 2009. **5**(11): p. 610-20.
126. Jain, R.K., *Normalization of tumor vasculature: An emerging concept in antiangiogenic therapy.* Science, 2005. **307**(5706): p. 58-62.
127. Dings, R.P.M., et al., *Scheduling of radiation with angiogenesis inhibitors anginex and avastin improves therapeutic outcome via vessel normalization.* Clinical Cancer Research, 2007. **13**(11): p. 3395-3402.
128. Ananthnarayan, S., et al., *Time course of imaging changes of GBM during extended bevacizumab treatment.* Journal of Neuro-Oncology, 2008. **88**(3): p. 339-347.
129. Laird, N.M. and J.H. Ware, *Random-effects models for longitudinal data.* Biometrics, 1982. **38**(4): p. 963-74.
130. Shawler, D.L., et al., *Human Immune-Response to Multiple Injections of Murine Monoclonal Igg.* Journal of Immunology, 1985. **135**(2): p. 1530-1535.
131. Herlyn, D., et al., *Specific Detection of Anti-Idiotypic Immune-Responses in Cancer-Patients Treated with Murine Monoclonal-Antibody.* Journal of Immunological Methods, 1985. **85**(1): p. 27-38.
132. Fagerberg, J., et al., *Humoral anti-idiotypic and anti-anti-idiotypic immune response in cancer patients treated with monoclonal antibody 17-1A.* Cancer Immunology Immunotherapy, 1996. **42**(2): p. 81-87.
133. Yu, L.L., et al., *Interaction between bevacizumab and murine VEGF-A: A reassessment.* Investigative Ophthalmology & Visual Science, 2008. **49**(2): p. 522-527.
134. Xu, Q.W., T. Qaum, and A.P. Adamis, *Sensitive blood-retinal barrier breakdown quantitation using Evans blue.* Investigative Ophthalmology & Visual Science, 2001. **42**(3): p. 789-794.
135. de Groot, J.F., et al., *Tumor invasion after treatment of glioblastoma with bevacizumab: radiographic and pathologic correlation in humans and mice.* Neuro-Oncology, 2010. **12**(3): p. 233-242.
136. Ferrara, N., et al., *Discovery and development of bevacizumab, an anti-VEGF antibody for treating cancer.* Nature Reviews Drug Discovery, 2004. **3**(5): p. 391-400.
137. Brandsma, D., et al., *Clinical features, mechanisms, and management of pseudoprogression in malignant gliomas.* Lancet Oncol, 2008. **9**(5): p. 453-61.
138. Ruben, J.D., et al., *Cerebral radiation necrosis: incidence, outcomes, and risk factors with emphasis on radiation parameters and chemotherapy.* Int J Radiat Oncol Biol Phys, 2006. **65**(2): p. 499-508.
139. Shi, L., et al., *Maintenance of white matter integrity in a rat model of radiation-induced cognitive impairment.* Journal of the Neurological Sciences, 2009. **285**(1-2): p. 178-184.
140. Zhou, H., et al., *Fractionated Radiation-Induced Acute Encephalopathy in a Young Rat Model: Cognitive Dysfunction and Histologic Findings.* American Journal of Neuroradiology, 2011. **32**(10): p. 1795-1800.
141. Wilson, C.M., et al., *Radiation-Induced Astrogliosis and Blood-Brain Barrier Damage Can Be Abrogated Using Anti-Tnf Treatment.* International Journal of Radiation Oncology Biology Physics, 2009. **74**(3): p. 934-941.
142. Embi, N., D.B. Rylatt, and P. Cohen, *Glycogen synthase kinase-3 from rabbit skeletal muscle. Separation from cyclic-AMP-dependent protein kinase and phosphorylase kinase.* Eur J Biochem, 1980. **107**(2): p. 519-27.
143. Leroy, K. and J.P. Brion, *Developmental expression and localization of glycogen synthase*

kinase-3beta in rat brain. J Chem Neuroanat, 1999. **16**(4): p. 279-93.

144. Watcharasit, P., et al., *Direct, activating interaction between glycogen synthase kinase-3beta and p53 after DNA damage.* Proc Natl Acad Sci U S A, 2002. **99**(12): p. 7951-5.
145. Loberg, R.D., E. Vesely, and F.C. Brosius, 3rd, *Enhanced glycogen synthase kinase-3beta activity mediates hypoxia-induced apoptosis of vascular smooth muscle cells and is prevented by glucose transport and metabolism.* J Biol Chem, 2002. **277**(44): p. 41667-73.
146. Song, L., P. De Sarno, and R.S. Jope, *Central role of glycogen synthase kinase-3beta in endoplasmic reticulum stress-induced caspase-3 activation.* J Biol Chem, 2002. **277**(47): p. 44701-8.
147. Thotala, D.K., D.E. Hallahan, and E.M. Yazlovitskaya, *Inhibition of glycogen synthase kinase 3 beta attenuates neurocognitive dysfunction resulting from cranial irradiation.* Cancer Res, 2008. **68**(14): p. 5859-68.
148. Cross, D.A.E., et al., *Selective small-molecule inhibitors of glycogen synthase kinase-3 activity protect primary neurones from death*. 2001. p. 94-102.
149. Yazlovitskaya, E.M., et al., *Lithium treatment prevents neurocognitive deficit resulting from cranial irradiation.* Cancer Res, 2006. **66**(23): p. 11179-86.
150. Thotala, D.K., et al., *A New Class of Molecular Targeted Radioprotectors: Gsk-3 Beta Inhibitors.* International Journal of Radiation Oncology Biology Physics, 2010. **76**(2): p. 557-565.
151. Medina, M. and J. Avila, *Glycogen synthase kinase-3 (GSK-3 beta) inhibitors for the treatment of Alzheimer's disease.* Curr Pharm Des, 2010. **16**(25): p. 2790-8.
152. Klamer, G., et al., *Using Small Molecule GSK3 beta Inhibitors to Treat Inflammation.* Current Medicinal Chemistry, 2010. **17**(26): p. 2873-2881.
153. Phukan, S., et al., *GSK3 beta: role in therapeutic landscape and development of modulators.* British Journal of Pharmacology, 2010. **160**(1): p. 1-19.
154. Coghlan, M.P., et al., *Selective small molecule inhibitors of glycogen synthase kinase-3 modulate glycogen metabolism and gene transcription.* Chem Biol, 2000. **7**(10): p. 793-803.
155. Jost, S.C., et al., *In vivo imaging in a murine model of glioblastoma.* Neurosurgery, 2007. **60**(2): p. 360-70; discussion 370-1.
156. Franken, N.A., et al., *Clonogenic assay of cells in vitro.* Nat Protoc, 2006. **1**(5): p. 2315-9.
157. Ogawa, S., et al., *Brain magnetic resonance imaging with contrast dependent on blood oxygenation.* Proc Natl Acad Sci U S A, 1990. **87**(24): p. 9868-72.
158. Derdeyn, C.P., et al., *Variability of cerebral blood volume and oxygen extraction: stages of cerebral haemodynamic impairment revisited.* Brain, 2002. **125**(Pt 3): p. 595-607.
159. Iadecola, C., *Neurovascular regulation in the normal brain and in Alzheimer's disease.* Nat Rev Neurosci, 2004. **5**(5): p. 347-60.
160. Iadecola, C., *Rescuing troubled vessels in Alzheimer disease.* Nat Med, 2005. **11**(9): p. 923-4.
161. Yamauchi, H., et al., *[Cerebral hemodynamics and risk for recurrent stroke in symptomatic internal carotid artery occlusion]*. Rinsho Shinkeigaku, 1999. **39**(5): p. 513-9.
162. Derdeyn, C.P., R.L. Grubb, Jr., and W.J. Powers, *Cerebral hemodynamic impairment: methods of measurement and association with stroke risk.* Neurology, 1999. **53**(2): p. 251-9.

163. Yablonskiy, D.A. and E.M. Haacke, *Theory of NMR signal behavior in magnetically inhomogeneous tissues: the static dephasing regime.* Magn Reson Med, 1994. **32**(6): p. 749-63.
164. Valk, P.E. and W.P. Dillon, *Radiation-Injury of the Brain.* American Journal of Roentgenology, 1991. **156**(4): p. 689-706.
165. He, X. and D.A. Yablonskiy, *Quantitative BOLD: mapping of human cerebral deoxygenated blood volume and oxygen extraction fraction: default state.* Magn Reson Med, 2007. **57**(1): p. 115-26.
166. Yablonskiy, D.A., *Quantitation of intrinsic magnetic susceptibility-related effects in a tissue matrix. Phantom study.* Magn Reson Med, 1998. **39**(3): p. 417-28.
167. Kelly, S.E., *Gibbs phenomenon for wavelets.* Applied and Computational Harmonic Analysis, 1996. **3**(1): p. 72-81.
168. Fernandez-Seara, M.A. and F.W. Wehrli, *Postprocessing technique to correct for background gradients in image-based R*(2) measurements.* Magn Reson Med, 2000. **44**(3): p. 358-66.
169. Bashir, A. and D.A. Yablonskiy, *Natural linewidth chemical shift imaging (NL-CSI).* Magn Reson Med, 2006. **56**(1): p. 7-18.
170. Yablonskiy, D.A., et al., *Voxel spread function method for correction of magnetic field inhomogeneity effects in quantitative gradient-echo-based MRI.* Magn Reson Med.
171. Ralchle, M.E. and A.Z. Snyder, *A default mode of brain function: A brief history of an evolving idea.* Neuroimage, 2007. **37**(4): p. 1083-1090.
172. Yamauchi, H., et al., *Significance of increased oxygen extraction fraction in five-year prognosis of major cerebral arterial occlusive diseases.* Journal of Nuclear Medicine, 1999. **40**(12): p. 1992-1998.
173. Diringer, M.N., et al., *No reduction in cerebral metabolism as a result of early moderate hyperventilation following severe traumatic brain injury.* Journal of Neurosurgery, 2000. **92**(1): p. 7-13.
174. Adamczak, J.M., et al., *High field BOLD response to forepaw stimulation in the mouse.* Neuroimage. **51**(2): p. 704-12.
175. Saria, A. and J.M. Lundberg, *Evans Blue Fluorescence - Quantitative and Morphological Evaluation of Vascular-Permeability in Animal-Tissues.* Journal of Neuroscience Methods, 1983. **8**(1): p. 41-49.

Chapter 2 Development and Optimization of a Mouse Model of Radiation Necrosis

Declaration

Declaration by Xiaoyu Jiang

In the case of Chapter 2, the nature and extent of my contribution to the work was following:

Publication title	A mouse model of delayed radiation necrosis: Optimization of Gamma Knife radiation dosing; MRI and histologic characterization of onset and progression
Publication status	In preparation
Nature and extent of candidate's contribution	Designed the experiments and performed the anatomic MR imaging and histogram analysis for quantitative comparison of the different progressions of radiation necrosis in control and antibodies-treated mice, and wrote the manuscript
Nature and extent of other co-authors' contribution	JA Engelbach[2] and J Cates[4] irradiated the mice; L Yuan[3] performed the H&E stains; F Gao[5,8] performed the statistical analysis; RE Drzymala[3,4], DE Hallahan[4,8], KM Rich[3,4], and RE Schmidt[6] advised the project and edited the manuscript; JJH Ackerman[1,2,7,8] and JR Garbow[2,8] initiated and supervised the project and edited the manuscript; Departments of [1]Chemistry, [2]Radiology, [3]Neurosurgery, [4]Radiation Oncology, [6]Neuropathology, and [7]Internal Medicine; [5]Division of Biostatistics; and the [8]Alvin J Siteman Cancer Center, Washington

	University, 1 Brookings Drive, St. Louis, MO, 63130; USA

Introduction

The management of both benign and malignant central nervous system tumors remains a challenging clinical problem, often requiring multimodal therapy, including surgical resection, chemotherapy, and radiation. Over the past decade, patient outcomes have benefitted from numerous advances, including novel chemotherapeutic agents, improved surgical resection, and the use of sophisticated, fractionated, high-dose radiation and radiosurgical methods. Radiation effects on non-neoplastic tissue, resulting in acute, early-delayed and late-delayed radiation-induced neurotoxicity, may complicate the outcomes of radiotherapy. Radiation necrosis (RN), a delayed radiation neurotoxicity, can develop in up to 24% of patients receiving focal irradiation three or more months following therapy [1]. The incidence of RN may be threefold higher with concurrent chemotherapy [3, 112].

Since the treatment paradigms for recurrent tumor and necrosis are significantly different, the differentiation between these two lesions may be critically important for achieving better clinical outcomes. Unfortunately, both recurrent tumor and RN have a similar appearance on conventional anatomic magnetic resonance imaging (MRI) and computerized tomography (CT) scans. A number of advanced imaging techniques, including magnetic resonance spectroscopy (MRS), MR diffusion-weighted imaging (DWI), diffusion tensor imaging (DTI) and perfusion techniques, positron emission tomography (PET), and thallium single photon emission computed tomography (SPECT), have been used to evaluate RN [22, 113-115]. Nonetheless, no single imaging modality has been shown to reliably distinguish radiation necrosis from recurrent tumor [116].

Clinicians have relatively few good options for therapeutic invention when patients develop symptomatic radiation necrosis. Surgical resection of necrotic tissue is often not possible due to the location of the necrosis in eloquent regions of the brain. Prolonged treatment with corticosteroids is often employed [55], but is complicated by Cushingnoid side effects, including weight gain, myopathy, immunosuppression, psychiatric disturbances, and occasionally arthritic sequelae, such as avascular necrosis affecting the shoulders and hips [56]. Hyperbaric oxygen treatment has also been explored as a therapeutic modality [57, 59], but it is cumbersome to deliver, expensive, and available in only a few medical centers. Its benefit has only been shown in a small number of cases [58].

A reproducible animal model of radiation necrosis provides a significant opportunity for diagnostic and therapeutic studies with imaging findings directly supported by correlative histology and statistical power, which allows positive results to be readily translated to clinical research investigation. Animal models of brain tumors and stroke have been extensively reported in the literature [117-119]. However, the lack of a well-developed, small-animal model of radiation necrosis has significantly hampered the development of diagnostic and therapeutic management of RN. Until recently, few small-animal models of radiation necrosis in brain tissue had been reported [2, 5], with most previous animal models developed in rats. In the past, irradiation of small animals, particularly mice, was performed by irradiating a large portion of the animal's body with selective shielding, rather than by directing radiation doses to focal targets. These approaches do not allow specific targeting of focal regions of mouse brain, a *sine qua non* for such studies.

The recent development of a conformal preclinical irradiation system demonstrated that high-dose, focal, fractionated brain irradiation in mice is feasible. We recently described a murine model of radiation necrosis using a micro-radiotherapy (microRT) system [101]. The progression of necrosis was characterized by contrast-enhanced T1- and T2-weighted MRI and histology reflected changes typically seen in radiation necrosis in human. A brain radiation necrosis model in rats has been established using a small animal radiation research platform, in which the necrosis began to appear at about 5 months post a single 40-Gy dose of x-ray radiation [41]. A mixed rodent model of radiation necrosis and tumor has been developed using a 4-mm radiosurgery cone to deliver a single 60-Gy dose of radiation to an implanted GBM cell line in the brains of rats [102]. Histological evaluation of the brains of rats with implanted irradiated GBM cells showed central liquefaction necrosis in high-dose regions, consistent with necrosis and viable tumor growth in low-dose regions. Although these studies demonstrated the feasibility of generating radiation necrosis in mouse/rat brain using focal brain irradiation, they were all performed on small cohorts of animals. Determinants of the onset and progression of radiation necrosis, including radiation dose and fractionation, which are crucial for the design of studies aimed at developing methods to identify/detect, monitor, protect against, and mitigate radiation necrosis, have not been well investigated.

The Leksell Gamma Knife (GK) Perfexion, a state-of-the-art unit used for stereotactic irradiation of patients with benign and malignant brain tumors, enables reproducible treatments of a small volume (1 cm^3 or less) with a precision of less than ±0.5 mm in stereotactic space. We hypothesized that this technology could be used to create a murine model of RN, using hemispheric irradiation in a dose and fractionation scheme patterned after therapeutic doses of radiation used clinically. An essential component of critically evaluating animal models of disease and pathology is correlation of findings with goal-standard histology. Herein, we report on the development of a semi-quantitative histologic *scoring system* for evaluation of the extent and severity of tissue injury in our mouse model of RN. In total, the goals of this work were to develop a GK-based murine model of radiation necrosis, to characterize the development of RN using MRI protocols and histologic evaluation, and to elucidate the critical determinants (i.e., radiation dose and fractionation scheme) governing the onset and progression of tissue injury. A well-characterized animal model of RN will provide a platform for studies to optimize dose and fractionation schemes for future clinical treatment protocols.

Materials and Methods

Animals

All studies were performed in accordance with the guidelines of the IACUC and in accordance with protocols approved by the Washington University Division of Comparative Medicine that met or exceeded American Association for the Accreditation of Laboratory Animal Care standards. Female Balb/c mice were used for the study and observed daily and weighed weekly to ensure that interventions were well tolerated.

Small-animal Irradiation

Mice were irradiated with the Leksell Gamma Knife® (GK) Perfexion™ (Elekta; Stockholm, Sweden; http://www.elekta.com/). Mice were supported on a specially designed platform mounted to the stereotactic frame that attaches to the treatment couch of the GK. Mice were anesthetized with a mixture of ketamine (25 mg/kg), acepromazine (5 mg/kg) and xylazine (5 mg/kg), injected intraperitoneally 5 min before the start of irradiation. Four cohorts of female Balb/c mice (n=15 each) were irradiated with four different dose schedules: 60-Gy in a single fraction, 60-Gy in three fractions, 50-Gy in a single fraction and 45-Gy in a single fraction, as described below. The resulting brain parenchymal changes were characterized by both MRI and histology.

MR Imaging

Images were collected in an Agilent/Varian (Santa Clara, CA) 4.7-T small-animal MR scanner equipped with a DirectDrive^{TM} console. The scanner is built around an Oxford Instruments (Oxford, United Kingdom) 33-cm, clear-bore magnet equipped with 21-cm inner diameter, actively shielded Agilent/Magnex gradient coils (maximum gradient, 28 G/cm; rise time approximately 200 ms) and International Electric Company (IEC; Helsinki, Finland) model A-240 amplifiers (300 V and 300 A).

MRI data were collected using an actively decoupled coil pair: 1.5-cm outer diameter surface coil (receive) and a 9-cm inner diameter Helmholtz coil (transmit). Before the imaging experiments, mice were anesthetized with isoflurane/O_2 (3% [vol/vol]) and maintained on isoflurane/O_2 (1% [vol/vol]) throughout the experiments. Mice were restrained in a laboratory-constructed Teflon head holder with ear bars and a tooth bar. To maintain their body temperature at approximately 37°, mice were placed on a water pad circulating warm water. Mice were injected intraperitoneally with 0.5 mL Omniscan (gadodiamide; GE Healthcare, Princeton, NJ) contrast agent, diluted 1:10 in sterile saline, immediately prior to positioning in the magnet.

Mice that received 60-Gy of radiation, in either single or three fractions, or 50-Gy of radiation were imaged 4, 8, and 13 weeks post-irradiation. Mice that received 45-Gy of radiation were imaged 10, 13, 16, 19 and 22 weeks post-irradiation. The time interval between adjacent imaging sessions was chosen to ensure observable progression of RN on anatomic MR images. Mice were sacrificed immediately after the last imaging point (13 and 22 weeks post-irradiation for mice receiving 50/60-Gy and 45-Gy of radiation, respectively). End points were selected because by these times, the majority of mice showed a significant deterioration in physical condition, including loss of more than 20% bodyweight and/or obvious behavioral impairment (such as ataxia), as well as significant RN (>30% of the volume of the irradiated hemisphere), as determined by MR imaging. Multislice, T2-weighted, spin-echo transaxial images were collected beginning ~3 minutes following intraperitoneal injection of 0.5 mL of MultiHance (gadobenate dimeglumine; Bracco Diagnostics) contrast agent, diluted 1:10 in sterile saline, with the following parameters: repetition time [TR] = 1.5 s, echo time [TE] = 0.05 s, field of view [FOV] = 1.5 x 1.5 cm^2, slice thickness = 0.5 mm, 21 slices to cover the whole brain; total acquisition time = 12 minutes. Multislice, T1-weighted, spin-echo transaxial images were then collected over 5 minutes with the following parameters: TR = 0.65 s, TE = 0.02 s, FOV = 1.5 x 1.5 cm^2, slice thickness = 0.5 mm, 21 slices to cover the whole brain.

Measuring Necrotic Volumes Quantitatively by MR Imaging

Regions of radiation necrosis appeared as hyperintense areas on both contrast-enhanced, T1-weighted and T2-weighted images. While either set of images could be used for quantitative analysis, we chose to calculate necrotic volumes from T2-weighted images, as described previously [120]. Briefly, for each set of T2-weighted spin-echo images, regions of interest were drawn around the entire brain in several contiguous image slices, chosen to include the entire hyperintense region. Each brain was divided along the midline into left (irradiated) and right (non-irradiated) hemispheres. The image intensity for each individual pixel in the left hemisphere was normalized by the average of the 25 pixels (5 x 5 square) including and immediately surrounding its mirror-image pixel in the right hemisphere, and histograms of normalized intensity for the irradiated hemisphere were constructed. The same analysis was performed on a cohort (n=10) of non-irradiated mice. The histogram of average intensity distribution for non-irradiated subjects is symmetric; 99% of the pixels are distributed in the intensity range 0.6 – 1.4 about a normalized mean of 1.0. Therefore, an intensity threshold of 1.4 was chosen as the cutoff for normal brain tissue. For images of irradiated mice, the number of pixels exceeding this threshold serves to measure the necrotic volume.

Histology

Selected groups of the mice were sacrificed for histological studies at various times after irradiation. Following intra-cardiac perfusion with 0.1 M Phosphate-buffered saline and formalin, each mouse head was then dissected and immersed in formalin for 24 hours. Brains were then dissected, processed through graded alcohols, embedded in paraffin, and sectioned in coronal planes. Eight-micron-thick tissue sections were stained with hematoxylin and eosin (H&E). Briefly, the slides were de-paraffinized with 100% xylene, 100% ethanol, 90% ethanol, 80% ethanol, and finally distilled water. Nuclei were stained with the alum hematoxylin and rinsed with running tap water, differentiated with 0.3% acid alcohol, and rinsed again with tap water. Slides were stained with eosin for two minutes, followed by a series of dehydration steps. Other samples were fixed in modified Zenker's solution and stained, according to standard protocols, with either phosphotungstic acid-hematoxylin (PTAH) to demonstrate the presence of fibrin in tissue or with trichrome to reveal collagen deposition within the brain.

Statistical Analysis

The differences in MR-derived necrotic volumes for mice having different histological scores were summarized using means and standard deviations, and compared by one-way ANOVA. Due to the relatively large variability in MR-derived necrotic volumes, a logarithm transformation was performed to better satisfy the assumption of a normal distribution. The correlation between

MR results and histology scores was also assessed using Kendall's tau correlation coefficient [121]. All the tests were two-sided and a p-value of 0.05 or less was taken to indicate statistical significance. Statistical analysis was performed using SAS 9.3 (SAS Institutes, Cary, NC).

Results

MRI detects radiation necrosis as image hyperintensity in contrast-enhanced T1-weighted images

Representative contrast-enhanced T1-weighted spin-echo images of irradiated mice, covering the same anatomic region of the brain and collected at 1, 4, 8, and 13 weeks following a single 50-Gy dose of radiation, are shown in Figure 1. Hyperintense areas in these images, due to leaky vasculature, correspond with regions of radiation necrosis in the brain. MR images begin to show hyperintense regions at ~4 weeks post irradiation, and these regions expand significantly in extent by 13 weeks, indicating late onset and rapid progression of radiation necrosis.

Radiation dose schedules affect the onset and progression of radiation necrosis

Figure 2 shows the progressions of the volumes of MRI-derived necrotic regions for irradiated mice, in which mice received four different radiation dose schedules, including 60-Gy in a single fraction (red), 60-Gy in three fractions (green), 50-Gy in a single fraction (black), 45-Gy in a single fraction (blue). Mice received either 60-Gy or 50-Gy of radiation developed RN at 3-4 weeks post irradiation and had significant, large RN (>30% of the volume of the irradiated hemisphere), as determined by anatomic MRI at approximately 13 weeks post irradiation. While time-to-onset of necrosis following 45-Gy irradiation in one fraction occurs much later than with 60/50-Gy irradiation, the rates of injury progression following onset are similar.

Neuropathological Grading System in the Murine Model of Radiation Necrosis.

Histologic changes are shown in control and irradiated mice (Figs 3,4). Changes include microhemorrhages, edema, vascular changes ranging from increased numbers of delicate telangiectatic vessels to fibrinoid necrosis and hyalinization, development of foamy macrophages, infiltration of polymorphonuclear leukocytes, astrocytosis, and loss of tissue elements ranging from neuronal loss to frank involvement of all tissue elements with microcavitation. The severity of histologic changes was independently scored by three individuals, including a clinical neuropathologist (RES), in blinded fashion using a semi-quantitative, 0 to 3 grading system. Figure 3 shows the typical changes characteristic of radiation necrosis in the weeks following irradiation of the murine brains at both low and high magnifications. *Grade 0* was assigned to no histologic changes (Figure 3 A-B). *Grade 1* included mild histological changes associated with radiation injury, including early events such as micro-hemorrhages accompanied by increased numbers of telangiectatic vessels (Figure 3 C-D). *Grade 2* injuries (Figure 3E-F), were characterized by moderate histologic changes, including changes seen in Grade 1 with addition of vascular hyalinization, astrocytosis and tissue loss. *Grade 3* injuries (Figure 3 G-H) resembled those of Grade 2 but were more severe, often including tissue loss with extension to areas of grey matter. Grade 3 injuries also more frequently featured fibrinoid vascular necrosis. This grading system was tested independently by 4 researchers (non-pathologists), with substantial agreement with the neuropathologist.

The most severely involved animals showed hyalinized vessels and fibrinoid vascular necrosis (Figure 5B), and extensive fibrin deposition, highlighted by PTAH staining (blue regions; Figure 4G) and trichrome staining (red regions; Figure 4H). Collagen surrounding the vessel walls was also visualized with trichrome staining (blue material, Figure 4H). These vascular changes were accompanied by macrophages clustered in damaged areas of necrosis and a few cells that showed radiation-induced atypia (Figure 4D). Edema formed in the center of the damaged regions of brains, with decreased neuronal/glial cell density and a paucity of blood vessels and parenchymal structures. Degenerating neurons were characterized by loss of cytoplasm and condensed pyknotic nuclei (Figure 4F).

Tissue damage was noted as early as 3 weeks post radiation in animals that received a single fraction of 60-Gy of radiation, and slightly later (4 weeks) in mice that received a single dose of 50-Gy of radiation. By histologic examination, no specific changes were noted at earlier post-irradiation time points. At later time points, areas with more severe hemorrhage (Figure 4B), foamy macrophages (Figure 4C), parenchymal necrosis (Figure 4F), and tissue loss (Figure 4B, C, and G) were observed.

Histological scores for radiation necrosis correlate with MR-derived necrotic volumes

For each graded histology slide, the MR-derived necrotic volume was calculated from the contrast-enhanced T1-weighted image for a single slice, covering the same anatomic features as the histological slide. The average MR-derived necrotic volumes vs. histological scores are plotted in Figure 5A. The two measures are highly correlated (correlation coefficient = 0.948, with $p<0.0001$) and the differences among the four cohorts (n=30, 37, 27, and 53 for Grade 0, 1, 2, and 3, respectively) are all statistically significant ($p<0.0001$). Further, the correlation between histological score and time post irradiation is displayed in Figure 5B. The differences among the three cohorts (n=17, 15, and 20 for 4, 8, and 13 weeks following 50/60-Gy of radiation) are all statistically significant ($p<0.0001$). These strong correlations help to provide validation for the MR results and demonstrates that the histologic grading system is a useful tool for the classification of the severity of radiation necrosis.

Discussion

Herein, we describe the development and optimization of a mouse model of late onset radiation necrosis. With the aid of a customized, stereotactic head-holder, well-defined doses of Gamma Knife radiation can be accurately and reproducibly delivered hemispherically in mouse brain. An optimized mouse model of radiation necrosis incorporates several important characteristics, including: i) consistent induction of late time-to-onset necrosis following irradiation; ii) characteristic MR imaging changes that allow clear identification of necrotic regions; iii) tissue injury whose histology accurately matches that seen in tissue from patients with confirmed radiation necrosis; iv) progression of necrosis occurs over a reasonable period of time, thereby enabling longitudinal imaging studies to characterize the onset and development of necrosis and its response to therapeutic interventions. Herein, the initiation and progression of necrosis in irradiated mice subjected to different radiation doses and fractionation schedules (60/50/45-Gy in a single fraction and 60-Gy in three fractions) were compared.

As shown in Figure 2, the onset and progression of RN for mice receiving either 60-Gy or 50-Gy are similar, while time-to-onset of necrosis following single-fraction, 45-Gy irradiation occurs much later than with higher doses. The radiation dose-response relationship can be represented graphically by a curve that maps the biologic effects observed in relation to the radiation dose received. A variety of different linear and non-linear models, some including a threshold radiation dose for initiating tissue damage, have been proposed [23]. The sigmoid, threshold curve of radiation dose-response is commonly employed in radiotherapy to demonstrate high-dose cellular response. Treating radiation-induce injury has been described as shifting this sigmoid curve [122]. In terms of the development of RN, a decrease of radiation dose from 50-Gy to 45-Gy causes a much more dramatic difference than a decrease from 60-Gy to 50-Gy, suggesting that 50-Gy is in the rapidly changing part of the sigmoid curve. As a result, 50-Gy is an appropriate radiation dose schedule for testing the efficacy of therapeutic inventions of RN. 50-Gy also provides an appropriate observation window (from-4-to-13 weeks post irradiation) for the development of late-onset necrosis, with evident weekly change in the volume of the necrotic region. Although this dose is substantially higher than a clinical-dose schedule, the resulting radiation necrosis is histologically similar to that induced in patients, suggesting that all the positive results of this model of necrosis can be readily translated.

Our robust mouse model recapitulates significant features of radiation necrosis that occur in response to a number of clinical treatment paradigms. These features include the delayed-onset of radiation changes and well-described histologic changes. A histologic grading system was developed to allow us to assess the severity of the radiation-induced changes in a systemic fashion. Such a semi-quantitative grading system may be employed to assess the effects of radiation sensitizers or protective agents. These studies will not only test the efficacy of various treatment paradigms, but will allow the mechanisms involved in the onset and progression of delayed radiation necrosis and its response to therapeutic interventions to be studied.

Conclusion

By employing the Leksell Gamma Knife Perfexion to stereotactically deliver radiation to one hemisphere of the mouse brain, we have developed a novel murine model of late time-to-onset radiation necrosis. The animal model can be used to reproducibly study radiation necrosis that simulates changes noted in radiation necrosis in the brain. A four-level histologic scoring system was developed to grade the severity of radiation necrosis. The onset and progression of RN in this model can be quantitatively characterized by both preclinical MRI and histology. This mouse model of RN can, thus, serve as a robust platform for a variety of studies, including imaging biomarkers for differentiation of RN from recurrent tumor, mitigation and neuroprotection of radiation necrosis.

Figures

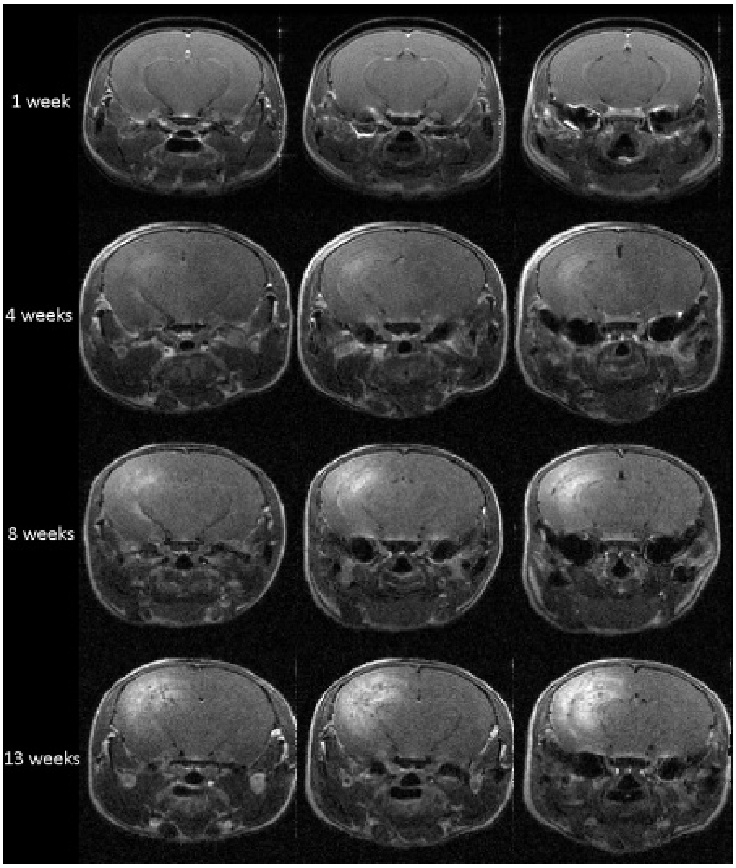

Figure 2.1. MRI can detect radiation necrosis in irradiated mouse brain**.** Representative contrast-enhanced transaxial T1-weighted spin-echo images of irradiated mice at 1, 4, 8, and 13 weeks following a single 50-Gy (50% isodose) of radiation. Slices are chosen to display the same anatomic region of the brain at all four time points.

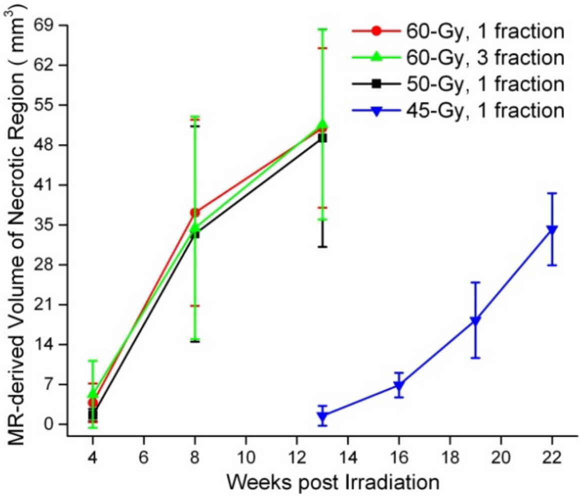

Figure 2.2. MRI-derived necrotic volumes, mean ± SD (n = 15), vs. time post-irradiation for mice irradiated hemispherically with different dose schedules: 60-Gy in 1 fraction (red), 60-Gy in 3 fractions (green), 50-Gy in 1 fraction (black) and 45-Gy in 1 fraction (blue).

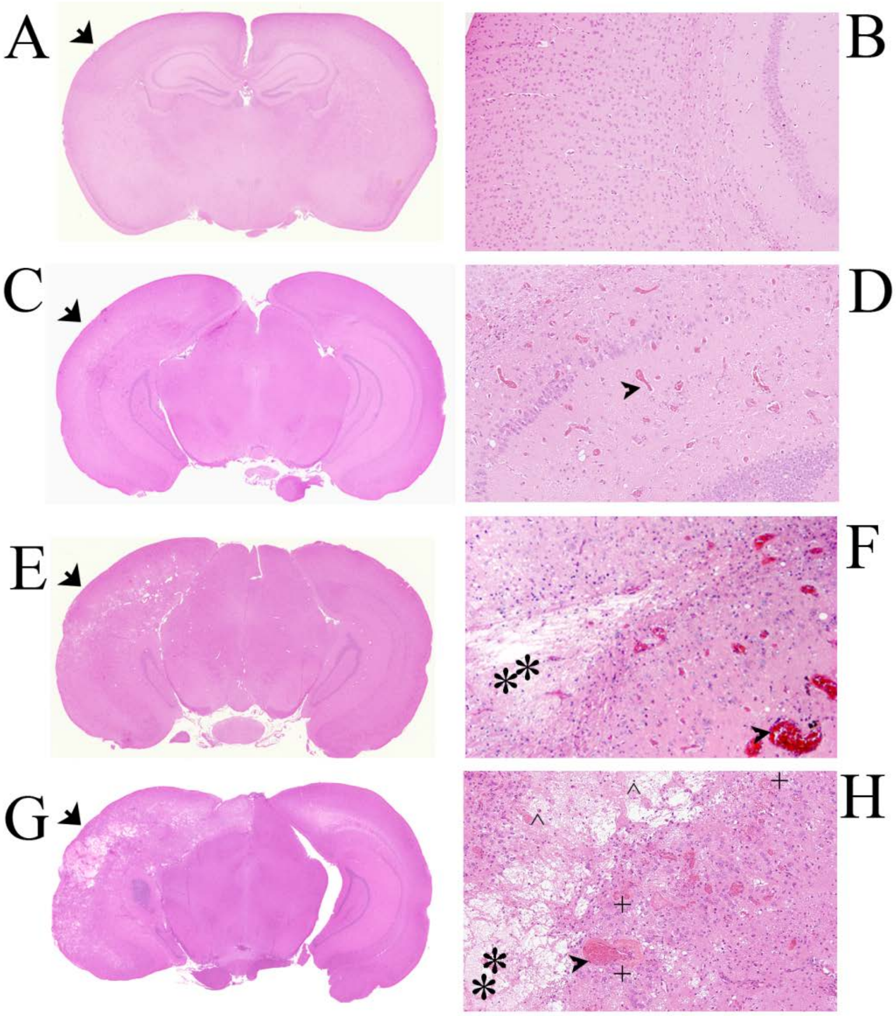

Figure 2.3. Representative pictures of irradiation damage of each grade. Panels A, C, E, and G are shown at 1x, with arrows indicating the irradiated hemisphere of the brain; Panels B, D, F, and H are shown at 100x magnification, thereby revealing more detail in the irradiated areas. Panels A and B (Grade 0): The irradiated brain shows no pathological changes. Panels C and D (Grade 1) in which the earliest histological events noted were micro-hemorrhages accompanied by increased numbers of telangiectatic vessels. (arrow). In grade 2 damage (Panels E and F), there were typically larger parenchymal hemorrhages (arrow), neuronal necrosis and tissue loss (*), with approximately one-half to two-thirds of the left hemisphere involved. Grade 3 damage

(Panels G and H) typically involves more extensive areas, with severe tissue damage, including fibrinoid vascular necrosis (+) and tissue loss (**).

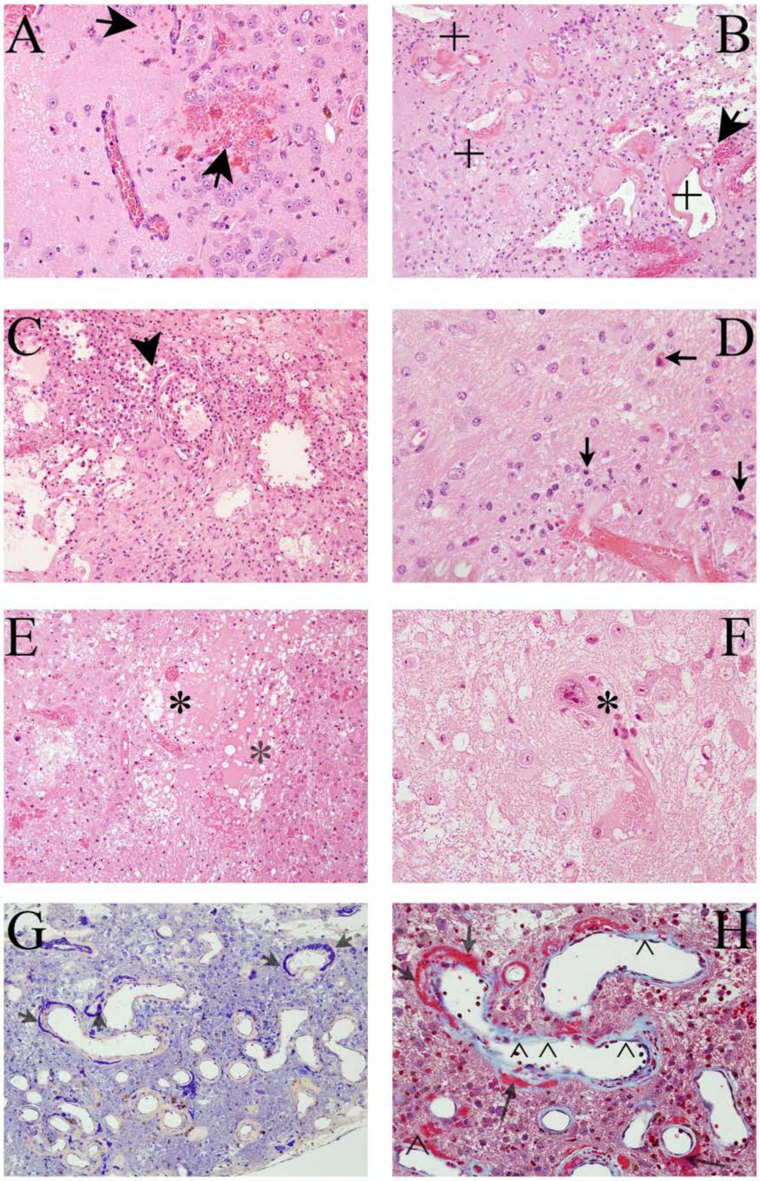

Figure 2.4. Pathological features in post-irradiation mouse brain. **A.** Micro-hemorrhages and dilated vessels (arrows, 20X). **B.** Hemorrhages (arrow) and fibrinoid vascular necrosis (+) (H&E staining, 20X). **C.** Activated microphages surrounding damaged tissues (arrow, 20x). **D.** Neuronal necrosis (arrows, 60X). **E.** Edema and hemorrhage (*, 20X). **F.** Cellular atypia (*, 60X). **G.** PTAH staining shows fibrinoid vascular necrosis in dark blue (arrows, 20X). H. Trichrome staining demonstrates fibrinoid vascular necrosis (red, arrows) and collagen in light

blue (^)(20X).

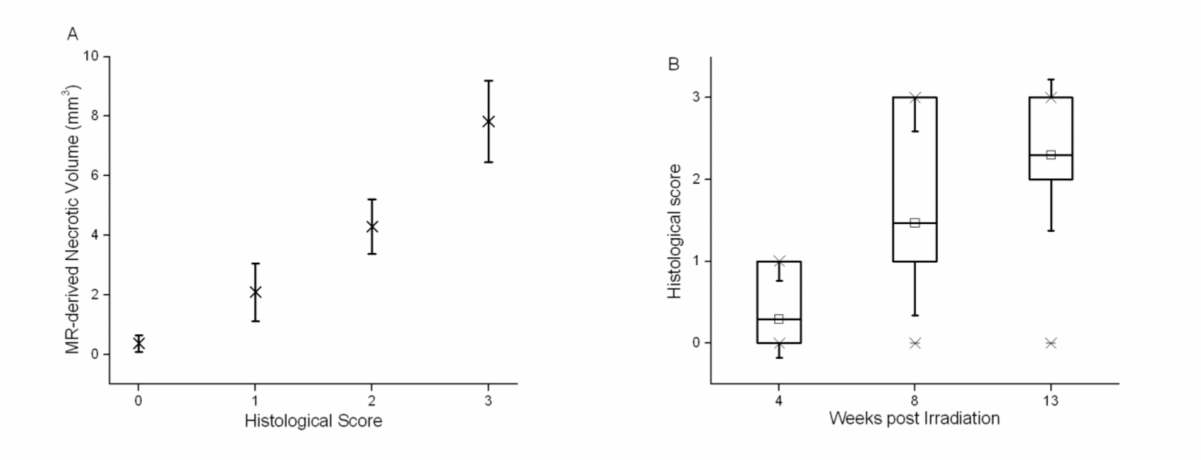

Figure 2.5. A. Correlation between MR-derived necrotic volumes and histological scores. MR-derived volumes, mean ± SD (n = 30, 37, 27, and 53 for Grade 0, 1, 2, and 3, respectively), of radiation necrosis vs. histological score for all the irradiated mice, regardless of radiation dosing and treatment schedules. B1. Correlation between histological scores and time post irradiation. Box-and-whisker plot of the histological scores for mice receiving 50/60-Gy of radiation, at 4, 8, and 13 weeks post irradiation. The 25th-75th percentiles are blocked by the box, and the whiskers identify the standard deviation.

References

1. Giglio P, Gilbert MR. Cerebral radiation necrosis. *Neurologist* 2003;9:180-188.
2. Stupp R, Mason WP, van den Beuf MJ. Radiotherapy plus concomitant and adjuvant temozolomide for newly diagnosed glioblastoma (vol 352, pg 19, 2005). *Annals of Oncology* 2005;16:949-949.
3. Stupp R, Hegi ME, Mason WP, *et al.* Effects of radiotherapy with concomitant and adjuvant temozolomide versus radiotherapy alone on survival in glioblastoma in a randomised phase III study: 5-year analysis of the EORTC-NCIC trial. *Lancet Oncology* 2009;10:459-466.
4. Tsuyuguchi N, Takami T, Sunada I, *et al.* Methionine positron emission tomography for differentiation of recurrent brain tumor and radiation necrosis after stereotactic radiosurgery - In malignant glioma. *Annals of Nuclear Medicine* 2004;18:291-296.
5. Rachinger W, Goetz C, Popperl G, *et al.* Positron emission tomography with O-(2-[F-18]fluoroethyl)-L-tyrosine versus magnetic resonance imaging in the diagnosis of recurrent gliomas. *Neurosurgery* 2005;57:505-511.

6. Kumar AJ, Leeds NE, Fuller GN, *et al.* Malignant gliomas: MR imaging spectrum of radiation therapy- and chemotherapy-induced necrosis of the brain after treatment. *Radiology* 2000;217:377-384.
7. Hein PA, Eskey CJ, Dunn JF, *et al.* Diffusion-weighted Imaging in the follow-up of treated high-grade gliomas: Tumor recurrence versus radiation injury. *American Journal of Neuroradiology* 2004;25:201-209.
8. Rahmathulla G, Marko NF, Weil RJ. Cerebral radiation necrosis: A review of the pathobiology, diagnosis and management considerations. *Journal of Clinical Neuroscience* 2013;20:485-502.
9. Shaw PJ, Bates D. Conservative Treatment of Delayed Cerebral Radiation Necrosis. *Journal of Neurology Neurosurgery and Psychiatry* 1984;47:1338-1341.
10. Siu A, Wind JJ, Iorgulescu JB, *et al.* Radiation necrosis following treatment of high grade glioma-a review of the literature and current understanding. *Acta Neurochirurgica* 2012;154:191-201.
11. But QC, Lieber M, Withers HR, *et al.* The efficacy of hyperbaric oxygen therapy in the treatment of radiation-induced late side effects. *International Journal of Radiation Oncology Biology Physics* 2004;60:871-878.
12. Tibbles PM, Edelsberg JS. Medical progress - Hyperbaric-oxygen therapy. *New England Journal of Medicine* 1996;334:1642-1648.
13. Kohshi K, Imada H, Nomoto S, *et al.* Successful treatment of radiation-induced brain necrosis by hyperbaric oxygen therapy. *Journal of the Neurological Sciences* 2003;209:115-117.
14. Mergenthaler P, Dirnagl U, Meisel A. Pathophysiology of stroke: lessons from animal models. *Metab Brain Dis* 2004;19:151-167.
15. van der Worp HB, Sena ES, Donnan GA, *et al.* Hypothermia in animal models of acute ischaemic stroke: a systematic review and meta-analysis. *Brain* 2007;130:3063-3074.
16. Clarke MF, Dick JE, Dirks PB, *et al.* Cancer stem cells--perspectives on current status and future directions: AACR Workshop on cancer stem cells. *Cancer Res* 2006;66:9339-9344.
17. Mori Y, Kondziolka D, Balzer J, *et al.* Effects of stereotactic radiosurgery on an animal model of hippocampal epilepsy. *Neurosurgery* 2000;46:157-165.
18. Wong CS, Van der Kogel AJ. Mechanisms of radiation injury to the central nervous system: implications for neuroprotection. *Molecular Interventions* 2004;4:273-284.
19. Jost SC, Hope A, Kiehl E, *et al.* A Novel Murine Model for Localized Radiation Necrosis and Its Characterization Using Advanced Magnetic Resonance Imaging. *International Journal of Radiation Oncology Biology Physics* 2009;75:527-533.
20. Zhou JY, Tryggestad E, Wen ZB, *et al.* Differentiation between glioma and radiation necrosis using molecular magnetic resonance imaging of endogenous proteins and peptides. *Nature Medicine* 2011;17:130-U308.
21. Kumar S, Arbab AS, Jain R, *et al.* Development of a novel animal model to differentiate radiation necrosis from tumor recurrence. *Journal of Neuro-Oncology* 2012;108:411-420.
22. Jiang X, Engelbach JA, Yuan L, *et al.* Anti-VEGF antibodies mitigate the development of radiation necrosis in mouse brain. *Clinical Cancer Research* 2013:in revision.
23. Conover WJ. Practical nonparametric statistics. 3rd ed. New York: Wiley; 1999.
24. Schollnberger H, Mitchel RE, Azzam EI, *et al.* Explanation of protective effects of low doses of gamma-radiation with a mechanistic radiobiological model. *Int J Radiat Biol*

2002;78:1159-1173.

Chapter 3 Anti-VEGF Antibodies Mitigate the Development of Radiation Necrosis

Declaration

Declaration by Xiaoyu Jiang

In the case of Chapter 3, the nature and extent of my contribution to the work was following:

Publication title	Anti-VEGF antibodies mitigate the development of radiation necrosis in mouse brain
Publication status	submitted
Nature and extent of candidate's contribution	Designed the experiments and performed the anatomic MR imaging and histogram analysis for quantitative comparison of the different progressions of radiation necrosis in control and antibodies-treated mice, and wrote the manuscript
Nature and extent of other co-authors' contribution	JA Engelbach[2] and J Cates[4] irradiated the mice; L Yuan[3] performed the H&E stains; F Gao[5,8] performed the statistical analysis; RE Drzymala[3,4], DE Hallahan[4,8], KM Rich[3,4], and RE Schmidt[6] advised the project and edited the manuscript; JJH Ackerman[1,2,7,8] and JR Garbow[2,8] initiated and supervised the project and edited the manuscript; Departments of [1]Chemistry, [2]Radiology, [3]Neurosurgery, [4]Radiation Oncology, [6]Neuropathology, and [7]Internal Medicine; [5]Division of Biostatistics; and the [8]Alvin J Siteman Cancer Center, Washington

	University, 1 Brookings Drive, St. Louis, MO, 63130; USA

Introduction

Radiation is a key component in the treatment of both benign and malignant central nervous system tumors, including gliomas, metastases, meningiomas, schwanomas, pituitary adenomas, and other less common neoplasms. Multiple radiation-treatment schemes have been developed to treat various neoplasms in the brain. These treatment protocols utilize a variety of different fractionation and conformational schemes designed to deliver focused radiation to regions in the brain to maximize control of tumor growth and minimize deleterious effects on normal brain tissue. Outcomes of these clinical protocols may be complicated by radiation effects on non-neoplastic tissue, resulting in a spectrum of phenotypes, ranging from minimal change with no observable clinical symptoms, to delayed radiation necrosis with severe neurological sequelae. The delayed effects from radiation may produce cerebral edema and necrosis of normal brain parenchyma, resulting in untoward neurologic effects that are difficult to differentiate from recurrent tumor growth.

Radiation necrosis, a delayed radiation neurotoxicity that can occur after radiation treatment of the CNS, can develop between 3 months and 10 years after radiotherapy, with most cases occurring in the first two years [1]. Necrosis following radiation is not uncommon, occurring in 3-24% of patients receiving focal irradiation [1]. The incidence may be threefold higher with concurrent chemotherapy [3, 112]. Currently, only limited options for therapeutic intervention are available for patients with symptomatic radiation necrosis. Surgical resection of necrotic tissue is often not possible due to the location of the necrosis in eloquent regions of the brain.

Prolonged treatment with corticosteroids is often employed [55], but is complicated by cushingoid side-effects, including weight gain, myopathy, immunosuppression, psychiatric disturbances, and occasionally arthritic sequelae, such as avascular necrosis affecting the shoulders and hips [56]. Hyperbaric oxygen treatment has also been considered as a therapeutic modality [57, 59]. However, it is cumbersome to deliver, expensive, and available in few medical centers. Its benefit has only been shown in a relatively small number of cases [58].

Two models of the pathogenesis of radiation necrosis have been proposed. These models involve radiation-induced injury to vasculature, radiation-induced injury to glial cells (apoptosis), or a combination thereof [123]. In particular, radiation necrosis has been associated with breakdown of the blood brain barrier, leading to increased vascular permeability and elevated levels of vascular endothelial growth factor (VEGF) [1, 5]. Elevated VEGF levels can, in turn, damage vascular endothelial cells and, together with subsequent narrowing of vessels due to fibrosis, can result in edema and necrosis [124].

Bevacizumab, a humanized monoclonal antibody against VEGF, was first approved by the FDA in 2004 for use in treating metastatic colorectal cancer. Since then, it has also been approved for the treatment of non-small-cell lung cancer, metastatic breast cancer, and recurrent glioblastoma [125]. Bevacizumab has been reported to normalize the vasculature, thereby enhancing the efficient delivery of drugs [126, 127]. There is clinical evidence that bevacizumab substantially decreases the effects of radiation necrosis [61-64, 128]. A recent randomized double-blind study of bevacizumab therapy for the patients with radiation necrosis [64] provided evidence of its efficacy in mitigating radiation necrosis. These studies relied on MR imaging, and, in particular, T1 post-gadolinium enhancement to characterize radiation necrosis, which is complicated by the presence of recurrent tumor. Also, because it is generally not possible to correlate time-course

MR observations with histologic findings in patients, these human studies lack information regarding the mechanisms of action of bevacizumab. Thus, further studies are needed to validate the effects and mechanisms of bevacizumab in the treatment of radiation necrosis.

We have recently developed a mouse model of delayed time-to-onset injury [101] that recapitulates the histologic features observed in patients suffering from CNS radiation necrosis. This model provides a platform for studies aimed at developing methods to identify/detect, monitor, protect against, and mitigate radiation necrosis, and distinguish it from tumor regrowth. In the work reported herein, this model is employed to validate the efficacy of both murine and humanized anti-VEGF-A monoclonal antibodies as mitigators of radiation necrosis following high-dose radiation treatment.

Materials and Methods

Animals

All studies were performed in accordance with the guidelines of the IACUC and in accordance with protocols approved by the Washington University Division of Comparative Medicine that met or exceeded American Association for the Accreditation of Laboratory Animal Care standards. Female Balb/c mice were used for the study and observed daily and weighed weekly to ensure that interventions were well tolerated.

Irradiation and Treatment

Mice were irradiated with the Leksell Gamma Knife® Perfexion™ (Elekta; Stockholm, Sweden; http://www.elekta.com/), a state-of-the-art unit used for stereotactic irradiation of patients with malignant brain tumors. Mice were supported on a specially designed platform mounted to the stereotactic frame that attaches to the treatment couch of the Gamma Knife. Mice were anesthetized with a mixture of ketamine (25 mg/kg), acepromazine (5 mg/kg) and xylazine (5 mg/kg), injected intraperitoneally 5 min before the start of irradiation. 35 female Balb/c mice were irradiated with either 60 Gy or 50 Gy, as described below, and the resulting brain parenchymal changes were characterized by both MRI and histology.

VEGF inhibitory monoclonal antibody

Bevacizumab (Genentech/Roche) is a humanized mAb (monoclonal antibody) that inhibits VEGF-A. Anti-VEGF antibody B20-4.1.1, heretofore referred to as B20-4.1.1, is a cross-species reactive, function-blocking mAb targeting both human and murine VEGF-A.

Experimental Outline

As part of the overall study, two different sets of experiments, designated as “A” and “B” were performed. In experiment “A”, two cohorts of mice (n=10 each) received a single 50-Gy dose (50% isodose) of Gamma Knife radiation. At this dose, the onset of radiation necrosis typically occurs approximately 4 weeks post-irradiation. Mouse cohort #1 was an irradiated, non-antibody (Ab)-treated, control group; cohort #2 received B20-4.1.1 (10 mg/kg), twice weekly, from 4-to-13 weeks post-irradiation. In experiment “B”, three cohorts of mice received a single fraction of 60-Gy radiation (50% isodose). At this dose, the onset of radiation necrosis typically occurs ~3 weeks post-irradiation. Mouse cohort #1 (n=5) was an irradiated, non-Ab-treated antibody, control group; cohort #2 (n=5) received B20-4.1.1 (10 mg/kg), twice weekly, from 3-to-10 weeks post-irradiation; cohort #3 (n=5) received bevacizumab (10 mg/kg, twice weekly) from 3-to-10 weeks post-irradiation. Antibodies were administered intraperitoneally.

MR Imaging

Images were collected in an Agilent/Varian (Santa Clara, CA) 4.7-T small-animal MR scanner equipped with a DirectDrive^{TM} console. The scanner is built around an Oxford Instruments (Oxford, United Kingdom) 33-cm, clear-bore magnet equipped with 21-cm inner diameter, actively shielded Agilent/Magnex gradient coils (maximum gradient, 28 G/cm; rise time approximately 200 ms) and Oy International Electric Company (IEC; Helsinki, Finland) model A-240 amplifiers (300 V and 300 A).

MRI data were collected using an actively decoupled coil pair: 1.5-cm outer diameter surface coil (receive) and a 9-cm inner diameter Helmholtz coil (transmit). Before the imaging experiments, mice were anesthetized with isoflurane/O_2 (3% [vol/vol]) and maintained on isoflurane/O_2 (1% [vol/vol]) throughout the experiments. Mice were restrained in a laboratory-constructed Teflon head holder with ear bars and a tooth bar. To maintain the body temperature of the mice at approximately 37°, mice placed on a water pad circulating warm water. Mice were injected intraperitoneally with 0.5 mL Omniscan (gadodiamide; GE Healthcare, Princeton, NJ) contrast agent, diluted 1:10 in sterile saline.

Non-Ab-treated mice treated with 50 Gy of radiation were imaged 4, 8, and 13 weeks post-irradiation. Ab-treated mice that had received 50 Gy of radiation were imaged 4, 5, 7, 9, 11, and 13 weeks post-irradiation. Mice that had received 60 Gy of radiation were imaged weekly from 3-to-10 weeks post-irradiation (non-Ab-treated mice were not imaged at week 9). Multislice, T2-weighted, spin-echo transaxial images were collected beginning ~3 minutes following gadodiamide administration with the following parameters: time to repetition [TR] = 1.5 s, time to echo [TE] = 0.05 s, field of view [FOV] = 1.5 x 1.5 cm^2, slice thickness = 0.5 mm, 21 slices to cover the whole brain; total acquisition time = 12 minutes. Multislice, T1-weighted, spin-echo transaxial images were then collected over 5 minutes with the following parameters: TR = 0.65 s, TE = 0.02 s, FOV = 1.5 x 1.5 cm^2, slice thickness = 0.5 mm, 21 slices to cover the whole brain.

Histology

Immediately after the last MR imaging session (13 weeks post-irradiation for mice receiving 50-Gy irradiation, 10 weeks post-irradiation for mice receiving 60-Gy irradiation), all the mice were perfused intracardially with 0.1 M Phosphate-buffered saline and formalin. The heads were then dissected and immersed in formalin for 24 hrs. All the brains were removed from skulls and embedded in paraffin. A single, 8-micron-thick coronal tissue section was taken from each brain near the radiation center and stained with hematoxylin and eosin (H&E) according to standard protocols. Histologic comparison of tissue sections was facilitated by the accurate targeting of radiation, ensuring that all histologic slices reflected the same anatomic features.

Statistical Analysis

For experiment “A”, Laird and Ware’s growth curve method [129] was used to compare the differences in the rates of progression of radiation necrosis, since the Ab-treated and non-Ab-treated irradiated cohorts were imaged at different time points. For experiment “B”, in addition to the overall rates of progression, two-way ANOVA for repeated measurement data was also used to compare the MRI-derived necrotic volumes between Ab-treated and non-Ab-treated irradiated cohorts, followed by ad hoc multiple comparisons for differences at specific time points. All the tests were two-sided and a p-value of 0.05 or less was taken to indicate statistical significance. The statistical analysis was performed using SAS 9.3 (SAS Institutes, Cary, NC).

Results

MRI detects radiation necrosis as image hyperintensity in T2-weighted images

Representative T2-weighted spin-echo images of control, bevacizumab-treated, and B20-4.1.1-treated mice, covering the same anatomic region of the brain and collected at 3, 6, and 10 weeks following a single 60 Gy dose of radiation, are shown in Figure 1. Hyperintense areas in these images correspond with region of radiation necrosis in the brain. Significant hyperintense regions are clearly seen in non-Ab-treated, control mice at 6 weeks post irradiation and these regions expand significantly in extent by 10 weeks. The images of mice treated with B20-4.1.1 show minimal hyperintensity, even at 10 weeks post irradiation, while the images of bevacizumab-treated mice describe an intermediate situation, showing no hyperintense regions at 6 weeks but small such regions at 10 weeks post irradiation.

Necrosis volumes can be measured quantitatively from MR images

For each set of T2-weighted spin-echo images, regions of interest were drawn around the entire brain in several contiguous image slices, chosen to include the entire hyperintense region. Each brain was divided along the midline into left (irradiated) and right (non-irradiated) hemispheres. The image intensity for each individual pixel in the left hemisphere was normalized by the average of the 25 pixels (5 x 5 square) including and immediately surrounding its mirror-image pixel in the right hemisphere, and histograms of normalized intensity for the irradiated hemisphere were constructed, as shown in Figure 2. The same analysis was performed on a cohort (n=10) of non-irradiated mice. The histogram of average intensity distribution for non-irradiated subjects, shown in Figure 2A, is symmetric; 99% of the pixels are distributed in the intensity range 0.6 – 1.4 about a normalized mean of 1.0. Therefore, an intensity threshold of 1.4 was chosen as the cutoff for normal brain tissue. For images of irradiated mice with/without treatment at different weeks post-irradiation, the number of pixels exceeding this threshold serves to measure the necrotic volume at each time point. Figure 2B shows image-pixel intensity histograms for B20-4.1.1- and bevacizumab-treated mice at 6 and 10 weeks following a single 60-Gy dose of radiation. The rates of progression of radiation necrosis over the designated time period can be derived from the slopes of least-squares fits of # pixels vs. time over the designated period.

Anti-VEGF antibodies slow the progression of radiation necrosis in irradiated brain tissue

Figure 3 shows the progression of the mean volumes of MRI-derived necrotic regions for non-Ab-treated and B20-4.1.1-treated mice in Experiment A, in which all the mice received a single, 50-Gy dose of radiation. There was almost no progression of radiation necrosis in the B20-4.1.1-treated cohort ($p < 0.0001$) compared to non-AB-treated control, indicating a significant mitigative effect due to the treatment.

Figure 4A shows the progression of the mean volumes of necrotic region for non-Ab-treated, bevacizumab-treated, and B20-4.1.1-treated cohorts in Experiment B, in which all the mice received a single 60 Gy dose of radiation. The overall slope of the progression curve for B20-4.1.1-treated mice is slightly negative, demonstrating the mitigative effect of B20-4.1.1 where the treated cohort had a greatly diminished volume of necrosis at week 10 post-irradiation compared to non-Ab-treated controls ($p < 0.0001$, week 10). Bevacizumab also slows the overall rate of progression ($p<0.0001$, week 10). Considering the initial 3-7 week period post-irradiation, bevacizumab has the same mitigative effect as B20-4.1.1 ($p = 0.8$, week 7). However, for the latter 7-10 week period, radiation-induced necrosis developed at a higher rate than in the B20-

4.1.1-treated cohort ($p<0.0001$, week 10), indicating that the mitigative effect of bevacizumab was weaker than B20-4.1.1 in the late period following the initiation of treatment.

These effects are evident in Figure 4B, in which the rates of progression of radiation necrosis for the three cohorts are plotted. The progression rate for the B20-4.1.1-treated cohort was substantially reduced relative to the non-Ab-treated cohort over both the 3-7 week ($p<0.0001$) and 7-10 week periods ($p=0.0002$) post-irradiation. While bevacizumab treatment slowed the rate of progression relative to the non-Ab-treated cohort during the initial 3-7 week period ($p<0.0001$), its effect was lost over the latter 7-10 week period ($p=0.2$). It is apparent that in mice, B20-4.1.1 was a more potent mitigator of radiation necrosis compared to bevacizumab.

Histology reveals that anti-VEGF antibodies mitigate radiation necrosis in irradiated brain tissue

Figure 5(A) shows representative 2x (top), 10x (middle) H&E histologic images and corresponding T2W MR images (bottom) for non-Ab-treated, bevacizumab -treated, and B20-4.1.1-treated mice at 10 weeks following a single, 60-Gy dose of radiation. Corresponding histologic images and T2-weighted images of control and B20-4.1.1 –treated mice following a single, 50-Gy fraction of radiation are shown in Figure 5(B). The irradiated hemispheres of the control mice demonstrated many of the classic histologic features of radiation necrosis, including fibrinoid vascular necrosis (black arrow), vascular telangiectasia (yellow arrows), *hemorrhage (red arrow)*, and loss of neurons and edema (blue arrows) [4]. In contrast, the irradiated hemisphere of the bevacizumab-treated mouse showed only modest tissue damage and the irradiated hemisphere of the B20-4.1.1-treated mouse displayed no visible tissue damage. These histologic findings support the MR data shown in Figs. 3 and 4, demonstrating a significant mitigative effect of anti-VEGF-A therapy.

Discussion

Surgery, chemotherapy, and/or radiation are modalities utilized in treatment protocols for patients with brain neoplasms. The risk of late-onset radiation necrosis significantly limits the efficiency of such treatment. The identification of agents that mitigate the delayed effects of radiation-induced changes on normal tissue, while not reducing the therapeutic efficacy of radiation on tumor tissue, could significantly increase the effectiveness of radiation paradigms. Currently, the clinical therapeutic options for treating radiation necrosis are limited.

It has been suggested that radiation necrosis results from local tissue injury characterized by disruption of the blood-brain barrier and consequent tissue edema. Endothelial cell death, which results in breakdown of the blood-brain barrier, edema, and hypoxia and enhanced expression of VEGF has been described as an important step in the development of radiation necrosis [5]. The mitigative potential of anti-VEGF therapy using Bevacizumab in the treatment of radiation necrosis has been shown in several retrospective human studies and a recent prospective human study in a small number of patients [61-64], though these studies lacked statistical power. MRI monitoring of the onset and progression of radiation necrosis, in concert with Gamma Knife irradiation, offers an attractive strategy for validating and optimizing anti-VEGF-Ab therapy. We have established an animal model that faithfully reproduces the histology of radiation necrosis observed in patients. Herein, we demonstrate that anti-VEGF antibodies can delay the onset of radiation necrosis and believe that the results of mitigation studies in the mouse may be immediately and readily translatable.

In this study, the onset and progression of radiation necrosis in mouse brain were characterized by the volume of hyperintense regions on T2-weighted images. Characterization employing contrast-enhanced T1-weighted images yielded essentially equivalent findings (data not shown). The greatly reduced progression of radiation necrosis in treated mice, as measured longitudinally by *in vivo* MR imaging, and the much lighter tissue damage observed in H&E-stained tissue sections for bevacizumab- and B20-4.1.1-treated mice, demonstrated the efficacy of anti-VEGF-A therapy. B20-4.1.1 has a better mitigative effect than bevacizumab in the mouse model of radiation necrosis. The mitigative effects of bevacizumab disappeared approximately 4 weeks after the start of treatment (Fig. 4). This may be due to an anti-idiotypic immunogenic response [130-132], whereby murine antibodies directed against the antigen specific part of bevacizumab are produced, thereby inhibiting its binding to mouse VEGF. The greater therapeutic efficacy of B20-4.1.1 is likely due to its higher affinity for mouse VEGF-A [133].

Although the results of the present study demonstrate that bevacizumab and B20-4.1.1 can significantly reduce the progression of radiation necrosis, the mechanism of the mitigative effect of these VEGF inhibitors remains undetermined and requires further investigation. Future studies that address mechanism of action will include Dynamic Contrast-Enhanced MRI, an imaging method for quantitatively measuring vascular permeability [27, 79] and specific histological stains targeting permeability, such as Evans Blue [134].

Outstanding questions also remain regarding the ideal dosing schemes and the treatment periods for anti-VEGF-Ab therapy. Multiple dosing schemes, ranging from 5 mg/kg to 10 mg/kg have been reported in the treatments of tumor and radiation necrosis in both human [61, 64] and animal studies [135]. Typically, bevacizumab, with a half-life of approximately 20 days in humans, is administered once every 2 or 3 weeks in patients [61, 64, 136], and once or twice weekly in mice [60, 135]. For our mitigation study, a high-end dosing scheme (10 mg/kg, twice weekly) was chosen and demonstrated promising mitigative effects on radiation necrosis in mice.

Nonetheless, minimizing the dose required to effective control the progression of necrosis will reduce patient costs and potential side effects, thereby improving the likelihood of effective clinical translation. Studies measuring the effects of using lower doses of B20-4.1.1 in our mouse model are ongoing in our lab. Also, in the current studies, irradiated mice were treated with bevacizumab or B20-4.1.1 for 7 or 8 weeks, beginning with the first radiographic sign of radiation necrosis. However, the mitigative effectiveness found upon initiating the treatment earlier (e.g., immediately following irradiation) or stopping the treatment after a fixed period of time (e.g., 4 weeks) remain to be investigated.

Conclusion

The data in this study demonstrate a significant mitigative effect of both bevacizumab and B20-4.1.1 in a mouse model of radiation necrosis. By reducing the development of necrosis following irradiation, anti-VEGF-Ab therapy may overcome the deleterious effects of focal irradiation to effectively treat lesions with fewer side effects. Efforts to optimize dosing schemes and treatment periods and elucidate the mechanisms of mitigative effect of bevacizumab and B20-4.1.1 in the treatment of radiation necrosis in this mouse model are ongoing.

Acknowledgments

We thank Drs. Dinesh Thotala and Carlos Perez-Torres for valuable discussions and feedback. This project has been supported by NIH grants R01 CA155365 (JRG), R01 CA174966 (DEH), and R01 CA140220-01 (DEH), and funding from the Alvin J. Siteman Cancer Center, an NCI-comprehensive cancer center, P30 CA091842, the Barnes-Jewish Hospital Foundation Cancer Frontier Fund, and Elekta Instruments AB (Stockholm, Sweden). We gratefully acknowledge Genentech (South San Francisco, CA) for donation of anti-VEGF antibody B20-4.1.1.

Complementary data

DCE MR imaging

For DCE MR imaging, a 2D T1-weighted fast spoiled gradient-echo sequence was used to obtain dynamic sets of 3 slices with a slice thickness of 1.0 mm, field of view of 15 x 15 mm^2, matrix of 64 x 64, TR = 20 ms, TE = 3.10 ms, and Flip angle = 20 degree. 200 sets of images were collected continuously with about 5 s for each set. 0.17 mL Omniscan (gadodiamide; GE Healthcare, Princeton, NJ) contrast agent was injected via tail vein within 1 s at the 10th set of images.

Anti-VEGF antibodies decrease the vasculature permeability in the necrotic region

Figure 3.6 compares the endothelial transfer constant (K^{trans}) maps for control (left) and B20-4.1.1-treated (right) mice at 13 weeks post irradiation. Large high K^{trans} regions associated to radiation-induced BBB breakdown are indentified in the irradiated hemispheres of control mice. In contrast, the K^{trans} values are close to zero in both irradiated and contralateral hemispheres of B20-4.1.1-treated mice, indicating that B20-4.1.1 significantly decreased the permeability of BBB in irradiated mouse brain.

The K^{trans} maps for the same animal before and after one-time B20-4.1.1 treatment are shown in Figure 3.7. It is evident that the K^{trans} values in the irradiated hemisphere decreased dramatically after a single B20-4.1.1 treatment. Further, the hyperintense regions on T2-weighted images associated with necrotic regions is larger at 7 weeks post irradiation than 6 weeks, indicating that a single treatment cannot mitigate the progression of necrosis.

Figures

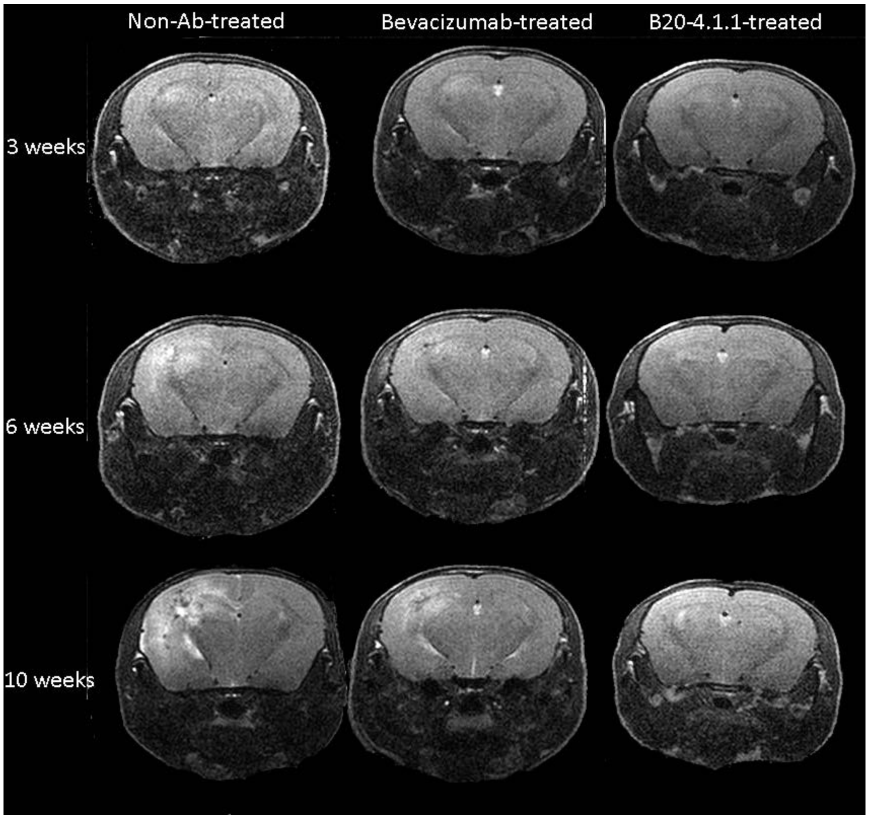

Figure 3.1. MRI can detect radiation necrosis in irradiated brain**.** Representative, transaxial, T2-weighted spin-echo images acquired longitudinally from non-Ab-treated, bevacizumab-treated, and B20-4.1.1-treated mice at 3 (top), 6 (middle) and 10 weeks (bottom) following a single 60 Gy at (50% isodose) of radiation. Slices are chosen to display the same anatomic region of the brain at all three time points.

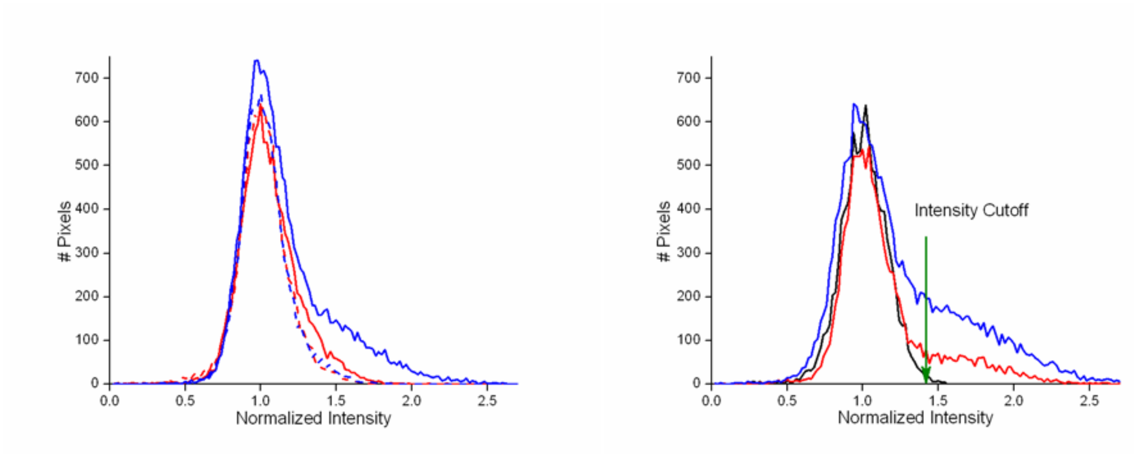

Figure 3.2. Histogram analysis enables quantitative MRI measurement of necrotic volume. (A) Image-pixel intensity histograms for the same non-Ab-treated mouse at 6 and 10 weeks following a single 60 Gy of radiation (red, blue) and average intensity histogram for 10 non-irradiated non-Ab-treated mice (black). The intensity cutoff used to define hyperintense pixels, corresponding to necrotic tissue, is indicated by the labeled arrow at a normalized intensity of 1.4. (B) Image-pixel intensity histograms for the same B20-4.1.1-treated (red) and bevacizumab-treated (blue) mice at 6 (dash line) and 10 (solid line) weeks following a single 60-Gy dose of radiation.

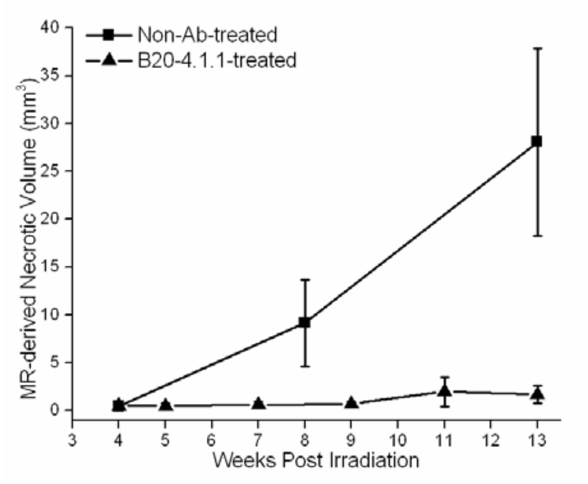

Figure 3.3. MRI-derived necrotic volumes in mice irradiated hemispherically with a single 50-Gy dose of GK radiation. MRI-defined volumes, mean ± SD (n = 10), of radiation necrosis vs. time post-irradiation for non-Ab-treated and B20-4.1.1-treated mice; all the mice received a single 50-Gy of radiation (50% isodose). Compared to non-Ab-treated control, almost no progression of radiation necrosis in the B20-4.1.1-treated cohort ($p<0.0001$) was observed.

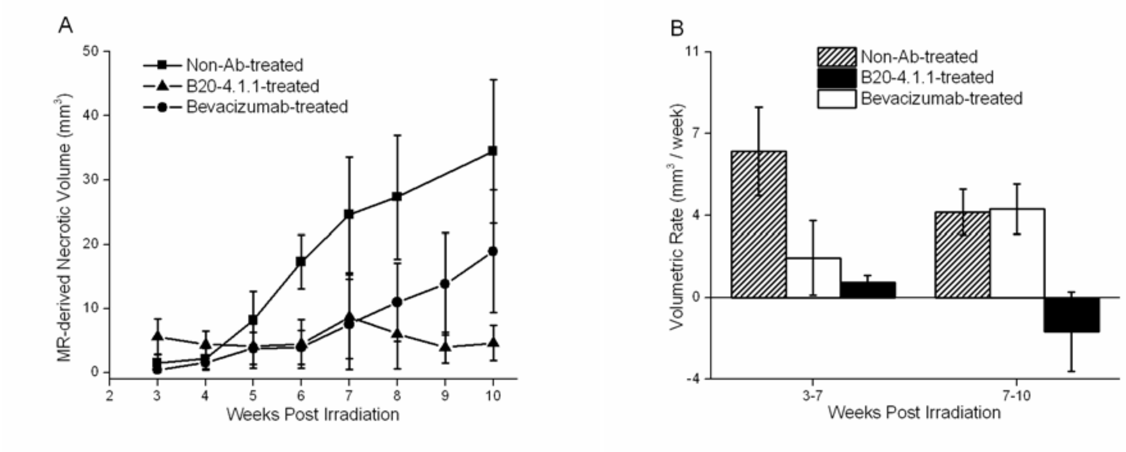

Figure 3.4. MRI-derived necrotic volumes in mice irradiated hemispherically with a single 60-Gy dose of GK radiation. (A) MRI-defined volumes, mean ± SD (n = 5), of radiation necrosis vs. time post-irradiation for non-Ab-treated, bevacizumab -treated, and B20-4.1.1-treated mice; all the mice received a single 60-Gy of radiation (50% isodose). At the 0.0001 level, MR-derived necrotic volumes for both treated cohorts were significantly smaller than the non-Ab-treated cohort at week 6, 7, 8, and 10 post-irradiation. The differences in the volumes between bevacizumab-treated and B20-4.1.1-treated cohorts was significant at week 10 post-irradiation (p<0.0001), but not significant at week 7 post-irradiation (p = 0.8), indicating that the mitigative effect of bevacizumab was weaker than B20-4.1.1 in the late period following the initiation of treatment. (B) MRI-defined volumetric rate of radiation necrosis progression, mean ± SD (n = 5), derived from the slope of the curves in the left panel, for the 3-7 and 7-10 week periods. The progression rates for both treated cohorts were significantly reduced relative to the non-Ab-treated cohort over the 3-7 week period (P<0.0001) post irradiation. For the 7-10 week period post irradiation, only B20-4.1.1 treatment slowed the rate of progression relative to the control (p=0.0002).

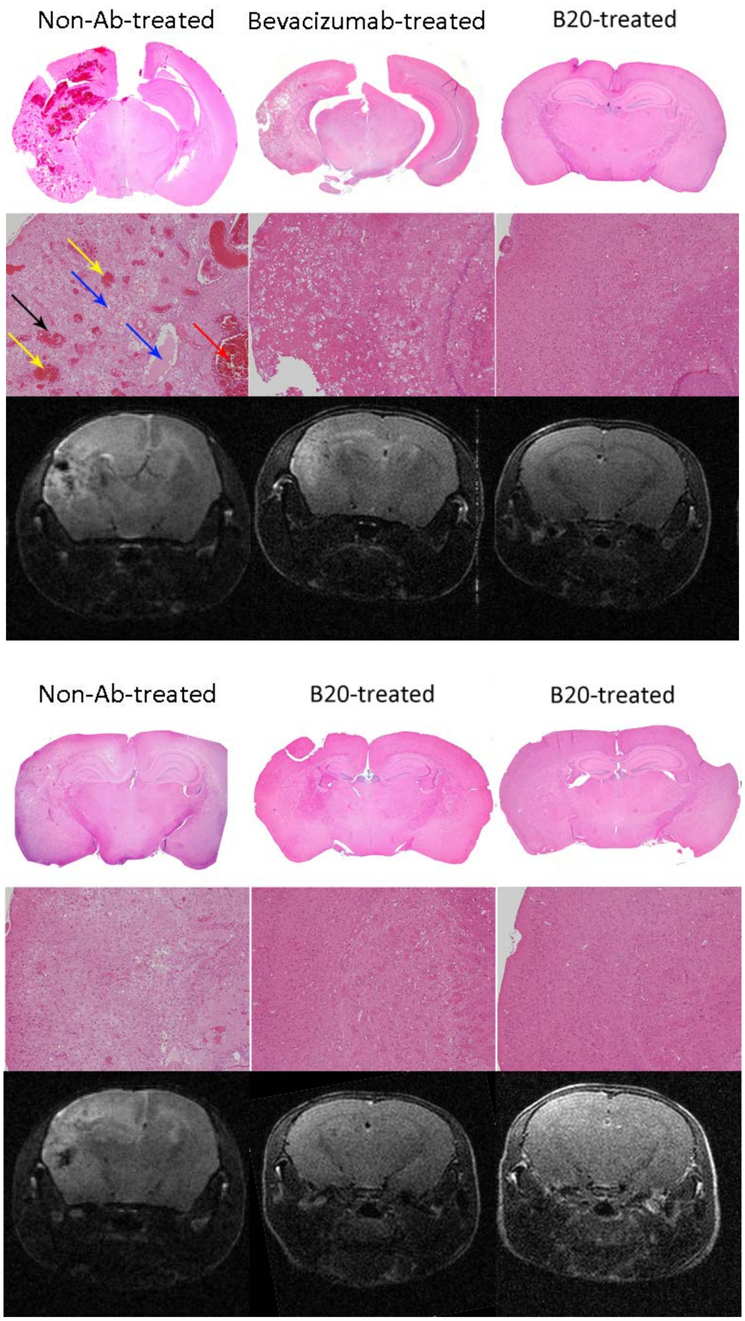

Figure 3.5. H&E-stained sections display characteristic histologic features of radiation necrosis and demonstrate mitigation by anti-VEGF Ab. (A) Representative 2x (top) and 10x (middle) H&E histology slices chosen near the radiation isocenter, and corresponding T2W images

(bottom) for non-Ab-treated, bevacizumab-treated, and B20-4.1.1-treated mice at 10 weeks following a single 60-Gy fraction of radiation. (B) Representative 2x (top) and 10x (middle) H&E histology slices, and corresponding T2W images (bottom) for one control and two B20-4.1.1-treated mice at 13 weeks following a single 50-Gy fraction of radiation. The irradiated hemispheres of the control mice show many of the histologic features that are characteristic of radiation necrosis, including fibrinoid vascular necrosis (black arrow), vascular telangiectasia (yellow arrows), *hemorrhage (red arrow)*, loss of neurons and edema (blue arrows). In addition, the tissue injury observed on the histology slices are highly correlated with the hyperintense regions on T2W images.

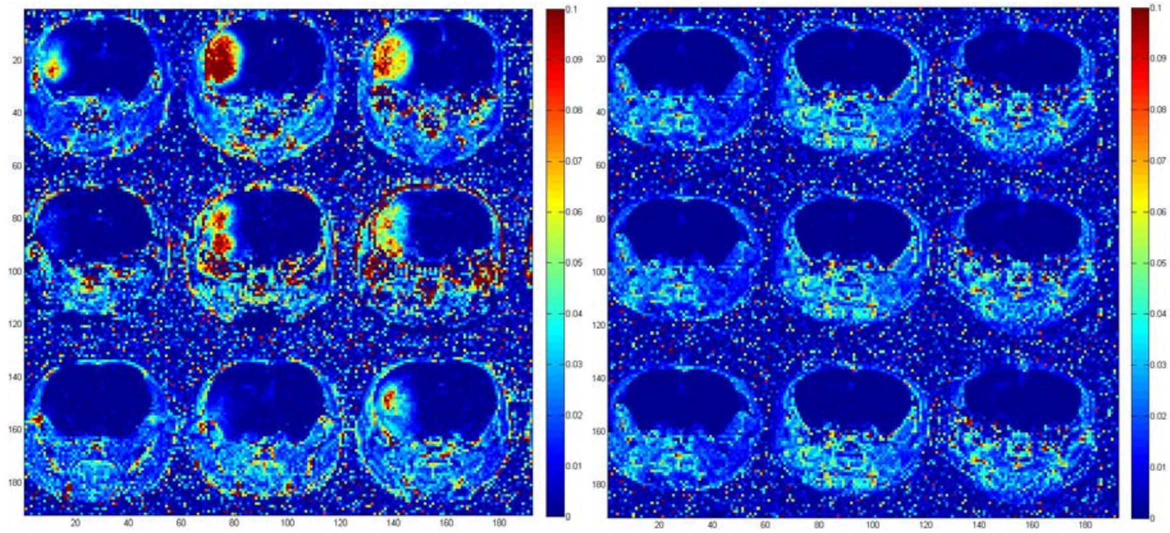

Figure 3.6. The K^{trans} maps. (Left) different columns represent three contiguous slices from the same animal, and different rows represent three control mice; (Right) different columns represent three contiguous slices from the same animal, and different rows represent three B20-4.1.1-treated mice.

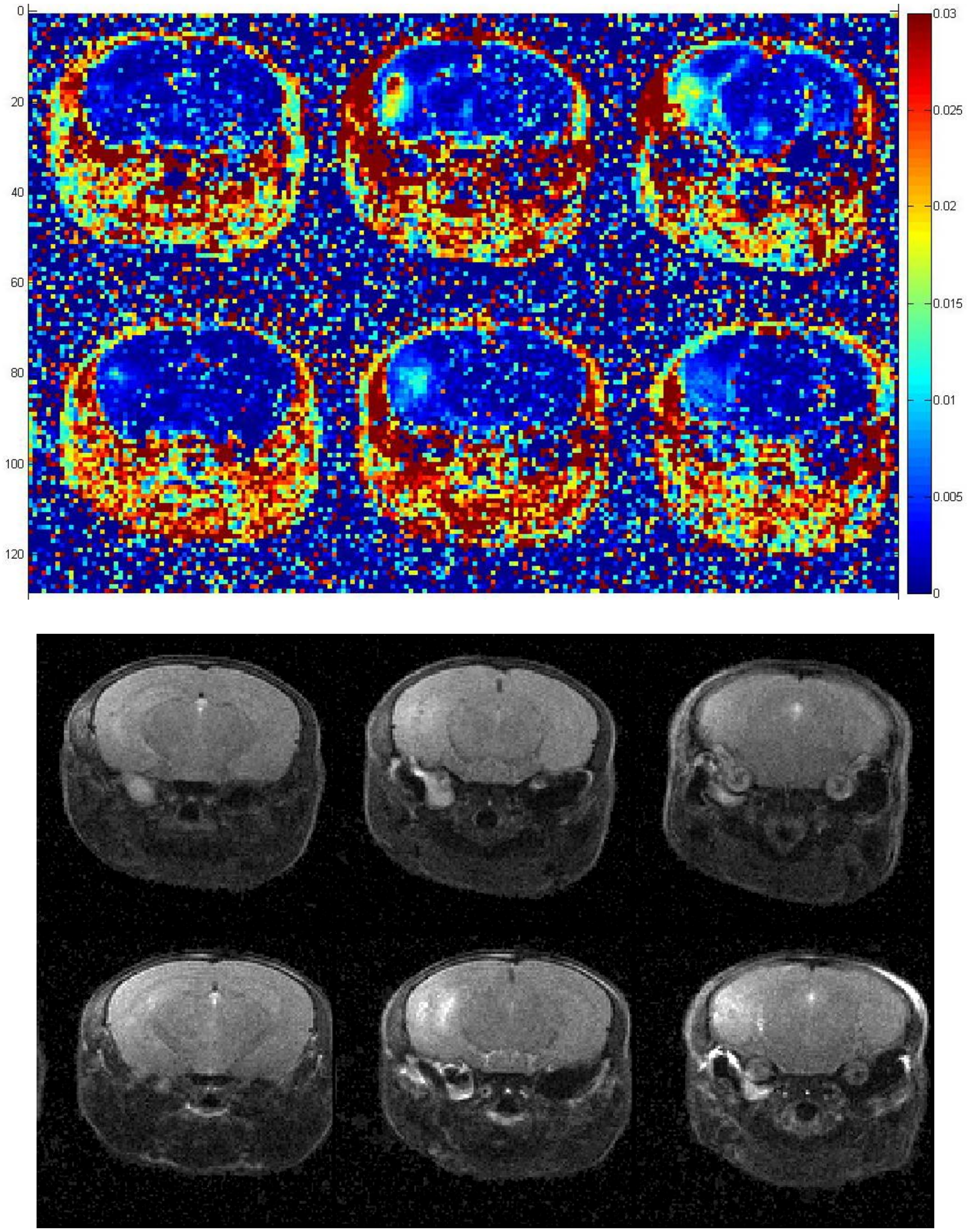

Figure 3.7. The K^{trans} maps (A) and corresponding T2-weighted images (B) for the same mouse, before (top) and after (bottom) one single B20-4.1.1 treatment. Different columns represent three contiguous slices.

References

1. Giglio P, Gilbert MR. Cerebral radiation necrosis. Neurologist. 2003;9:180-8.

2. Stupp R, Mason WP, van den Beuf MJ. Radiotherapy plus concomitant and adjuvant temozolomide for newly diagnosed glioblastoma (vol 352, pg 19, 2005). Annals of Oncology. 2005;16:949-.

3. Stupp R, Hegi ME, Mason WP, van den Bent MJ, Taphoorn MJB, Janzer RC, et al. Effects of radiotherapy with concomitant and adjuvant temozolomide versus radiotherapy alone on survival in glioblastoma in a randomised phase III study: 5-year analysis of the EORTC-NCIC trial. Lancet Oncology. 2009;10:459-66.

4. Shaw PJ, Bates D. Conservative Treatment of Delayed Cerebral Radiation Necrosis. Journal of Neurology Neurosurgery and Psychiatry. 1984;47:1338-41.

5. Siu A, Wind JJ, Iorgulescu JB, Chan TA, Yamada Y, Sherman JH. Radiation necrosis following treatment of high grade glioma-a review of the literature and current understanding. Acta Neurochirurgica. 2012;154:191-201.

6. Tibbles PM, Edelsberg JS. Medical progress - Hyperbaric-oxygen therapy. New England Journal of Medicine. 1996;334:1642-8.

7. But QC, Lieber M, Withers HR, Corson K, van Rijnsoever M, Elsaleh H. The efficacy of hyperbaric oxygen therapy in the treatment of radiation-induced late side effects. International Journal of Radiation Oncology Biology Physics. 2004;60:871-8.

8. Kohshi K, Imada H, Nomoto S, Yamaguchi R, Abe H, Yamamoto H. Successful treatment of radiation-induced brain necrosis by hyperbaric oxygen therapy. Journal of the Neurological Sciences. 2003;209:115-7.

9. Rahmathulla G, Marko NF, Weil RJ. Cerebral radiation necrosis: A review of the pathobiology, diagnosis and management considerations. J Clin Neurosci. 2013;20:485-502.

10. Wong CS, Van der Kogel AJ. Mechanisms of radiation injury to the central nervous system: implications for neuroprotection. Molecular Interventions. 2004;4:273-84.

11. Remler MP, Marcussen WH, Tiller-Borsich J. The late effects of radiation on the blood brain barrier. Int J Radiat Oncol Biol Phys. 1986;12:1965-9.

12. Norden AD, Drappatz J, Wen PY. Antiangiogenic therapies for high-grade glioma. Nat Rev Neurol. 2009;5:610-20.

13. Jain RK. Normalization of tumor vasculature: An emerging concept in antiangiogenic therapy. Science. 2005;307:58-62.

14. Dings RPM, Loren M, Heun H, McNiel E, Griffioen AW, Mayo KH, et al. Scheduling of radiation with angiogenesis inhibitors anginex and avastin improves therapeutic outcome via vessel normalization. Clinical Cancer Research. 2007;13:3395-402.

15. Gonzalez J, Kumar AJ, Conrad CA, Levin VA. Effect of bevacizumab on radiation necrosis of the brain. International Journal of Radiation Oncology Biology Physics. 2007;67:323-6.

16. Torcuator R, Mohan YS, Lee I, Rock J, Doyle T, Anderson J, et al. Initial experience with bevacizumab treatment for biopsy-confirmed cerebral radiation necrosis. Neuro-Oncology. 2007;9:580-1.

17. Jeyaretna DS, Curry WT, Batchelor TT, Stemmer-Rachamimov A, Plotkin SR. Exacerbation of Cerebral Radiation Necrosis by Bevacizumab. Journal of Clinical Oncology. 2011;29:E159-E62.

18. Levin VA, Bidaut L, Hou P, Kumar AJ, Wefel JS, Bekele BN, et al. Randomized Double-Blind Placebo-Controlled Trial of Bevacizumab Therapy for Radiation Necrosis of the Central Nervous System. International Journal of Radiation Oncology Biology Physics. 2011;79:1487-95.

19. Ananthnarayan S, Bahng J, Roring J, Nghiemphu P, Lai A, Cloughesy T, et al. Time course of imaging changes of GBM during extended bevacizumab treatment. Journal of Neuro-Oncology. 2008;88:339-47.

20. Jost SC, Hope A, Kiehl E, Perry A, Travers S, Garbow JR. A Novel Murine Model for Localized Radiation Necrosis and Its Characterization Using Advanced Magnetic Resonance Imaging. International Journal of Radiation Oncology Biology Physics. 2009;75:527-33.

21. Laird NM, Ware JH. Random-effects models for longitudinal data. Biometrics. 1982;38:963-74.

22. Perry A, Schmidt RE. Cancer therapy-associated CNS neuropathology: an update and review of the literature. Acta Neuropathologica. 2006;111:197-212.

23. Shawler DL, Bartholomew RM, Smith LM, Dillman RO. Human Immune-Response to Multiple Injections of Murine Monoclonal Igg. Journal of Immunology. 1985;135:1530-5.

24. Herlyn D, Lubeck M, Sears H, Koprowski H. Specific Detection of Anti-Idiotypic Immune-Responses in Cancer-Patients Treated with Murine Monoclonal-Antibody. Journal of Immunological Methods. 1985;85:27-38.

25. Fagerberg J, Ragnhammar P, Liljefors M, Hjelm AL, Mellstedt H, Frodin JE. Humoral anti-idiotypic and anti-anti-idiotypic immune response in cancer patients treated with monoclonal antibody 17-1A. Cancer Immunology Immunotherapy. 1996;42:81-7.

26. Yu LL, Wu XM, Cheng ZY, Lee CV, LeCouter J, Campa C, et al. Interaction between bevacizumab and murine VEGF-A: A reassessment. Investigative Ophthalmology & Visual Science. 2008;49:522-7.

27. O'Connor JPB, Jackson A, Parker GJM, Jayson GC. DCE-MRI biomarkers in the clinical evaluation of antiangiogenic and vascular disrupting agents. British Journal of Cancer. 2007;96:189-95.

28. Padhani AR, Husband JE. Dynamic contrast-enhanced MRI studies in oncology with an emphasis on quantification, validation and human studies. Clinical Radiology. 2001;56:607-20.

29. Xu QW, Qaum T, Adamis AP. Sensitive blood-retinal barrier breakdown quantitation using Evans blue. Investigative Ophthalmology & Visual Science. 2001;42:789-94.

30. de Groot JF, Fuller G, Kumar AJ, Piao Y, Eterovic K, Ji YJ, et al. Tumor invasion after treatment of glioblastoma with bevacizumab: radiographic and pathologic correlation in humans and mice. Neuro-Oncology. 2010;12:233-42.

31. Ferrara N, Hillan KJ, Gerber HP, Novotny W. Discovery and development of bevacizumab, an anti-VEGF antibody for treating cancer. Nature Reviews Drug Discovery. 2004;3:391-400.

32. Ferrara N, Hillan KJ, Novotny W. Bevacizumab (Avastin), a humanized anti-VEGF monoclonal antibody for cancer therapy. Biochemical and Biophysical Research Communications. 2005;333:328-35.

Chapter 4 A GSK-3β inhibitor Protects Against Radiation Necrosis in Mouse Brain

Declaration

Declaration by Xiaoyu Jiang

In the case of Chapter 3, the nature and extent of my contribution to the work was following:

Publication title	A GSK-3β inhibitor protects against radiation necrosis in mouse brain
Publication status	submitted
Nature and extent of candidate's contribution	Designed the experiments and performed the anatomic MR imaging and histogram analysis for quantitative comparison of the different progressions of radiation necrosis in control and SB415286-treated mice, and wrote the manuscript
Nature and extent of other co-authors' contribution	CJ Perez-Torres[2] and D Thotala[3] tested the effect of SB415286 in the radiotherapy of tumor tissue; JA Engelbach[2] and J Cates[3] irradiated the mice; L Yuan[4] performed the H&E stains; F Gao[5,8] performed the statistical analysis; RE Drzymala[3,4], DE Hallahan[3,8], KM Rich[3,4], and RE Schmidt[6] advised the project and edited the manuscript; JJH Ackerman[1,2,7,8] and JR Garbow[2,8] initiated and supervised the project and edited the manuscript; Departments of [1]Chemistry, [2]Radiology, [3]Radiation Oncology, [4]Neurosurgery, [6]Neuropathology, and [7]Internal Medicine, [5]Division of Biostatistics; and the [8]Alvin J Siteman Cancer Center, Washington

	University, 1 Brookings Drive, St. Louis, MO, 63130; USA

Introduction

Radiation necrosis (RN) is a major complication of radiotherapy [1] that often limits radiation dose. The incidence of reported RN ranges from 3-24% of patients following focal irradiation [56, 115, 137, 138] and may be up to threefold higher with concurrent chemotherapy [3, 112]. A number of treatment options for RN are available [55-58, 62-64], however each therapy has limitations and introduces potential complications for patients. Current interventions have limited success in mitigating RN.

Proposed mechanisms leading to RN in the brain include radiation-induced injury to vasculature and apoptosis [116]. In particular, RN has been associated with acute apoptosis of oligodendroglial precursor cells that results in: (i) loss of mature oligodendrocytes, (ii) demyelination and white-matter necrosis [139], and (iii) damaged astrocytes that result in breakdown of the blood brain barrier (BBB) [140, 141]. BBB breakdown is associated with elevated levels of vascular endothelial growth factor (VEGF) and, together with subsequent narrowing of vessels due to fibrosis, can result in edema and necrosis [5]. Inhibiting the apoptotic process of glial cells may prevent or ameliorate the development of radiation necrosis.

Others and we have studied neuroprotection by GSK-3β inhibitors, which increase neuronal cell viability [26-29, 44]. GSK-3β is a multifunctional serine/threonine kinase originally identified as a regulator of glycogen metabolism [142]. GSK-3β is widely expressed in most tissues, however, it is expressed abundantly in brain and especially in neurons, due to its vital role in neuronal signalling [143].

GSK-3β has been shown to induce apoptosis in response to a wide variety of conditions [144-146] including irradiation[147]. In cell culture studies, apoptosis was either attenuated or prevented by inhibiting GSK-3β in primary [148] and hippocampal (HT-22) neurons,[149]. GSK-3β inhibition has been demonstrated to enhance survival of irradiated endothelial cells due to attenuated apoptosis and to protect cells *in vivo* from radiation-induced apoptosis [150].

GSK-3β inhibitors are utilized for the treatment of various diseases [151-153], with ongoing development of new GSK-3β inhibitors that are in various phases of clinical trials[153]. Accordingly, GSK-3β inhibition represents a potential therapeutic approach in the treatment of radiation necrosis.

A novel animal model of radiation necrosis has been developed in our lab [101] that accurately recapitulates the classic histologic features of radiation necrosis observed clinically and provides a robust platform to test the efficacy of neuroprotective drugs. This model is employed herein to validate the neuroprotective effect of SB 415286, a specific GSK-3β inhibitor, in mouse brain following high-dose radiation treatment. Further, the effect of SB 415286 on the effectiveness of radiation therapy in tumor bearing mice is investigated.

Materials and Methods

Animals

Female Balb/c mice were used for the study and observed daily and weighed weekly to ensure that interventions were well tolerated.

Irradiation and treatment

Mice were irradiated with the Leksell Gamma Knife® Perfexion™ (Elekta; Stockholm, Sweden; http://www.elekta.com/), a state-of-the-art device used for stereotactic irradiation of patients with malignant brain tumors. Mice were supported on a specially designed platform mounted to the stereotactic frame that attaches to the treatment couch of the Gamma Knife (GK). Mice were anesthetized with a mixture of ketamine (25 mg/kg), acepromazine (5 mg/kg), and xylazine (5 mg/kg), injected intraperitoneally 5 min before the start of irradiation. Mice were irradiated with a single 45-Gy fraction targeted to the left hemisphere (brain). The resulting brain parenchymal changes were monitored and characterized by MRI and histology.

GSK-3β□ inhibitor

SB 415286 (GlaxoSmithKline; London, UK) is a potent and selective cell-permeable, ATP-competitive GSK-3β inhibitor with an IC_{50} and a K_i of 78 and 31 nM, respectively [154].

Experimental 0utline

Two different sets of experiments, designated as “A” and “B” were performed. Experiment “A” was designed to validate the efficacy of GSK-3β inhibition in the treatment of radiation necrosis. Two cohorts of mice (n=12 each) received a single 45-Gy dose (50% isodose) of GK radiation. At this dose, the onset of radiation necrosis typically occurs 10-12 weeks post-irradiation. Mouse cohort #1 was an irradiated, DMSO-treated, control group; cohort #2 was treated with SB 415286 (1mg/kg in DMSO) i.p. at 24 h, 12 h and 30 min prior to irradiation.

Experiment "B" was designed to test whether GSK-3β inhibition would also have protective effects in tumor tissue. Orthotopic tumors were generated using DBT glioma cells, as described previously [155]. Post-contrast T1-weighted imaging was performed on post-implantation day (PID) 9 to confirm tumor implantation. Mice were randomly assigned into three cohorts: cohort #1 (n=10) was an untreated control group (no irradiation, no SB 415286); cohort #2 received a total 22.5 Gy dose (50% isodose) of GK radiation targeted to the tumor site over 3 fractions given at PID 10, 12 and 14 (but no SB 415286); cohort #3 received the exact same radiation treatment as cohort #2 but was also treated with SB 415286 (1 mg/kg), at 24 h, 6 h and 30 min prior to the first irradiation fraction and then 30 min prior to the subsequent irradiation fractions. Mice were sacrificed if/when they lost more than 20% bodyweight, suffered obvious behavioral detriments (such as ataxia), or had significantly large tumors as determined by MRI imaging.

MR imaging

Images were collected in an Agilent/Varian (Santa Clara, CA) 4.7-T small-animal MR scanner equipped with a DirectDrive console. The scanner is built around an Oxford Instruments (Oxford, United Kingdom) 33-cm, clear-bore magnet equipped with a 21-cm inner diameter, actively shielded Agilent/Magnex gradient coil assembly (maximum gradient, 28 G/cm; rise time approximately 200 ms) and Oy International Electric Company (IEC; Helsinki, Finland) model A-240 amplifiers (300 V and 300 A).

Data were collected using an actively decoupled coil pair: 1.5-cm outer diameter surface coil (receive) and a 9-cm inner diameter Helmholtz coil (transmit). Mice were anesthetized with isoflurane/O2 (3% [vol/vol]) before the imaging experiments and maintained on isoflurane/O_2 (1% [vol/vol]) throughout the experiments. Mice were restrained in a laboratory-constructed Teflon head holder with ear bars and a tooth bar and were placed on a water pad with circulating warm water to maintain body temperature at approximately 37°C. They were injected intraperitoneally with 0.5 mL Omniscan (gadodiamide; GE Healthcare, Princeton, NJ) contrast agent, diluted 1:10 in sterile saline, 15 min before being placed in the magnet.

Mice in experiment “A” that received 45 Gy of radiation were imaged 10, 13, 16, 19 and 22 weeks post-irradiation. For cohort #1 in experiment “B”, the untreated control group, mice were imaged at PID 10 and then every 3 days until they were sacrificed. For cohorts #2 and #3 of experiment “B”, the treated groups, mice were imaged at PID 10 (before receiving GK radiation), 17, and then every 3 days until they were sacrificed. Multislice, T2-weighted, spin-echo transaxial images were obtained during the 3-15 minutes immediately following gadodiamide administration with the following parameters: time to repetition (TR) = 1.5 s, time to echo (TE) = 0.05 s, field of view (FOV) = 1.5 x 1.5 cm^2, slice thickness = 0.5 mm, 21 slices to cover the whole brain. Multislice, T1-weighted, spin-echo transaxial images were then obtained over 5 minutes with the following parameters: TR = 0.65 s, TE = 0.02 s, FOV = 1.5 x 1.5 cm^2, slice thickness = 0.5 mm, 21 slices to cover the whole brain.

Histology

Immediately after the last MR imaging session, mice were perfused intracardially with 0.1 M Phosphate-buffered saline and formalin. The heads were then dissected and fixed in formalin for 24 hrs. The brains were removed from skulls and embedded in paraffin. The brain was coronally sectioned and 8-micron-thick tissue sections were stained with hematoxylin and eosin (H&E) according to standard protocols. For each brain, a single slice reflecting the same anatomic features was chosen for comparison.

Clonogenic survival assay

Clonogenic survival assays were performed as described previously[156]. Briefly, calculated numbers of cells were plated to enable normalization for plating efficiencies. Cells were allowed to attach for 5 hours and then irradiated with 0, 2, 4, 6 or 8 Gy. After 7-10 days of incubation, plates were fixed with 70% ethanol and stained with 1% methylene blue. Colonies consisting of >50 cells were counted by viewing the plates under a microscope. The survival fractions were calculated as (number of colonies / number of cells plated) / (number of colonies for corresponding control / number of cells plated).

Statistical analysis

For experiment “A”, the weekly changes of necrotic volumes for each group were summarized using means and standard deviations. Because of the relatively large variability in these volumes, a logarithm transformation was performed to better satisfy the assumption of a normal distribution. Two-way ANOVA was used to compare the mean volumes of radiation necrosis among treatment groups, followed by *ad hoc* multiple comparisons for between-group differences at specific time points. For experiment “B”, “Last Observation Carried Forward (LOCF)” analysis was used for visualization of tumor growth. Two-way ANOVA was used to compare the mean tumor volumes among treatment groups, followed *by ad hoc* multiple comparisons for between-group differences at specific time points. All tests were two-sided and a p-value of 0.05 or less was taken to indicate statistical significance. The statistical analysis was performed using SAS 9.3 (SAS Institutes, Cary, NC).

Results

MRI detects radiation necrosis as image hyperintensity in T1-weighted images

Representative T1-weighted spin-echo images of SB 415286-treated and DMSO-treated mice, covering the same anatomic region of the brain and collected at 13, 16, 19, and 22 weeks following a single 45-Gy dose of radiation are shown in Figure 1. Hyperintense areas in these images correspond with regions of RN in the brain. Evident hyperintense regions are clearly seen in DMSO-treated, control mice at 13 weeks post-irradiation and these regions expand significantly in extent by 22 weeks. The images of SB 415286-treated mice (1mg/kg) show minimal hyperintensity, even at 22 weeks post-irradiation.

Necrosis volumes can be measured quantitatively from MR images

The development of RN is associated with hyperintensity in both T2-weighted and contrast-enhanced, T1-weighted images. At each time point, regions of interest were drawn around the entire brain in several contiguous image slices, chosen to include the entire hyperintense region. Each brain was divided along the midline into left (irradiated) and right (non-irradiated) hemispheres. The image intensity for each individual pixel in the left hemisphere was normalized by the average of the 25 pixels (5 x 5 square) including and immediately surrounding its mirror-image pixel in the right hemisphere, and histograms of normalized intensity for the irradiated hemisphere were constructed. We have performed this same analysis previously in a cohort (n=10) of non-irradiated mice and shown that the resulting histogram is symmetric; with 99% of the pixels being distributed in the intensity range 0.6 – 1.4 about a normalized mean of 1.0. Therefore, an intensity threshold of 1.4 was chosen as the cutoff for normal brain tissue. The number of pixels exceeding this threshold measures the necrotic volume at each time point for irradiated mice.

GSK-3β inhibitor slows the progression of radiation necrosis in brain tissue

Figure 2A shows the progression of the volumes of MRI-derived necrotic regions for DMSO-treated (red) and SB 415286-treated (blue) mice (1mg/kg), in which all the mice received a single, 45-Gy dose of radiation. Seven out of 12 mice treated with SB 415286 had smaller necrotic regions at 22 weeks compared with control mice. The neuroprotective effect is clearly evident in the progression of the mean volumes (Figure 2B), in which the treated cohort had a greatly diminished volume of necrosis at weeks 16, 19 and 22 post-irradiation compared to DMSO-treated controls ($p=0.0024$, 0.0003, and 0.0056 for weeks 16, 19 and 22, respectively).

Histology reveals that GSK-3β inhibitor protects against radiation necrosis in irradiated brain tissue

Figure 3 shows 2x (top) and 10x (middle) H&E histologic images and corresponding T1-weighted MR images (bottom) for DMSO-treated, and SB 415286-treated mice (1mg/kg) at 22 weeks following a single, 45 Gy dose of radiation. The irradiated hemispheres of the DMSO-treated mice demonstrated many of the classic histologic features of RN, including fibrinoid vascular necrosis (black arrow), vascular telangiectasia (yellow arrows), hemorrhage (red arrow), and loss of neurons and edema (blue arrows) [4]. In contrast, the irradiated hemisphere of the SB 415286-treated mouse showed only minimal tissue damage. These histologic findings support the MR data shown in Figure 2, demonstrating a significant neuroprotective effect of GSK-3β inhibition.

GSK-3β inhibitor does not affect the therapeutic efficacy of radiation on tumor tissue

Figure 4 shows representative T1-weighted, spin-echo images of non-irradiated, radiation only, and radiation plus SB 415286-treated (1mg/kg) tumor-bearing mice; images cover the same anatomic region of the brain and were obtained on PID 10 and 20. Hyperintense areas in these images correspond with regions of tumor in the brain. Evident hyperintensity is clearly seen in all three mice at PID 10, but only in the non-irradiated mice did the hyperintense region grow significantly in extent between PID 10 and 20. This is seen clearly in the tumor growth curves for the three cohorts (Figure 5). Tumors in non-irradiated mice grew quickly compared to the irradiated mice, while no significant difference was observed between radiation-treated mice with and without pre-treatment with SB 415286 (1mg/kg), demonstrating that SB 415286 does not affect the therapeutic efficacy of radiation.

Survival data are shown in Figure 6A for all cohorts. If SB 415286 fully protected tumor cells from radiation, the survival curves of cohorts 1 and 3 would be the same. Instead, treatment with radiation plus SB 415286 leads to a significant increase in median survival compared with non-irradiated controls ($P=0.0024$), a survival increase that was statistically indistinguishable from radiation treatment alone ($P=0.9974$). This observation demonstrates that administering the GSK-3β inhibitor SB 415286 has no effect on this glioma model’s sensitivity to radiation. We further evaluated the effect of the GSK-3β inhibitor SB 415286 on irradiated DBT cells in a colony formation assay. As shown in Figure 6B, the DBT glioma cells treated with 25 μM SB 415286 showed significantly decreased survival following irradiation. SB 415286 did not protect, but in fact radiosensitized, the DBT cells in culture.

Discussion

SB 415286, a small molecule inhibitor of GSK-3β, provides significant protection from radiation-induced apoptosis in neuronal cells in culture [147, 150]. MRI monitoring of RN, in concert with GK irradiation, offers an attractive strategy for validating the *in vivo* neuroprotective effect of this GSK-3β inhibitor with laboratory animals. We have established a mouse model that consistently reproduces the histology of RN observed in patients. Herein, we demonstrate that exposure to SB 415286 reduces the progression of RN in the mouse. The onset and progression of RN in mouse brain were characterized by measuring the volume of hyperintense regions on contrast-enhanced T1-weighted images. Characterization with T2-weighted images yielded essentially equivalent findings (data not shown). The greatly reduced progression of RN in SB 415286-treated mice measured longitudinally by *in vivo* MR imaging, and corresponding histologic findings, clearly demonstrate the efficacy of this GSK-3β inhibitor. In addition, tumor-bearing mice treated with SB 415286 prior to irradiation show no difference in median survival compared with untreated, irradiated mice, suggesting that SB 415286 did not reduce the therapeutic efficacy of radiation on tumor tissue. These findings are entirely consistent with a colony formation assay of DBT glioma cells in culture.

The neuroprotective effect of SB 415286 is dependent on the radiation dosing scheme. Mice receiving a single, 60-Gy dose of radiation showed no significant difference in the progression of RN between control and treated cohorts was observed (data not shown). The radiation dose-response relationship has been modeled as a sigmoid function [122]. The results of these studies suggest that 45-Gy of radiation may be near the middle of the sigmoid curve for this mouse model of radiation necrosis, where small shifts in the curve due to treatment with SB 415286 can generate a significant protective effect.

Findings of the present study motivate consideration of SB 415286 as a potential neuroprotectant. However, its half-life is shorter than 24 hours. Assuming the inhibitor acts by targeting the acute apoptosis of glial cells and endothelial cells, a process that lasts longer than 24 hours, continuous use of SB 415286 following irradiation might, therefore, increase its therapeutic efficacy. Studies to optimize dosing schemes are a logical next step.

Conclusion

The data in this study demonstrate that (i) SB 415286, a small molecule inhibitor of GSK-3β, confers significant neuroprotection in a mouse model of RN and (ii) SB 415286 does not reduce the therapeutic efficacy of radiation on the mouse DBT glioma model of glioblastoma. Extrapolating to the clinic, should SB 415286 or other GSK-3β inhibitors reduce/prevent the development of necrosis in normal CNS tissue following irradiation, the development of more aggressive/effective radiation paradigms would likely follow.

Acknowledgments

This project has been supported by NIH grants R01 CA155365 (JRG), R01 CA174966 (DEH), and R01 CA140220-01 (DEH), and funding from the Alvin J. Siteman Comprehensive Cancer Center (P30), P30 CA091842, the Barnes-Jewish Hospital Foundation Cancer Frontier Fund, and Elekta Instruments AB (Stockholm, Sweden).

Figures

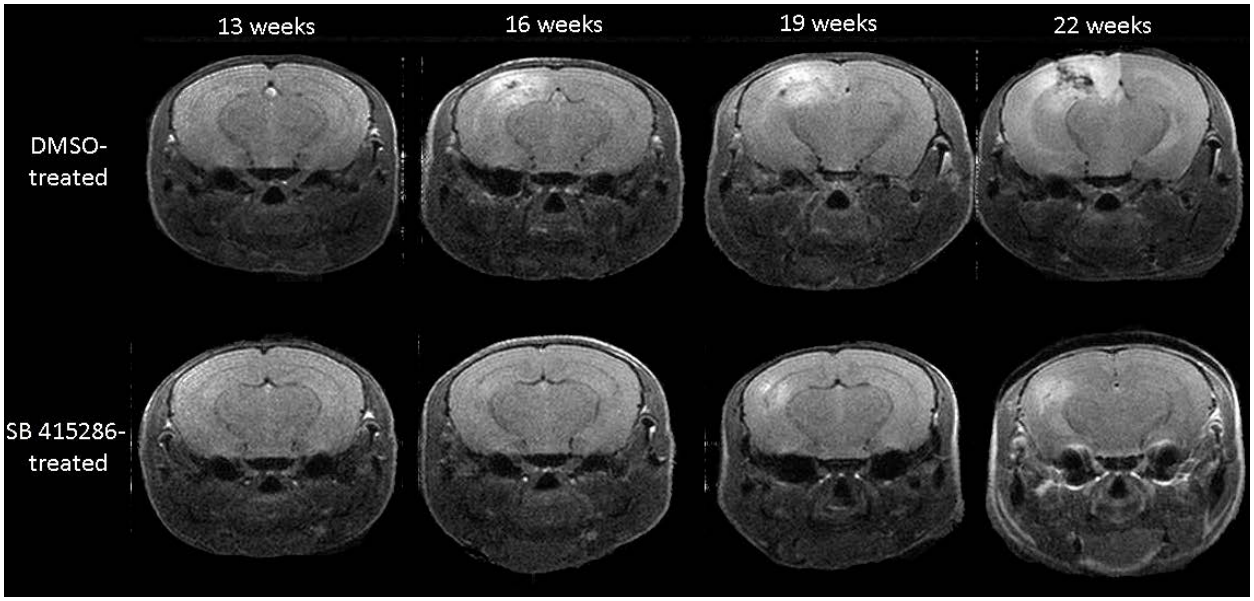

Figure 4.1. Representative transaxial T1-weighted spin-echo images. DMSO-treated (top) and SB 415286- treated (1mg/kg, bottom) mice at (from left to right) 13, 16, 19, and 22 weeks following a single 45-Gy dose, at 50% isodose, of radiation. Slices were chosen to display the same anatomic region of the brain at two time points.

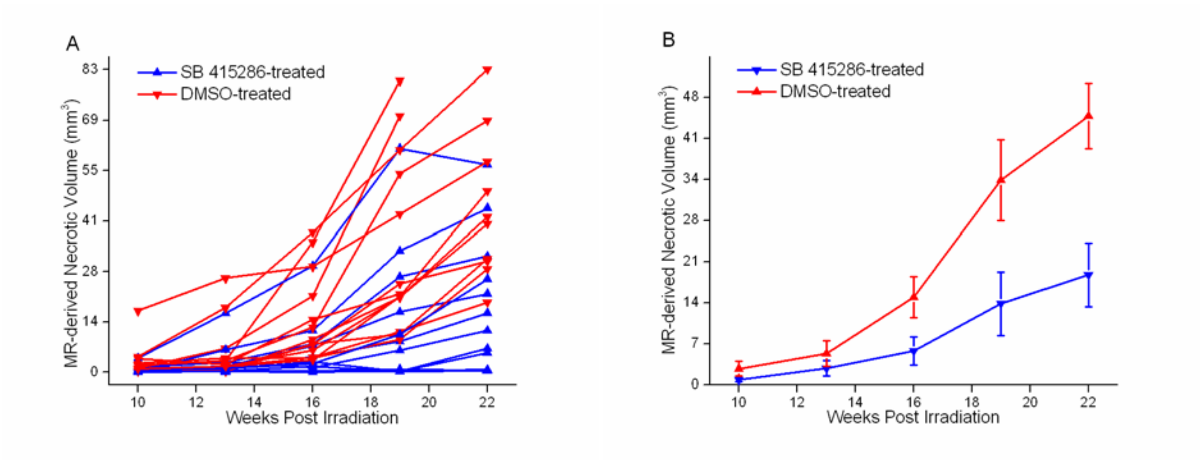

Figure 4.2. Time course plots of MRI-derived necrotic volumes in mice irradiated hemispherically with a single 45-Gy dose of GK radiation. (A) Individual subject data for DMSO-treated and SB 415286 (1mg/kg) treated mice. (B) Summary data mean ± standard error, n=13 and 12 for control and SB 415286-treated mice, respectively.

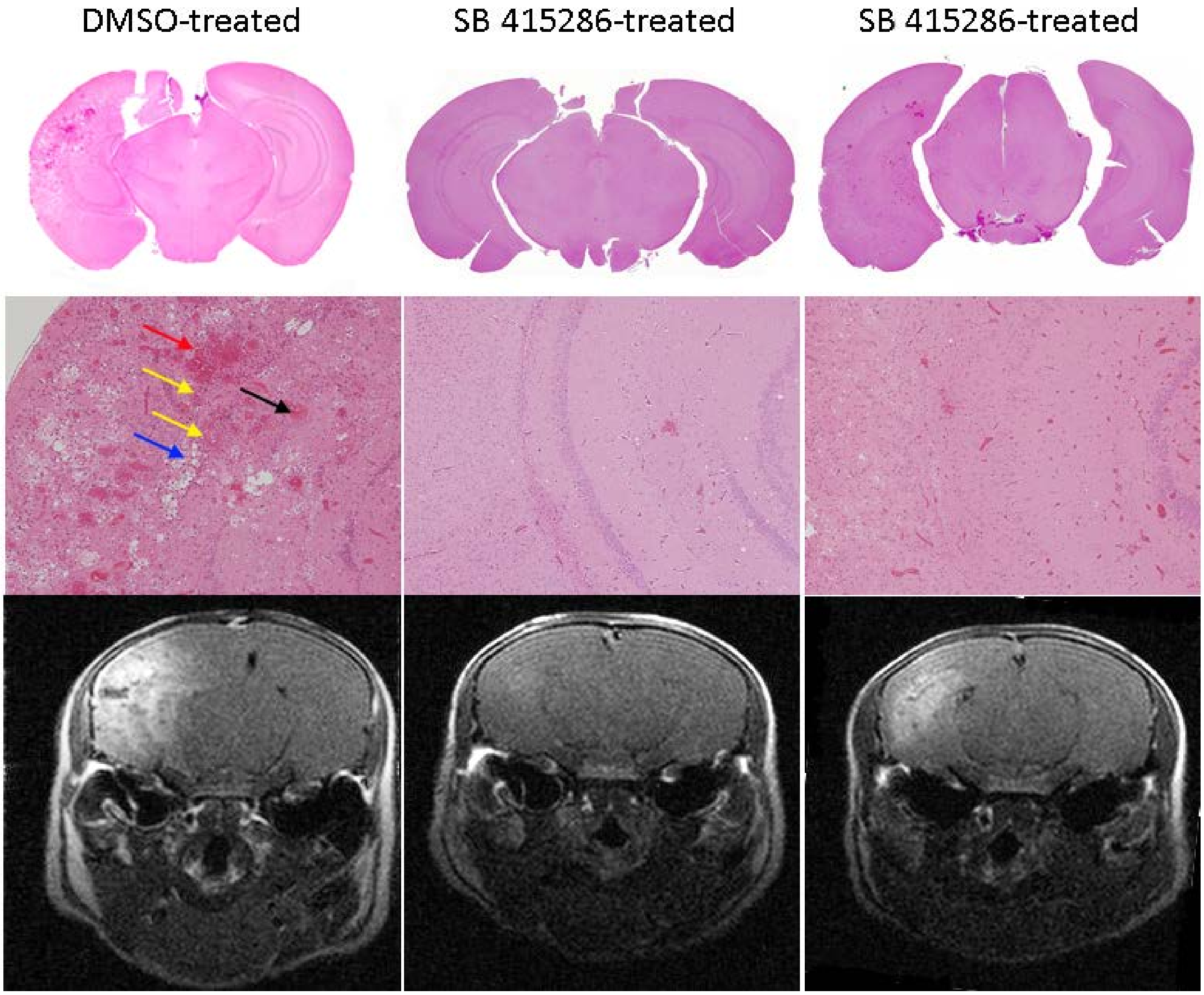

Figure 4.3. H&E-stained sections display characteristic histologic features of RN and demonstrate neuroprotection by SB 415286. Representative 2x (top) and 10x (middle) H&E histology slices chosen near the radiation isocenter, and corresponding contrast-enhanced T1W images (bottom) DMSO-treated and (two different) SB 415286 (1mg/kg) treated mice at 22 weeks following 45-Gy fraction of radiation. The irradiated hemispheres of the control mice show many of the histologic features that are characteristic of RN, including fibrinoid vascular necrosis (black arrow), vascular telangiectasia (yellow arrows), hemorrhage (red arrow), loss of neurons and edema (blue arrows). In addition, the tissue injury observed on the histology slices

is highly correlated with the hyperintense regions on T1-weighted images. These features are largely lacking or are reduced in severity in the SB 415286 -treated mice.

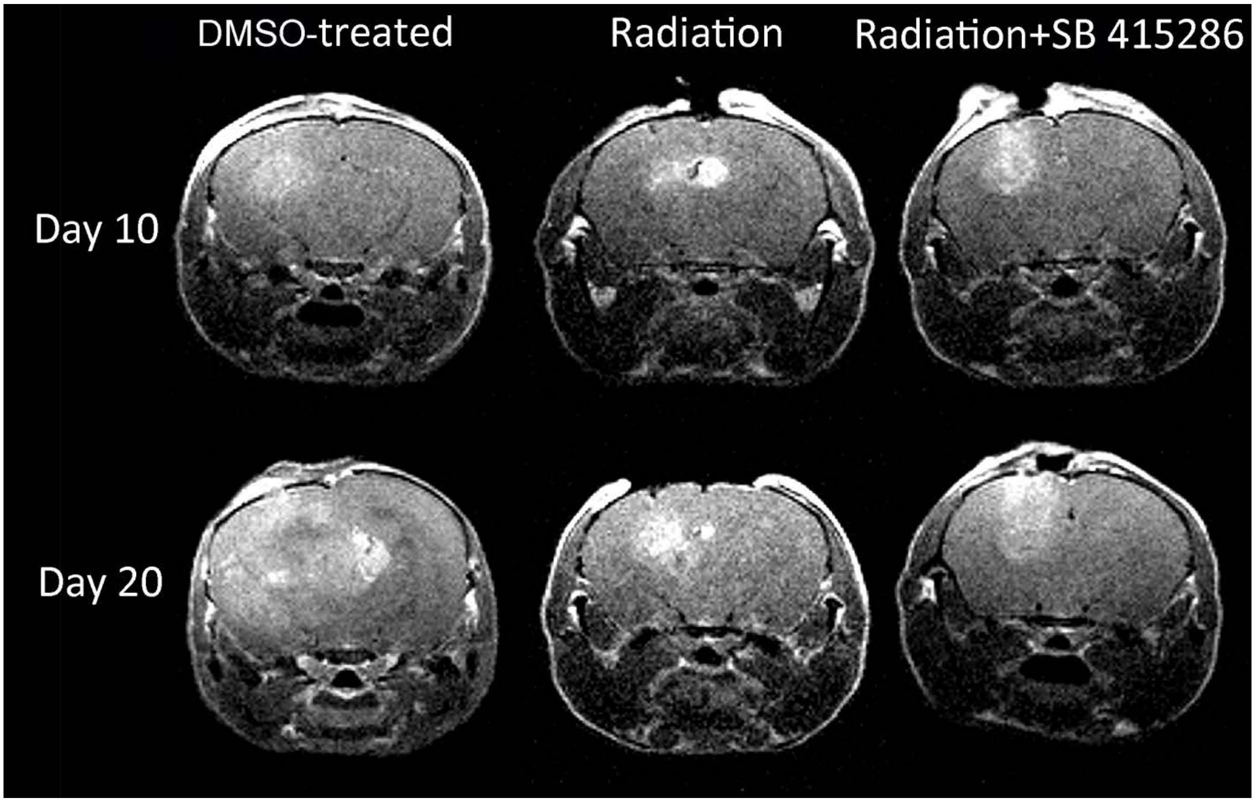

Figure 4.4. Representative transaxial T1-weighted spin-echo images. Untreated, tumor-bearing (left), radiation-treated, tumor-bearing (middle) and combination of radiation with SB 415286 (1mg/kg) treated, tumor bearing (right) mice at 10 and 20 (from top to bottom) days post-implantation with DBT glioma cells. Slices are chosen to display the same anatomic region of the brain at two time points.

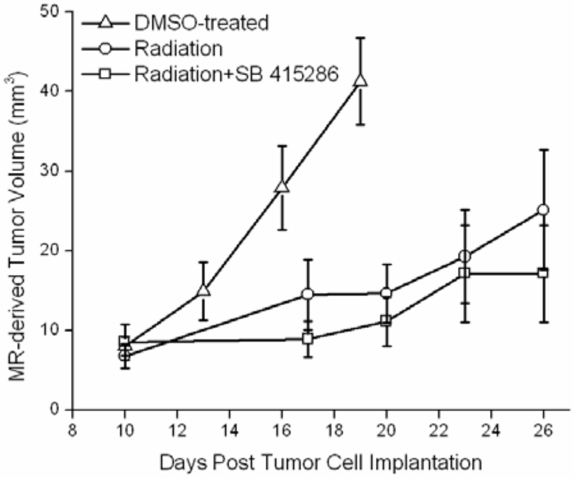

Figure 4.5. Time course of MRI-derived tumor volumes for mice implanted with DBT glioma cells. Mean ± standard error, n = 10 each for untreated, radiation-treated, and combined radiation- and SB 415286-treated mice.

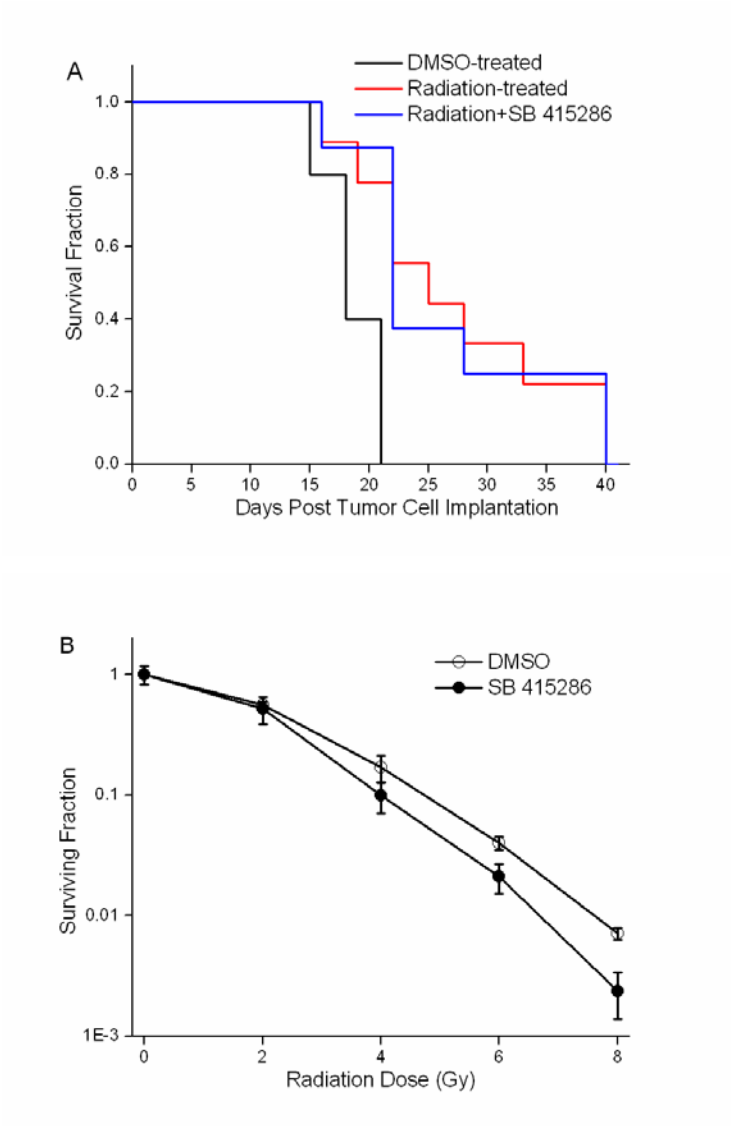

Figure 4.6. A. Survival of tumor bearing mice. Percent surviving fraction is presented for DMSO-treated mice (black line, N=10), radiation-treated mice (red line, N=9), and combined radiation and SB 415286-treated mice (blue line, N=9). Both treatment regimes significantly increased median survival over the untreated group. Survival curves for the two treatment groups were statistically indistinguishable. B. Survival of cultured DBT glioma cells. Cells were treated with DMSO (o) or 25 μM of SB 415286 (•) for 16 h, irradiated with 0, 2, 4, 6 and 8 Gy and

plated for clonogenic survival assay. After 10 days, colonies were fixed, stained with 1% methylene blue, and counted. Shown are the percent surviving fractions for DMSO- or SB 415286-treated DBT cells.

References

1. Giglio P, Gilbert MR. Cerebral radiation necrosis. *Neurologist* 2003;9:180-188.
2. Siu A, Wind JJ, Iorgulescu JB, *et al.* Radiation necrosis following treatment of high grade glioma-a review of the literature and current understanding. *Acta Neurochirurgica* 2012;154:191-201.
3. Brandsma D, Stalpers L, Taal W, *et al.* Clinical features, mechanisms, and management of pseudoprogression in malignant gliomas. *Lancet Oncol* 2008;9:453-461.
4. Kumar AJ, Leeds NE, Fuller GN, *et al.* Malignant gliomas: MR imaging spectrum of radiation therapy- and chemotherapy-induced necrosis of the brain after treatment. *Radiology* 2000;217:377-384.
5. Ruben JD, Dally M, Bailey M, *et al.* Cerebral radiation necrosis: incidence, outcomes, and risk factors with emphasis on radiation parameters and chemotherapy. *Int J Radiat Oncol Biol Phys* 2006;65:499-508.
6. Stupp R, Hegi ME, Mason WP, *et al.* Effects of radiotherapy with concomitant and adjuvant temozolomide versus radiotherapy alone on survival in glioblastoma in a randomised phase III study: 5-year analysis of the EORTC-NCIC trial. *Lancet Oncology* 2009;10:459-466.
7. Stupp R, Mason WP, van den Beuf MJ. Radiotherapy plus concomitant and adjuvant temozolomide for newly diagnosed glioblastoma (vol 352, pg 19, 2005). *Annals of Oncology* 2005;16:949-949.
8. Torcuator R, Mohan YS, Lee I, *et al.* Initial experience with bevacizumab treatment for biopsy-confirmed cerebral radiation necrosis. *Neuro-Oncology* 2007;9:580-581.
9. Shaw PJ, Bates D. Conservative Treatment of Delayed Cerebral Radiation Necrosis. *Journal of Neurology Neurosurgery and Psychiatry* 1984;47:1338-1341.
10. Levin VA, Bidaut L, Hou P, *et al.* Randomized Double-Blind Placebo-Controlled Trial of Bevacizumab Therapy for Radiation Necrosis of the Central Nervous System. *International Journal of Radiation Oncology Biology Physics* 2011;79:1487-1495.
11. Kohshi K, Imada H, Nomoto S, *et al.* Successful treatment of radiation-induced brain necrosis by hyperbaric oxygen therapy. *Journal of the Neurological Sciences* 2003;209:115-117.
12. Jeyaretna DS, Curry WT, Batchelor TT, *et al.* Exacerbation of Cerebral Radiation Necrosis by Bevacizumab. *Journal of Clinical Oncology* 2011;29:E159-E162.
13. But QC, Lieber M, Withers HR, *et al.* The efficacy of hyperbaric oxygen therapy in the treatment of radiation-induced late side effects. *International Journal of Radiation Oncology Biology Physics* 2004;60:871-878.
14. Rahmathulla G, Marko NF, Weil RJ. Cerebral radiation necrosis: A review of the pathobiology, diagnosis and management considerations. *Journal of Clinical Neuroscience* 2013;20:485-502.
15. Shi L, Linville MC, Iversen E, *et al.* Maintenance of white matter integrity in a rat model of radiation-induced cognitive impairment. *Journal of the Neurological Sciences* 2009;285:178-184.
16. Zhou H, Liu Z, Liu J, *et al.* Fractionated Radiation-Induced Acute Encephalopathy in a Young Rat Model: Cognitive Dysfunction and Histologic Findings. *American Journal of Neuroradiology* 2011;32:1795-1800.

17. Wilson CM, Gaber MW, Sabek OM, *et al.* Radiation-Induced Astrogliosis and Blood-Brain Barrier Damage Can Be Abrogated Using Anti-Tnf Treatment. *International Journal of Radiation Oncology Biology Physics* 2009;74:934-941.
18. Wong CS, Van der Kogel AJ. Mechanisms of radiation injury to the central nervous system: implications for neuroprotection. *Molecular Interventions* 2004;4:273-284.
19. Embi N, Rylatt DB, Cohen P. Glycogen synthase kinase-3 from rabbit skeletal muscle. Separation from cyclic-AMP-dependent protein kinase and phosphorylase kinase. *Eur J Biochem* 1980;107:519-527.
20. Leroy K, Brion JP. Developmental expression and localization of glycogen synthase kinase-3beta in rat brain. *J Chem Neuroanat* 1999;16:279-293.
21. Watcharasit P, Bijur GN, Zmijewski JW, *et al.* Direct, activating interaction between glycogen synthase kinase-3beta and p53 after DNA damage. *Proc Natl Acad Sci U S A* 2002;99:7951-7955.
22. Loberg RD, Vesely E, Brosius FC, 3rd. Enhanced glycogen synthase kinase-3beta activity mediates hypoxia-induced apoptosis of vascular smooth muscle cells and is prevented by glucose transport and metabolism. *J Biol Chem* 2002;277:41667-41673.
23. Song L, De Sarno P, Jope RS. Central role of glycogen synthase kinase-3beta in endoplasmic reticulum stress-induced caspase-3 activation. *J Biol Chem* 2002;277:44701-44708.
24. Thotala DK, Hallahan DE, Yazlovitskaya EM. Inhibition of glycogen synthase kinase 3 beta attenuates neurocognitive dysfunction resulting from cranial irradiation. *Cancer Res* 2008;68:5859-5868.
25. Cross DAE, Culbert AA, Chalmers KA, *et al.* Selective small-molecule inhibitors of glycogen synthase kinase-3 activity protect primary neurones from death. Vol 77; 2001. pp. 94-102.
26. Yazlovitskaya EM, Edwards E, Thotala D, *et al.* Lithium treatment prevents neurocognitive deficit resulting from cranial irradiation. *Cancer Res* 2006;66:11179-11186.
27. Thotala DK, Geng L, Dickey AK, *et al.* A New Class of Molecular Targeted Radioprotectors: Gsk-3 Beta Inhibitors. *International Journal of Radiation Oncology Biology Physics* 2010;76:557-565.
28. Medina M, Avila J. Glycogen synthase kinase-3 (GSK-3) inhibitors for the treatment of Alzheimer's disease. *Curr Pharm Des* 2010;16:2790-2798.
29. Klamer G, Song E, Ko KH, *et al.* Using Small Molecule GSK3 beta Inhibitors to Treat Inflammation. *Current Medicinal Chemistry* 2010;17:2873-2881.
30. Phukan S, Babu VS, Kannoji A, *et al.* GSK3 beta: role in therapeutic landscape and development of modulators. *British Journal of Pharmacology* 2010;160:1-19.
31. Jost SC, Hope A, Kiehl E, *et al.* A Novel Murine Model for Localized Radiation Necrosis and Its Characterization Using Advanced Magnetic Resonance Imaging. *International Journal of Radiation Oncology Biology Physics* 2009;75:527-533.
32. Coghlan MP, Culbert AA, Cross DA, *et al.* Selective small molecule inhibitors of glycogen synthase kinase-3 modulate glycogen metabolism and gene transcription. *Chem Biol* 2000;7:793-803.
33. Jost SC, Wanebo JE, Song SK, *et al.* In vivo imaging in a murine model of glioblastoma. *Neurosurgery* 2007;60:360-370; discussion 370-361.

34. Franken NA, Rodermond HM, Stap J, *et al.* Clonogenic assay of cells in vitro. *Nat Protoc* 2006;1:2315-2319.
35. Perry A, Schmidt RE. Cancer therapy-associated CNS neuropathology: an update and review of the literature. *Acta Neuropathologica* 2006;111:197-212.
36. Schollnberger H, Mitchel RE, Azzam EI, *et al.* Explanation of protective effects of low doses of gamma-radiation with a mechanistic radiobiological model. *Int J Radiat Biol* 2002;78:1159-1173.

Chapter 5 Characterizing Radiation Necrosis using qBOLD

5.1 Introduction

Several factors, including spin-spin interactions, imperfect static magnetic field, and susceptibility inhomogeneities due to air-tissue boundary, contribute to FID signal decay. The contribution from spin-spin interactions, a random effect, can be easily separated from contributions from other time-independent factor. In 1990, paramagnetic deoxyhemoglobin in blood vessel was discovered as an important fixed factor resulting in observable FID signal decay, also known as blood oxygenation level-dependent (BOLD) contrast [157]. Hemoglobin (Hb or Hgb) is the iron-containing oxygen-transport metalloprotein in the red blood cells. It carries oxygen (oxyhemoglobin) from the respiratory organs to the rest of the body where it releases the oxygen (deoxyhemoglobin) used to burn nutrients to provide energy to power the functions of the organism, and collects the resultant carbon dioxide to bring it back to the respiratory organs. Oxyhemoglobin and water in the soft tissue are slightly diamagnetic with an absolute susceptibility of about -9 ppm, while deoxyhemoglobin is paramagnetic with an absolute susceptibility of about 0.15 ppm. These magnetic susceptibility inhomogenities distort the local magnetic field and cause the FID signal decay. The relative length scale of the inhomogeneity induced by blood vessel is a distance smaller than the imaging voxel dimensions but much larger than the atomic and molecular scales. In contrast, the scale of the macroscopic magnetic field inhomogeneities, arising from magnet imperfections, body-air interfaces, and large sinuses inside the body, describes distances larger than the imaging voxel dimensions.

BOLD contrast directly links to the concentration of deoxyhemoglobin, which depends primarily on the oxygen extraction fraction (OEF) and deoxygenated cerebral blood volume (dCBV). This allows BOLD contrast to be useful in understanding brain function as well as the physiology of various tumors [158-162]. Most BOLD studies have focused on the temporal changes in the MR signal during changes in brain activity, also known as functional MRI (fMRI). Absolute quantitation of the BOLD signal and its constitutive components -- dCBV and OEF -- is difficult. Currently, there is no clinically accepted MRI-based method for measuring OEF *in vivo*. The only clinically accepted OEF measurement relies on PET techniques [92]. However, the PET-based methods are limited in human study and clinical practice due to their low spatial resolution and the requirement of radionuclides.

Recently, a quantitative BOLD method, based on an MR signal model in the presence of blood vessel network, has been developed in our laboratory [163]. It has been validated on phantoms [93, 164] and applied to the normal human brain in the baseline state [94]. The resulting OEF map is homogeneous across the entire brain with a mean of about 40%, and the dCBV map indicates that gray matter has ~3 times higher dCBV than white matter [165]. These results are supported by other reports, providing important validation of this approach.

Remarkable changes in cerebral blood flow and oxygen consumption are suggested in the region of radiation necrosis [42]. Consequently, qBOLD could be a promising biomarker for radiation necrosis and provide additional function information to differentiate necrosis from recurrent tumor. The purpose of this study is to evaluate the feasibility of this approach in characterizing radiation necrosis in mouse brain.

5.2 Methodology

5.2.1 qBOLD theory

In qBOLD theory, the blood vessel network is modeled as a collection of uniformly distributed and randomly oriented cylinders of infinite length. The magnetic susceptibility of each cylinder is determined by OEF and dCBV. The extravascular FID signal in the presence of magnetic field inhomogeneities [166] induced by the blood vessel network is described by equation:

$$S(t) = S_0 \cdot F(t) \cdot \exp\left[- dCBV \cdot f(t/t_c) - R_2 t\right],$$

where zero time t corresponds to the position of RF excitation pluse; S_0 is the proton density; F(t) represents the effect of macroscopic magnetic field inhomogeneities due to an imperfect magnet and air-tissue boundary; R_2 represents the T_2 relaxation rate constant, and the characteristic dephasing time, t_c, is defined as:

$$t_c^{-1} = \gamma \cdot \frac{4\pi}{3} \cdot \chi \cdot B_0$$

$$\chi = \Delta\chi_0 \cdot H_{ct}[1 - Y_a \cdot (1 - OEF)],$$

where B_0 is the external magnetic field strength; γ is gyromagnetic ratio; χ represents the susceptibility difference between deoxygenated blood and surrounding soft tissue; Y_a is the blood oxygenation level of arterial blood, which is approximately 1 under normal condition; Hct is the blood hematocrit measured independently from the sample blood (e.g., ~40% for human); $\Delta\chi_0$= 0.264 ppm, which is the susceptibility difference between completely deoxygenated and completely oxygenated blood.

For uniformly distributed and randomly oriented blood vessels, f(t) is given by:

$$f(t/t_c) = \int_0^1 du \frac{(2+u)\sqrt{1-u}}{3u^2}[1 - J_0(\frac{3u}{2} \cdot \frac{t}{t_c})]$$

Where J_0 is a Bessel function. In the short-time and long-time regimes, the function can be simplified into two functions that depend quadratically or linearly on time, respectively:

$$f(t/t_c) = \begin{cases} 0.3 \cdot (t/t_c)^2, |t|/t_c << 1 \\ |t|/t_c - 1, |t|/t_c >> 1 \end{cases}$$

Correspondingly, the signal can be written as:

$$S(t) = \begin{cases} S_0 \cdot F(t) \cdot \exp\left[-0.3 \cdot dCBV \cdot (t/t_c)^2 - R_2 t\right], t/t_c << 1 \\ S_0 \cdot F(t) \cdot \exp\left[-dCBV \cdot (|t|/t_c - 1) - R_2 t\right], t/t_c >> 1 \end{cases}$$

Figure 5.1 shows the time course of the normalized signal $S(t)/S_0$ in the extreme case where F(t)=1, indicating an ideal homogeneous magnetic field. When t/t_c is large, the curve is linear with a slope proportional to the product of dCBV and OEF. If we extend the linear part, the extrapolated point at $t/t_c=0$ is dCBV. However, in real experiments, the function F(t) also decays non-linearly and cannot be ignored. It is the major complication in the calculation of OEF and dCBV.

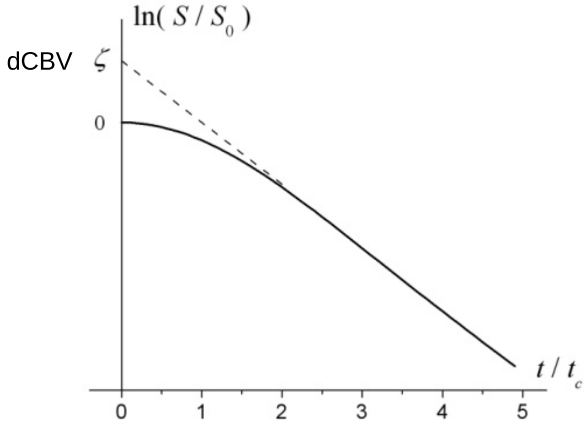

Figure 5.1. The signal, Eq. (5.6), as a function of t/t_c (logarithmic scale).

5.2.2 MRI pulse sequence

Since the accurate measurement of the initial non-linear part in the curve is the key to decouple OEF and dCBV, it was proposed to use the Gradient Echo Sampling of Spin Echo (GESSE) sequence where MR signal is sampled around a spin echo [166]. Compared with the gradient echo sampling starting from the center of the spin echo, this sampling was demonstrated to increase the accuracy of the estimate of the initial non-linear part, and result in a more accurate estimate of OEF and dCBV [166].

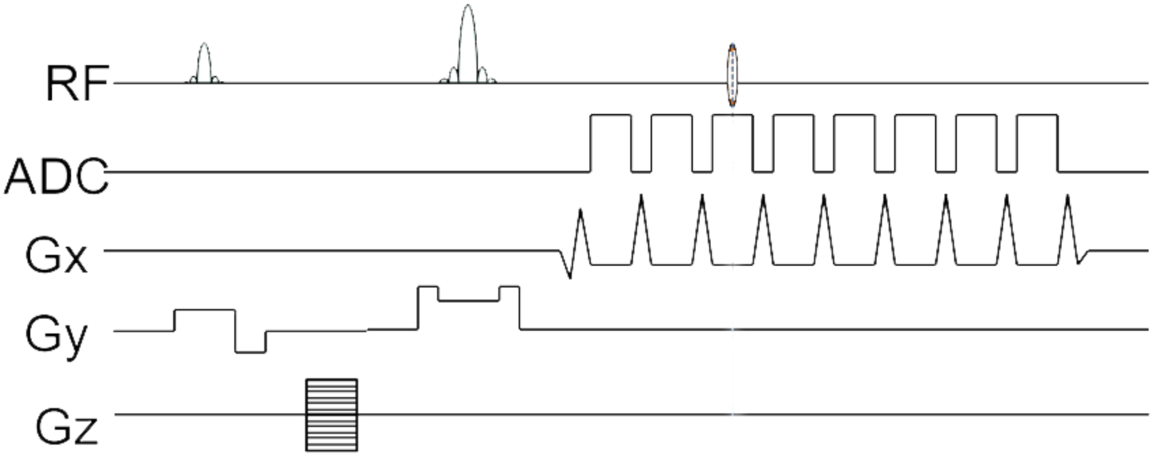

Figure 5.2. Schematic diagram of the GESSE sequence.

5.2.3 Auto shimming

As mentioned, an extremely homogeneous magnetic field is required to minimize the effect of F(t) term and extract OEF and dCBV from the signal decay. Active shimming is commonly used prior to any operation of the magnet to adjust the homogeneity of the scanner's magnetic field using shim coils with adjustable current. Our Agilent/Varian scanners allow both manual and automatic shimming across the entire space or within a user-defined voxel. Compared with manual shimming, automatic shimming is more efficient and accurate. The principle of automatic shimming is based on the accurate measurement of a field-map, which spatially maps the actual magnetic field in each imaging voxel. It is well known that any magnetic field can be described as a summation of gradients in different directions. Accordingly, the scanner can adjust the current flowing through the shim coils to compensate the inhomogeneities (gradients) in the shimming volume.

5.2.4 Numerical simulation

The trade-off between temporal/spatial resolutions and signal-noise-ratio (SNR) is an important factor for the accurate estimate of OEF and dCBV. In order to identify the minimum SNR, a numerical simulation was performed. Assuming the magnetic field is perfectly homogeneous (F(t) = 1), the signal was calculated by the equation shown below:

$$S_{sim}(t) = \exp\left[-dCBV \cdot f(t/t_c) - R_2 t\right] + noise_{gaussian}(\mu, \sigma)$$

The signal is then fitted by Eq. (5.7) but without the noise term, to generate dCBV, OEF and R_2. SNR is defined by S(t=0) divided by the standard deviation of the Gaussian noise, and is sampled from 20 to 520 in steps of 10. The differences between preset and fitted values of dCBV, OEF and R_2 were compared at different SNR levels.

5.2.5 Data processing

Hanning filter

It is well known that the Fourier Transform based MR images suffer from intervoxel signal leakage due to Gibbs ringing artifacts. The Gibbs phenomenon arises from the facts that 1) Fourier sums overshoot at a jump discontinuity, such as the edge of a single voxel, and 2) this overshoot does not decay as the frequency increases. Various methods have been reported to ameliorate this phenomenon, including the smoother method of Fourier series summation, sigma-approximation, and wavelet transform with Haar basis functions [167].

Here, we applied a Hanning filter, which corresponds to the following transformation of the signal (in 2D case), to reduce Gibbs ringing artifacts and improve SNR:

$$S_{i,j}^{Hanning} = \frac{1}{4}S_{i,j} + \frac{1}{8}(S_{i-1,j} + S_{i+1,j} + S_{i,j-1} + S_{i,j+1}) + \frac{1}{16}(S_{i-1,j+1} + S_{i+1,j+1} + S_{i-1,j-1} + S_{i+1,j-1}) \quad (5.11)$$

where S(i,j) represents the raw signal in the image domain at position (i,j).

Correction for macroscopic magnetic field inhomogeneities

As discussed, the decoupling of OEF and dCBV requires an accurate determination of the effect of macroscopic magnetic field inhomogeneities. In 2D MRI, the through-plane macroscopic magnetic field inhomogeneities result from a constant magnetic field gradient across the imaging voxel and their influence on the signal can be calculated using the sinc-function approach [166, 168]. However the contribution of the in-plane magnetic field inhomogeneities is complicated by the intervoxel signal leakage resulting from Gibbs ringing artifacts [169]. Natural linewidth chemical shift imaging (NL-CSI) has been proposed to eliminate the contribution from macroscopic magnetic field inhomogeneities mathematically, however, additional data are required to generate a high resolution field map.

Recently, a novel voxel spread function (VSF) method [170] has been developed that utilizes both magnitude and phase of MR images, allowing quantitative calculation of magnetic field inhomogeneity effects. The following is a brief description of the VSF algorithm.

In the presence of an inhomogeneous magnetic field b(r), the signals in k-space and image domain for a 3D qBOLD experiment can be written as follows:

$$
\begin{aligned}
&\tilde{S}(\vec{k};TE) = \int d\vec{r} \cdot \rho(\vec{r};TE)\exp[-2\pi i\vec{k}\vec{r} + i\gamma b(\vec{r})(TE+t) + i\varphi_0(\vec{r})] \\
&2\pi k_x = \gamma G_x t_x ; 2\pi k_y = \gamma G_y t_y ; 2\pi k_z = \gamma G_z t \\
&S_n(TE) = \frac{1}{N} \cdot \sum_k \tilde{S}(\vec{k};TE) \cdot \exp(2\pi i\vec{k}\vec{r}_n) \qquad\qquad , \\
&k_j = (-\frac{1}{2} + \frac{1}{N_j}, -\frac{1}{2} + \frac{2}{N_j}, -\frac{1}{2} + \frac{3}{N_j}, ..., \frac{1}{2}) / a_j
\end{aligned}
$$

where TE is the gradient-echo time, t is the time during GE acquisition, ρ is the ideal signal at TE without any magnetic field inhomogeneities, Gx, Gy and Gz are phase encoding (x and y) and read-out (z) gradients, and φ_0 is the phase shift at TE = 0.

In practice, assuming that i) the total signal is the summation of signals from n imaging voxels; ii) the magnetic field inhomogeneities within each voxel are described as resulting from a small background gradient; and iii) the proton density is homogeneous across each voxel, the b(r) and φ_0 can be further expressed as:

$$
\begin{aligned}
&b_n(\vec{r}) = b_n + g_{nx}x + g_{ny}y + g_{nz}z \\
&\varphi_0(\vec{r}) = \varphi_{0n} + \varphi_{nx}x + \varphi_{ny}y + \varphi_{nz}z
\end{aligned}
$$

Thus, the k-space signal can be written as:

$$
\begin{aligned}
&\tilde{S}(\vec{k};TE) = \sum_n \rho_n(TE) \cdot \exp(-2\pi i\vec{k}\vec{r}_n) \cdot \exp(i\gamma b_n \cdot TE + i\varphi_{0n}) \\
&\cdot \sin c[(k_x - k_{nx})a_x \cdot \sin c[(k_y - k_{ny})a_y \cdot \sin c[(k_z - k_{nz})a_z] \\
&2\pi k_{nj} = \gamma g_{nj} TE + \varphi_{nj} \\
&j = x, y, z
\end{aligned}
$$

By defining a voxel spread function (VSF), the signal in image domain can be simplified as:

$$S_n(TE) = \sum_m VSF_x \cdot VSF_y \cdot VSF_z \cdot \exp(i\varphi_{0m} + i\gamma b_m TE) \cdot \rho_m(TE)$$
$$VSF_j = \sum_q \sin c(q - (\gamma g_{mj} TE + \varphi_{mj}) a_j / 2\pi) \exp(2\pi i q(n - mj))$$
$$q = k_x a_x, k_y a_y, k_z a_z$$

By calculating $b_m, \varphi_{0m}, g_{mj}, \varphi_{mj}$ using the phase image, ρ_m can be mathematically solved. However, this approach involves inversion of large matrices and it is time-consuming. An approximation can be achieved by assuming that the signals from neighboring voxels behave similarly in the absence of magnetic field inhomogeneities, which can be expressed as:

$$\rho_m(TE) \cdot |S_n(0)| = \rho_n(TE) \cdot |S_m(0)|$$

In this case, the expression of $S_n(TE)$ reduces to:

$$S_n(TE) = \rho_n(TE) \cdot F_n(TE)$$
$$F_n(TE) = \frac{1}{|S_n(0)|} \sum_m VSF_x \cdot VSF_y \cdot VSF_z \cdot \exp(i\varphi_{0m} + i\gamma b_m TE) \cdot |S_m(0)|$$

Therefore, the “ideal” signal in the absence of macroscopic magnetic field inhomogeneities can be obtained simply by dividing the signal by the F-function calculated from the phase image.

5.3 Results

Numerical simulation optimizes the qBOLD imaging parameters

As shown in the Figure 5.2, the accurate estimates of OEF and dCBV require SNR higher than 400. In contrast, the fitted values of R2 and the product of OEF and dCBV are close to their true values if SNR is higher than 50.

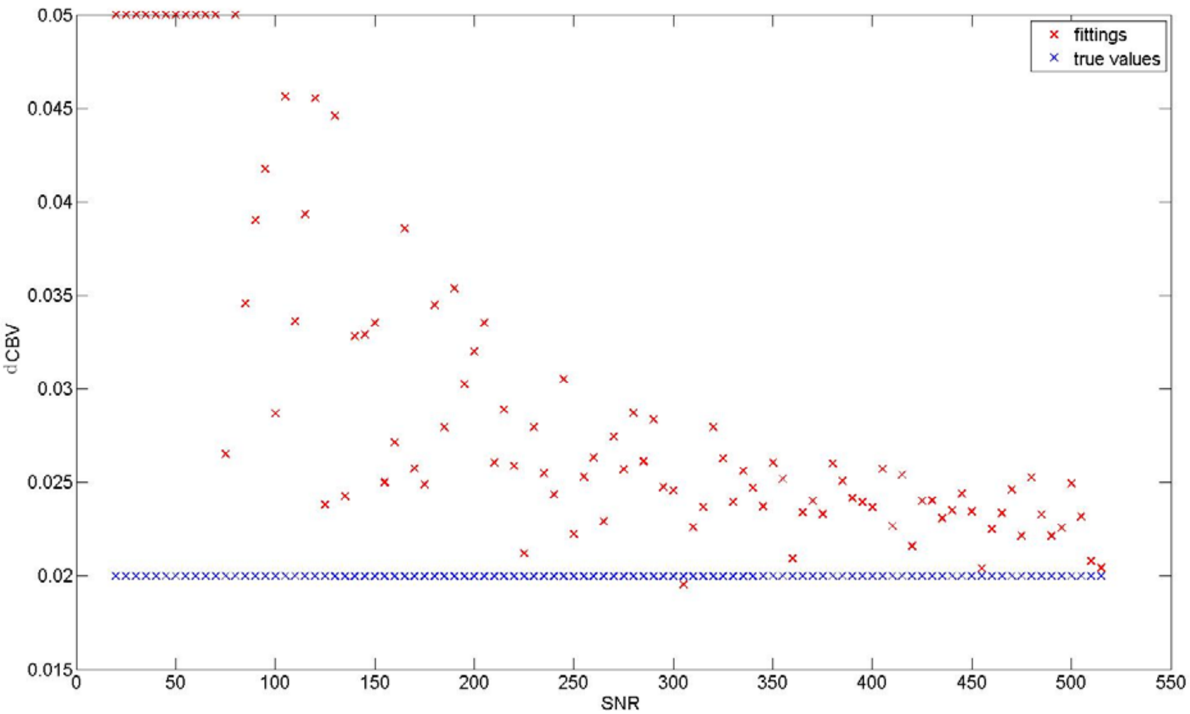
dCBV
0.05
0.045
0.04
0.035
0.03
0.025
0.02
0.015
0
50
100
150
200
250
300
350
400
450
500
550
SNR
fittings
true values

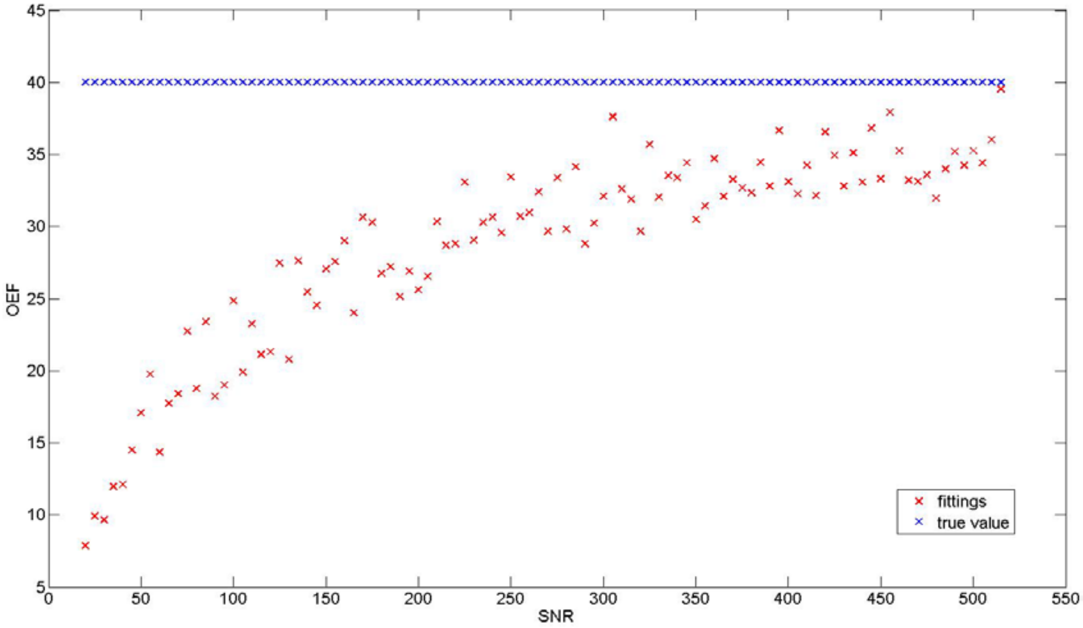
OEF
45
40
35
30
25
20
15
10
5
0
50
100
150
200
250
300
350
400
450
500
550
SNR
fittings
true value

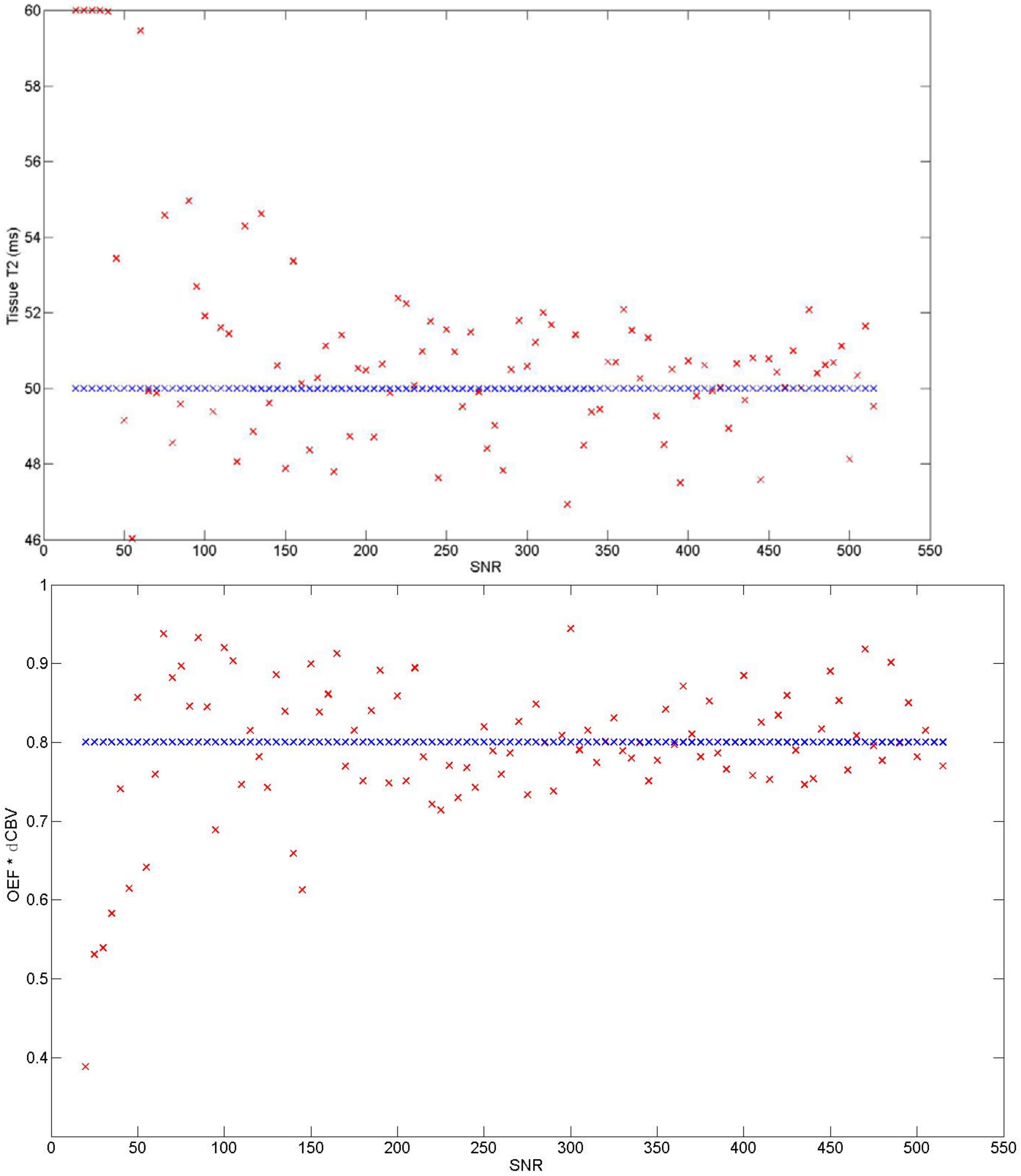

Figure 5.3. Numerical simulation. (from top to bottom) the fitted dCBV vs SNR; the fitted OEF vs SNR; the fitted T2* vs SNR; the product of dCBV and OEF vs SNR.

In order to obtain qBOLD images with a high SNR (>400), the imaging parameters are chosen as follows:

6 slices with slice thickness = 1 mm, TE of spin echo = 43 ms, TR = 2000 ms, 30 echoes, delta TE = 1.64 ms, spin echo is at the 10th echo, FOV = 15 x 15 mm^2, data matrix = 32 x 32, two blocks with each block has 16 averages, and the total scan time = 32 mins.

After applying a Hanning filter, the resulting images are shown in Figure 5.3, and the corresponding SNRs for 30 echoes of the 3rd slice with or without the Hanning filter are shown in Figure 5.4. The 10th echo image with and without applying the Hanning filter has SNRs of approximately 400 and 1100, respectively, which matches the SNR requirement suggested by the previous numerical simulation.

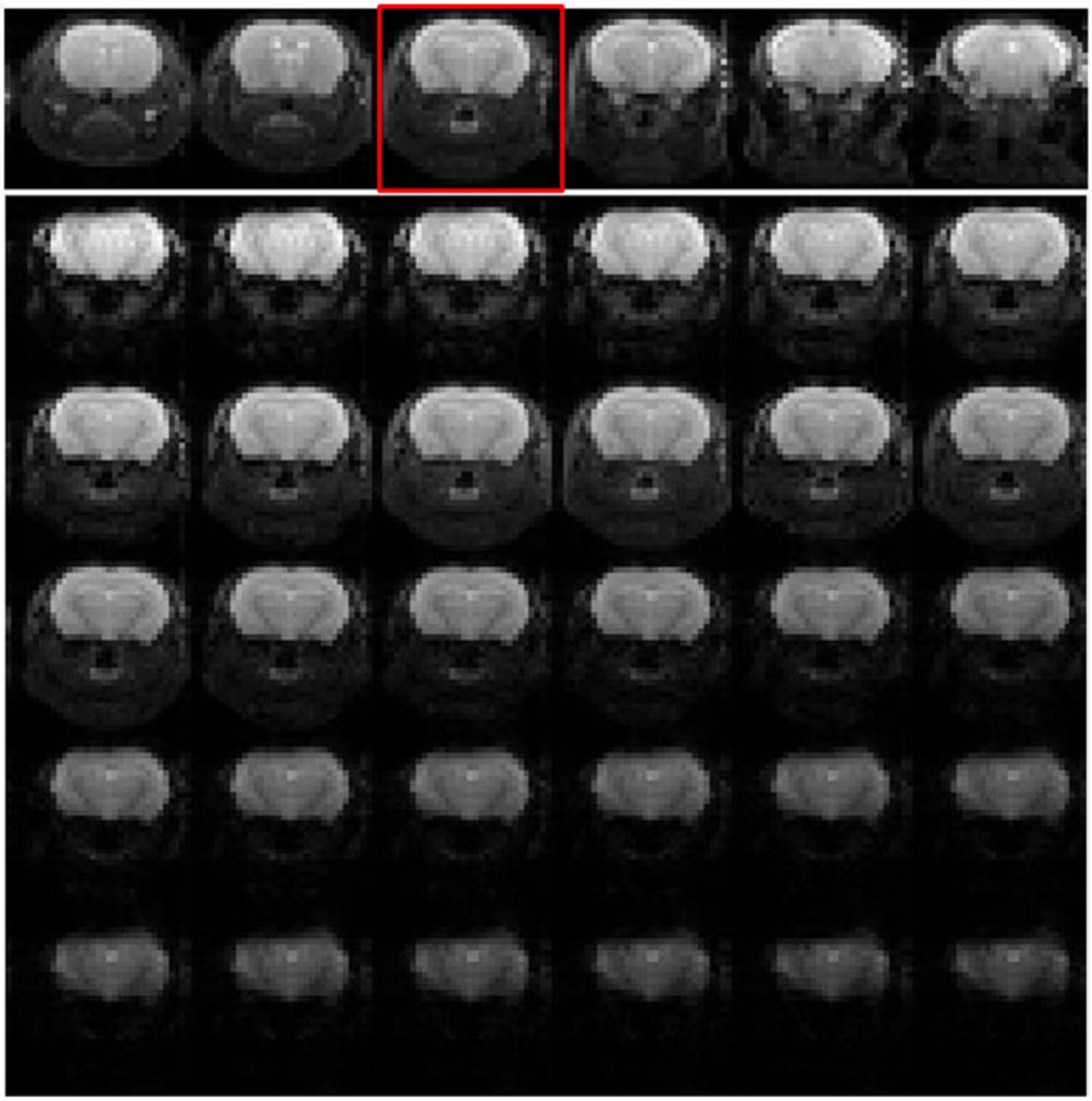

Figure 5.4. qBOLD images after applying the Hanning filter. The first row shows the spin echo images for six contiguous slices. The bottom 5 x 6 panel represents 30 echoes for the third slice (in red outline).

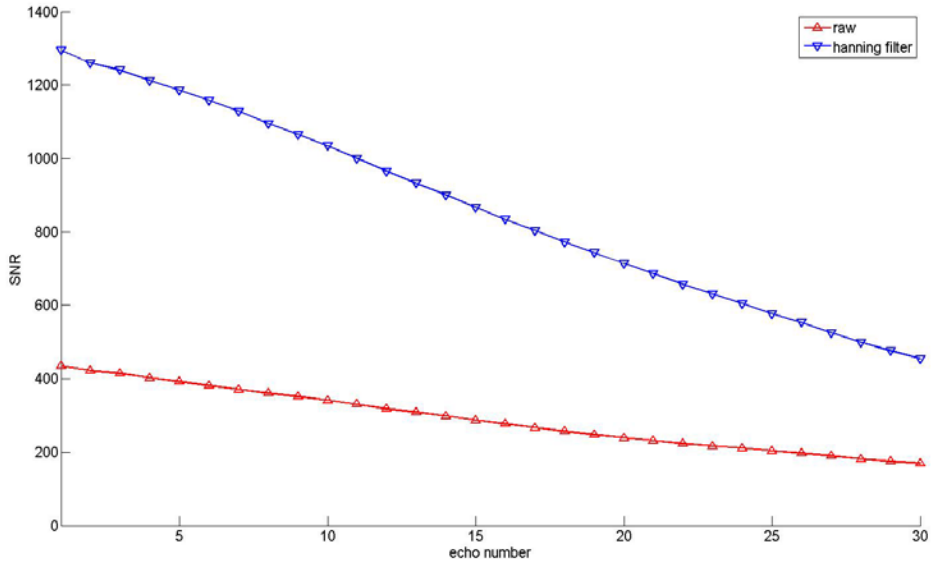

Figure 5.5. SNR for a single mouse brain slice vs echo number with and without applying the Hanning filter.

Auto shimming reduces the macroscopic magnetic field inhomogeneities

The advantage of automatic shimming over manual shimming is shown in a phantom study with a tube of water. In this dissertation, all the MR images were collected with a larger uniform-excitation transmit coil and a small, high sensitivity surface receive coil. One drawback of the use of surface coil is that the signal intensity drops sharply with increasing distance between coil and imaging voxel. This sensitivity profile is clearly evident in the axial gradient-echo image of a tube of water (Figure 5.5). In general, manual shimming improves the field homogeneity by slowing the FID signal decay. Accordingly, manual shimming favors the region of higher sensitivity that contributes more to the overall FID signal. In contrast, automatic shimming is based on the calculation of a field map, which is independent of the sensitivity of the receiving coil. The resulting fieldmaps after shimming show clear differences between the two shimming methods (Figure 5.6).

The following qBOLD experiments in mouse/rat brains were all performed after automatic shimming. The Full Width at the Half-Height (FWHH) of the spectrum for a tissue volume of 6 x 12 x 9 mm^3 in mouse brain is approximately 20 Hz (about 0.1 ppm in 4.7 Tesla) after automatic shimming, which usually takes about 5 – 6 minutes. Since the field change induced by blood vessel network is on the order of 10 Hz, the remaining macroscopic magnetic field inhomogeneities after automatic shimming cannot be ignored in the qBOLD data processing. The fieldmaps (Figure 5.7) show clearly that only a small region in the center of brain exhibits homogeneous field, while the top and bottom of the brain suffer from severe magnetic field inhomogeneities. A shimming experiment performed in an *ex vivo* mouse brain immersed in water confirms that the troublesome macroscopic magnetic field inhomogeneities arise from the tissue-air boundary and primarily, the air-filled ear cavities. The FWHH of the spectrum for the same volume used for the *in vivo* experiment is 7 Hz, and the field maps (Figure 5.7) show large regions of homogeneous magnetic field, indicating a significant improvement of magnetic field homogeneities due to the susceptibility match.

Unfortunately, it is technically demanding to fill the ear cavities of a mouse brain with water or other medium invasively.

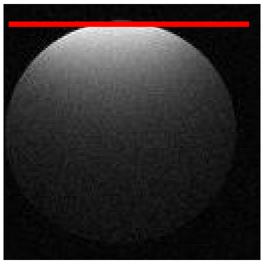

Figure 5.6. The axial gradient echo image of a water-filled tube. The image was collected with a surface (receiving) and volume (transmitting) coil pair. It is noted that the signal intensity drops significantly along the direction perpendicular to the surface coil (red line).

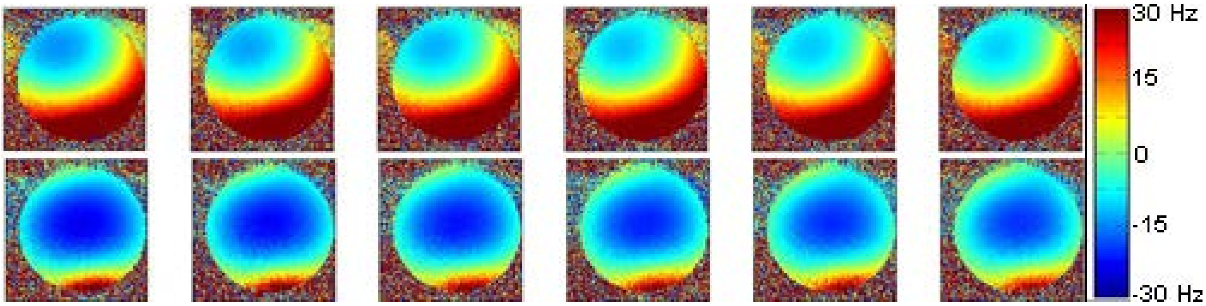

Figure 5.7. Fieldmaps of a water-filled tube after manual shimming (top) and automatic shimming (bottom). Images are displayed on a scale of [-30Hz, 30Hz].

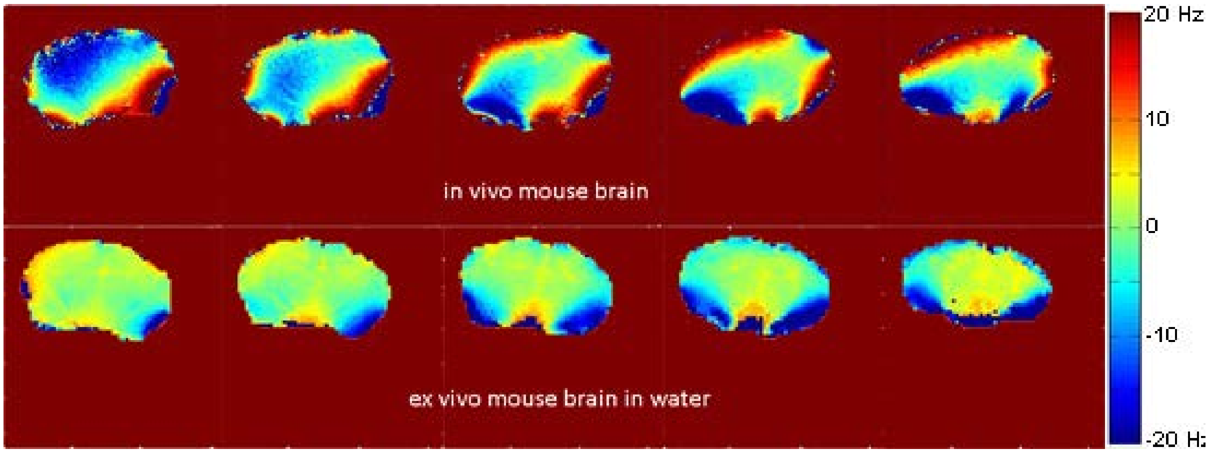

Figure 5.8. Fieldmaps of an *in vivo* mouse brain (top) and an *ex vivo* mouse brain (bottom) merging in water after automatic shimming. Images are displayed on a scale of [-20Hz, 20Hz].

VSF method reduces signal loss due to macroscopic magnetic field inhomogeneities

Figure 5.8 shows the 30th gradient-echo qBOLD images from five contiguous slices before and after correction for macroscopic magnetic field inhomogeneities. It is evident that the 'visible' brain regions extend significantly on the images after correction for macroscopic inhomogeneities using the Voxel Spread Function method.

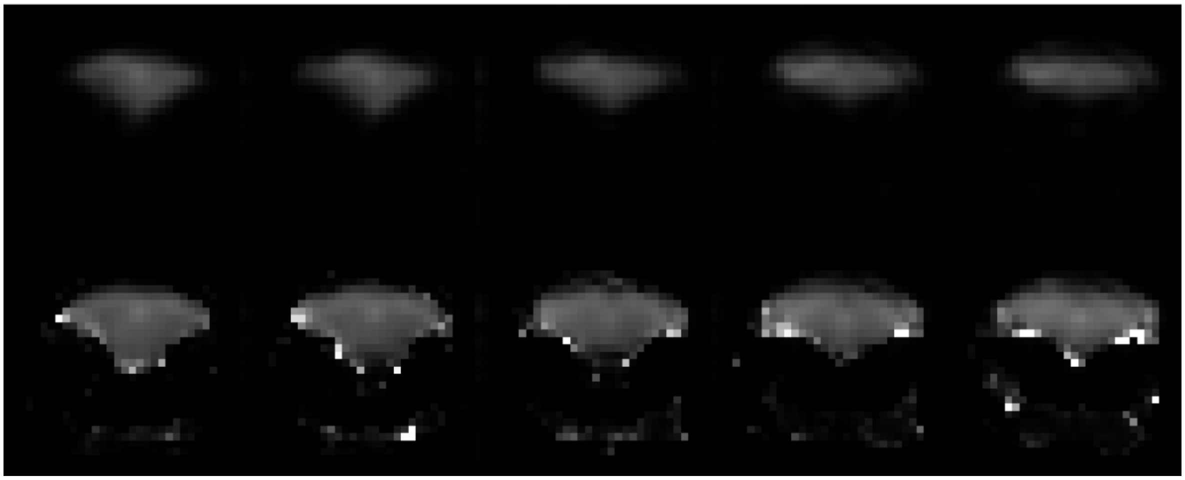

Figure 5.9. Representitive 30th gradient-echo qBOLD images from five contiguous slices before (top) and after (bottom) correction for macroscopic inhomogeneities using the Voxel Spread Function method.

Resulting OEF and dCBV maps

The fitted OEF and dCBV maps for an irradiated mouse brain at 4 weeks post irradiation, as well as the corresponding T_1W post-Gd enhanced images, are shown in Figure 5.9. The necrotic regions indicated by the minor hyperintensity regions on the T_1W images have high OEF values and low dCBV values, which are consistent with our hypothesis. However, OEF values of the undamaged brain tissue are approximately 10-20%, far lower than the OEF values of normal brain tissue (~40%) reported elsewhere [171-173]. dCBV values of the regions near the edge of the brain are extremely high (>20%), most likely due to imperfect corrections for macroscopic magnetic field inhomogeneities.

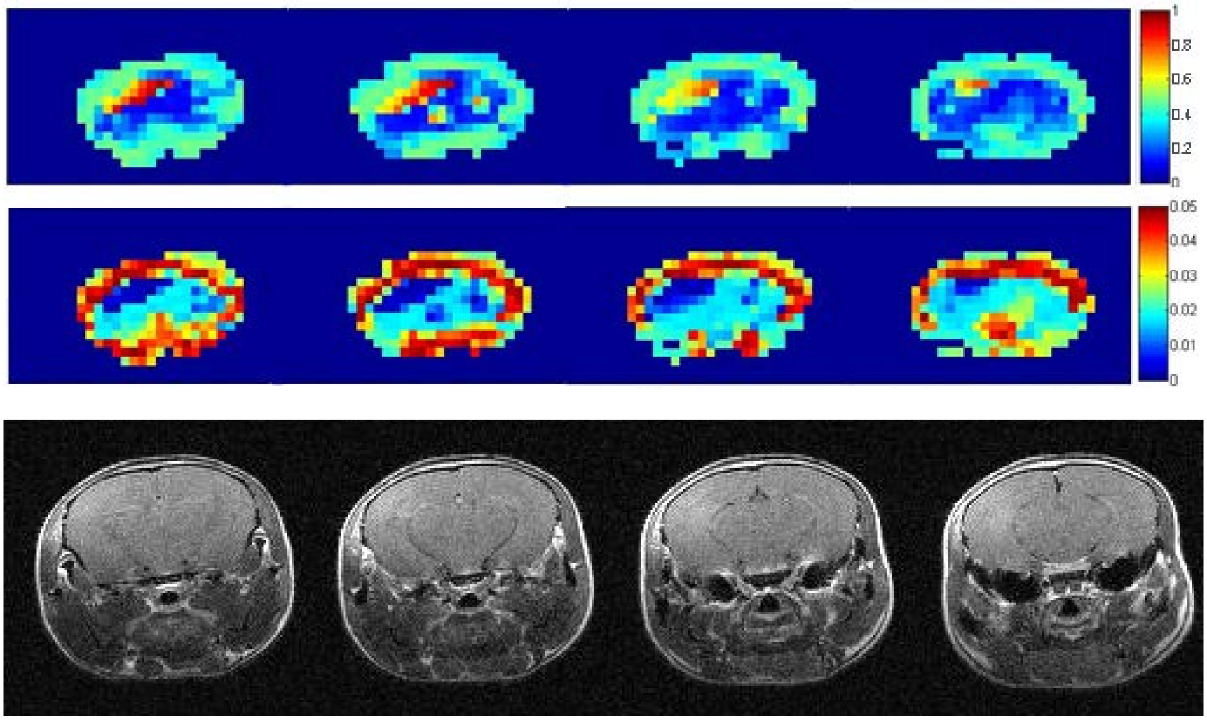

Figure 5.10. OEF (top), dCBV (middle) maps and corresponding T1-weighted images (bottom) for an irradiated mouse at 4 weeks following a single 50-Gy dose of radiation. OEF maps are displayed on a scale of [0%, 100%] and dCBV maps are displayed on a scale of [0%, 5%].

5.4 Discussion

Although the qBOLD method has been demonstrated to provide regional, *in vivo* absolute measurement of OEF and dCBV in human brain, it does not produce convincing results in the mouse brain. SNR and the effects of macroscopic magnetic field homogeneities are two major factors that determine the feasibility of the qBOLD method. As suggested by the numerical simulation, a minimum SNR of 400 is required to decouple OEF and dCBV. However, the simulation has its limitation due to the assumption of an ideal homogeneous magnetic field. The imperfect correction of macroscopic magnetic field inhomogeneities will highly undermine the accuracy of estimates of OEF and dCBV. Therefore, the required SNR in practice should be much higher than 400. Switching to high field may not help, because both BOLD contrast and the effect of macroscopic magnetic field inhomogeneites are proportional to the field strength. Performing qBOLD experiments in a larger brain, such as rat brain, is a plausible option that provides x2 SNR using the same data matrix used in our mouse study.

Shimming and post-processing correction are two ways to reduce the effects of macroscopic magnetic field inhomogeneities. It has been suggested that the shimming of mouse brain can be improved by placing a half-moon shaped head cap filled with 2% agarose gel between the mouse head and surface coil [174]. However, no significant improvement was observed when this experiment was attempted (data not shown). Further, the air-filled ear cavities, the primary sources of the macroscopic magnetic field inhomogeneities, are difficult to overcome for *in vivo* mouse studies.

The voxel spread function (VSF) method has been validated in a phantom study. In *in vivo* mouse brain studies, it helps to recover the long-TE GE signal near the mouse ears. However, the distorted OEF and dCBV maps suggest that the effects of macroscopic inhomogeneities were not completely eliminated. As mentioned, an accurate field map is needed in the calculation of the VSF function. In our experiments, the field map was calculated from the phase information of low-resolution qBOLD data. Measuring a high-resolution field map from another independent scan may improve the performance of the VSF method.

Macroscopic magnetic field inhomogeneities can be considered to be static if the sample does not move. It may be possible to decouple these static effects from the deoxyhemoglobin-induced effects by changing blood flow in the mouse brain. For example, carbon dioxide leads to increased blood flow, resulting in enhanced oxyhemoglobin concentration and then increased MR signal. The effects of macroscopic inhomogeneities can then be eliminated by calculating the ratio of MR signals generated with two different breathing gases (100% oxygen vs. 95% oxygen + 5% carbon dioxide). However, new concerns arise, including smaller contrast, other factors affecting cerebral blood flow (e.g., breathing rates, heartbeat), and increased scan time (x2 at least).

Independent verification of blood oxygen level must be included in future studies. The OEF values in normal brain tissue have been hypothesized to have a homogeneous distribution with a mean value of 40%. But the blood oxygen levels fluctuate among animals and vary from time to time. An independent *in vivo* measurement of blood oxygen levels at specific sites in the brain can help validate the qBOLD method in rodents.

5.5 Conclusion

A high SNR (400 at least) is required to decouple OEF and dCBV. The VSF function reduces the effect of macroscopic magnetic field inhomogeneities. With current shimming methods, imaging parameters, and post-process algorithms, the resulting OEF and dCBV maps in the mouse brain generated by qBOLD method are still not reliable. Efforts to boost the SNR, improve the shimming and eliminate the effects of macroscopic magnetic field inhomogeneities are ongoing.

References

1. Ogawa, S., et al., *Brain magnetic resonance imaging with contrast dependent on blood oxygenation.* Proc Natl Acad Sci U S A, 1990. **87**(24): p. 9868-72.
2. Derdeyn, C.P., et al., *Variability of cerebral blood volume and oxygen extraction: stages of cerebral haemodynamic impairment revisited.* Brain, 2002. **125**(Pt 3): p. 595-607.
3. Iadecola, C., *Neurovascular regulation in the normal brain and in Alzheimer's disease.* Nat Rev Neurosci, 2004. **5**(5): p. 347-60.
4. Iadecola, C., *Rescuing troubled vessels in Alzheimer disease.* Nat Med, 2005. **11**(9): p. 923-4.
5. Yamauchi, H., et al., *[Cerebral hemodynamics and risk for recurrent stroke in symptomatic internal carotid artery occlusion].* Rinsho Shinkeigaku, 1999. **39**(5): p. 513-9.
6. Derdeyn, C.P., R.L. Grubb, Jr., and W.J. Powers, *Cerebral hemodynamic impairment: methods of measurement and association with stroke risk.* Neurology, 1999. **53**(2): p. 251-9.
7. Mintun, M.A., et al., *Brain Oxygen Utilization Measured with O-15 Radiotracers and Positron Emission Tomography.* Journal of Nuclear Medicine, 1984. **25**(2): p. 177-187.
8. Yablonskiy, D.A. and E.M. Haacke, *Theory of NMR signal behavior in magnetically inhomogeneous tissues: the static dephasing regime.* Magn Reson Med, 1994. **32**(6): p. 749-63.
9. Yablonskiy, D.A., *Quantitation of intrinsic magnetic susceptibility-related effects in a tissue matrix. Phantom study.* Magnetic Resonance in Medicine, 1998. **39**(3): p. 417-428.
10. Valk, P.E. and W.P. Dillon, *Radiation-Injury of the Brain.* American Journal of Roentgenology, 1991. **156**(4): p. 689-706.
11. He, X. and D.A. Yablonskiy, *Quantitative BOLD: Mapping of human cerebral deoxygenated blood volume and oxygen extraction fraction: Default state.* Magnetic Resonance in Medicine, 2007. **57**(1): p. 115-126.
12. He, X. and D.A. Yablonskiy, *Quantitative BOLD: mapping of human cerebral deoxygenated blood volume and oxygen extraction fraction: default state.* Magn Reson Med, 2007. **57**(1): p. 115-26.
13. Alexiou, G.A., et al., *Glioma recurrence versus radiation necrosis: accuracy of current imaging modalities.* J Neurooncol, 2009. **95**(1): p. 1-11.
14. Yablonskiy, D.A., *Quantitation of intrinsic magnetic susceptibility-related effects in a tissue matrix. Phantom study.* Magn Reson Med, 1998. **39**(3): p. 417-28.
15. Kelly, S.E., *Gibbs phenomenon for wavelets.* Applied and Computational Harmonic Analysis, 1996. **3**(1): p. 72-81.
16. Fernandez-Seara, M.A. and F.W. Wehrli, *Postprocessing technique to correct for background gradients in image-based R*(2) measurements.* Magn Reson Med, 2000. **44**(3): p. 358-66.
17. Bashir, A. and D.A. Yablonskiy, *Natural linewidth chemical shift imaging (NL-CSI).* Magn Reson Med, 2006. **56**(1): p. 7-18.
18. Yablonskiy, D.A., et al., *Voxel spread function method for correction of magnetic field inhomogeneity effects in quantitative gradient-echo-based MRI.* Magn Reson Med.
19. Ralchle, M.E. and A.Z. Snyder, *A default mode of brain function: A brief history of an evolving idea.* Neuroimage, 2007. **37**(4): p. 1083-1090.

20. Yamauchi, H., et al., *Significance of increased oxygen extraction fraction in five-year prognosis of major cerebral arterial occlusive diseases.* Journal of Nuclear Medicine, 1999. **40**(12): p. 1992-1998.
21. Diringer, M.N., et al., *No reduction in cerebral metabolism as a result of early moderate hyperventilation following severe traumatic brain injury.* Journal of Neurosurgery, 2000. **92**(1): p. 7-13.
22. Adamczak, J.M., et al., *High field BOLD response to forepaw stimulation in the mouse.* Neuroimage. **51**(2): p. 704-12.

Chapter 6 Summary and Future Research

6.1 Summary

In this thesis work, we have developed a novel murine model of late time-to-onset radiation necrosis by employing the Leksell Gamma Knife Perfexion to stereotactically deliver radiation to one hemisphere of the mouse brain. This animal model can be used to reproducibly study radiation necrosis that simulates changes noted in the brains of human patients with radiation necrosis. A four-level histologic scoring system was developed to grade the severity of radiation necrosis. The onset and progression of RN in this model can be quantitatively characterized by both preclinical MRI and histology.

The efficacies of SB 415286, an inhibitor of glycogen synthase kinase 3β (GSK-3β), as a neuroprotectant, and bevacizumab (Avastin) and B20-4.1.1, both vascular endothelial growth factor (VEGF) inhibitors, as mitigators of radiation necrosis in mice have been determined. B20-4.1.1 significantly reduces the progression of RN in the mouse brain following a single 50-Gy dose of radiation, while bevacizumab shows only a temporal mitigative effect during the early stage of RN. When given prior to irradiation, SB 415286 also slows the progression of RN and does not reduce the therapeutic efficacy of radiation on tumors.

The possibility of utilizing qBOLD method to quantify the hemodynamic parameters in mouse brain, including OEF and dCBV, has been discussed. Although qBOLD has been validated in phantom and human studies, a combination of the significantly decreased SNR and severe macroscopic magnetic field inhomogeneites, mainly resulting from air-filled ear cavities, complicates the application of qBOLD in the mouse brain. With current shimming methods, scan parameters, and post-process algorithms, the decoupling of OEF and dCBV in the mouse brain using the qBOLD method is not reliable.

6.2 Future research

Optimize the dosing schedule of B20-4.1.1 in the treatment of RN

Outstanding questions also remain regarding the ideal dosing schemes and the treatment periods for anti-VEGF-Ab therapy. Multiple dosing schemes, ranging from 5 mg/kg to 10 mg/kg have been reported in the treatments of tumor and radiation necrosis in both human and animal studies. Typically, bevacizumab, with a half-life of approximately 20 days in humans, is administered once every 2 or 3 weeks in patients, and once or twice weekly in mice. For our mitigation study, a high-end dosing scheme (10 mg/kg, twice weekly) was chosen and demonstrated promising mitigative effects on radiation necrosis in mice. Nonetheless, minimizing the dose required to effective control the progression of necrosis will reduce patient costs and potential side effects, thereby improving the likelihood of effective clinical translation. Studies measuring the effects of using lower doses of B20-4.1.1 in our mouse model are ongoing in our lab. Also, in the current studies, irradiated mice were treated with bevacizumab or B20-4.1.1 for 7 or 8 weeks, beginning with the first radiographic sign of radiation necrosis. However, the mitigative effectiveness found upon initiating the treatment earlier (e.g., immediately following irradiation) or stopping the treatment after a fixed period of time (e.g., 4 weeks) remain to be investigated.

Verify the mechanism of anti-VEGF antibody in the treatment of RN

The DCE experiments verified that the anti-VEGF therapy decreases the vascular permeability in the necrotic region; however, the role of BBB breakdown in the development of RN is still not fully understood. One hypothesis explaining the action of anti-VEGF therapy claims that the acute BBB breakdown leads to a change in the surrounding micro environment and consequently, the onset of radiation necrosis [16]. However, we did not observe any acute injury (e.g., immediately following the irradiation and up to 4 weeks) in this Gamma Knife mouse model of radiation necrosis, by either DCE measurement or Evans Blue stain [175]. As the development of RN has been suggested to be a continuous process [16] and biological changes are expected immediately following the high-dose irradiation, DCE MR imaging and Evans Blue stain may not have sufficient sensitivity to detect the cellular response. Therefore, future studies that address mechanism of action need include other cellular biomarkers.

Determine the efficacy of other commercialized GSK-3β inhibitors as neuroprotectant

Our results demonstrate the significant neuroprotective effect of SB 415286. However, SB 415286 is no longer being pursued clinically by Glaxo SmithKline because of toxicity concerns. Future neuroprotection studies will utilize other GSK-3β inhibitors, such as lithium and valproic acid.

Improve qBOLD in the brain of small animal

1). Performing qBOLD experiments in a larger brain, such as rat brain, is an alternative providing x2 SNR with the same data matrix used in the current mouse study. Also, a larger brain enables the selection of tissue far away from the anatomic features which cause severe magnetic field inhomogeneities.

2). An independent measurement of the high-resolution field map may improve the accuracy of the VSF method and lead to a better correction of magnetic field inhomogeneities.

3). Changing blood flow in the mouse brain may enable decoupling of the macroscopic magnetic field inhomogeneities, which are static if the sample does not move, from the deoxyhemoglobin-induced effects. A practical way is to switch the composition of breathing gase (e.g., 100%

oxygen vs. 95% oxygen + 5% carbon dioxide). Carbon dioxide leads to increased blood flow, resulting in enhanced oxyhemoglobin concentration and increased MR signal. The effects of macroscopic inhomogeneities can then be eliminated by calculating the ratio of MR signals generated with these two different breathing gases.

4). OEF values in the normal brain tissue have been hypothesized to have a homogeneous distribution with a mean value of 40%. But the blood oxygen levels fluctuate among animals and vary from time to time. An independent *in vivo* measurement of blood oxygen levels at specific sites in the brain can help validate the qBOLD method.

Develop an animal model of tumor and necrosis

Developing methods at the pre-clinical level to differentiate recurrent tumor and radiation necrosis requires the development of a mixed animal model of tumor and necrosis. The major difficulties are i) to coordinate the progression timelines of tumor and necrosis; ii) to accurately irradiate a portion of tumor in order to produce a mixture of tumor and necrosis. A recent paper described a model of radiation necrosis in rats bearing human glioblastoma (GBM) in a small group of rats (n=3) [102]. A treatment plan was generated using a 4 mm radiosurgery cone such that one portion of the tumor received 100% dose of 60-Gy sufficient to cause necrosis, whereas the tumor edge at depth received only 50% or less dose, allowing for regrowth of the tumor. Future studies need direct efforts toward developing a mouse model of RN in tumor-bearing animals.

References

1. Giglio, P. and M.R. Gilbert, *Cerebral radiation necrosis.* Neurologist, 2003. **9**(4): p. 180-188.
2. Mori, Y., et al., *Effects of stereotactic radiosurgery on an animal model of hippocampal epilepsy.* Neurosurgery, 2000. **46**(1): p. 157-165.
3. Stupp, R., et al., *Effects of radiotherapy with concomitant and adjuvant temozolomide versus radiotherapy alone on survival in glioblastoma in a randomised phase III study: 5-year analysis of the EORTC-NCIC trial.* Lancet Oncology, 2009. **10**(5): p. 459-466.
4. Perry, A. and R.E. Schmidt, *Cancer therapy-associated CNS neuropathology: an update and review of the literature.* Acta Neuropathologica, 2006. **111**(3): p. 197-212.
5. Wong, C.S. and A.J. Van der Kogel, *Mechanisms of radiation injury to the central nervous system: implications for neuroprotection.* Molecular Interventions, 2004. **4**(5): p. 273-284.
6. Remler, M.P., W.H. Marcussen, and J. Tiller-Borsich, *The late effects of radiation on the blood brain barrier.* Int J Radiat Oncol Biol Phys, 1986. **12**(11): p. 1965-9.
7. Garden, G.A. and T. Moller, *Microglia biology in health and disease.* J Neuroimmune Pharmacol, 2006. **1**(2): p. 127-37.
8. Monje, M.L., H. Toda, and T.D. Palmer, *Inflammatory blockade restores adult hippocampal neurogenesis.* Science, 2003. **302**(5651): p. 1760-5.
9. Lee, T.C., et al., *Chronic administration of the angiotensin-converting enzyme inhibitor, ramipril, prevents fractionated whole-brain irradiation-induced perirhinal cortex-dependent cognitive impairment.* Radiat Res. **178**(1): p. 46-56.
10. Robbins, M.E., et al., *The AT1 receptor antagonist, L-158,809, prevents or ameliorates fractionated whole-brain irradiation-induced cognitive impairment.* Int J Radiat Oncol Biol Phys, 2009. **73**(2): p. 499-505.
11. Acharya, M.M., et al., *Human neural stem cell transplantation ameliorates radiation-induced cognitive dysfunction.* Cancer Res. **71**(14): p. 4834-45.
12. Reinhold, H.S., et al., *Development of blood vessel-related radiation damage in the fimbria of the central nervous system.* Int J Radiat Oncol Biol Phys, 1990. **18**(1): p. 37-42.
13. Schultheiss, T.E. and L.C. Stephens, *Invited review: permanent radiation myelopathy.* Br J Radiol, 1992. **65**(777): p. 737-53.
14. Brown, W.R., et al., *Capillary loss precedes the cognitive impairment induced by fractionated whole-brain irradiation: a potential rat model of vascular dementia.* J Neurol Sci, 2007. **257**(1-2): p. 67-71.
15. Morris, G.M., et al., *Boron neutron capture irradiation of the rat spinal cord: histopathological evidence of a vascular-mediated pathogenesis.* Radiat Res, 1996. **146**(3): p. 313-20.
16. Greene-Schloesser, D., et al., *Radiation-induced brain injury: A review.* Front Oncol. **2**: p. 73.
17. Kumar, A.J., et al., *Malignant gliomas: MR imaging spectrum of radiation therapy- and chemotherapy-induced necrosis of the brain after treatment.* Radiology, 2000. **217**(2): p. 377-384.
18. Mullins, M.E., et al., *Radiation necrosis versus glioma recurrence: Conventional MR imaging clues to diagnosis.* American Journal of Neuroradiology, 2005. **26**(8): p. 1967-1972.
19. Dequesada, I.M., et al., *Can Standard Magnetic Resonance Imaging Reliably Distinguish Recurrent Tumor from Radiation Necrosis after Radiosurgery for Brain Metastases? A Radiographic-Pathological Study.* Neurosurgery, 2008. **63**(5): p. 898-903.
20. Tsuruda, J.S., et al., *Radiation Effects on Cerebral White Matter - Mr Evaluation.* American Journal of Roentgenology, 1987. **149**(1): p. 165-171.
21. Schaefer, P.W., et al., *Assessing tissue viability with MR diffusion and perfusion imaging.* American Journal of Neuroradiology, 2003. **24**(3): p. 436-443.
22. Hein, P.A., et al., *Diffusion-weighted Imaging in the follow-up of treated high-grade gliomas: Tumor recurrence versus radiation injury.* American Journal of Neuroradiology, 2004. **25**(2): p. 201-209.
23. Wang, S.L., et al., *Evaluation of radiation necrosis and malignant glioma in rat models using diffusion tensor MR imaging.* Journal of Neuro-Oncology, 2012. **107**(1): p. 51-60.

24. Asao, C., et al., *Diffusion-weighted imaging of radiation-induced brain injury for differentiation from tumor recurrence.* American Journal of Neuroradiology, 2005. **26**(6): p. 1455-1460.
25. Castillo, M., et al., *Apparent diffusion coefficients in the evaluation of high-grade cerebral gliomas.* American Journal of Neuroradiology, 2001. **22**(1): p. 60-64.
26. Catalaa, I., et al., *Perfusion, diffusion and spectroscopy values in newly diagnosed cerebral gliomas.* Nmr in Biomedicine, 2006. **19**(4): p. 463-475.
27. Padhani, A.R. and J.E. Husband, *Dynamic contrast-enhanced MRI studies in oncology with an emphasis on quantification, validation and human studies.* Clinical Radiology, 2001. **56**(8): p. 607-620.
28. Aronen, H.J. and J. Perkio, *Dynamic susceptibility contrast MRI of gliomas.* Neuroimaging Clinics of North America, 2002. **12**(4): p. 501-+.
29. Covarrubias, D.J., B.R. Rosen, and M.H. Lev, *Dynamic magnetic resonance perfusion imaging of brain tumors.* Oncologist, 2004. **9**(5): p. 528-537.
30. Ellika, S.K., et al., *Role of perfusion CT in glioma grading and comparison with conventional MR imaging features.* American Journal of Neuroradiology, 2007. **28**(10): p. 1981-1987.
31. Sugahara, T., et al., *Posttherapeutic intraaxial brain tumor: the value of perfusion-sensitive contrast-enhanced MR imaging for differentiating tumor recurrence from nonneoplastic contrast-enhancing tissue.* AJNR Am J Neuroradiol, 2000. **21**(5): p. 901-9.
32. Jain, R.K., R.T. Tong, and L.L. Munn, *Effect of vascular normalization by antiangiogenic therapy on interstitial hypertension, peritumor edema, and lymphatic metastasis: insights from a mathematical model.* Cancer Res, 2007. **67**(6): p. 2729-35.
33. Jain, R.K., *Normalizing tumor vasculature with anti-angiogenic therapy: a new paradigm for combination therapy.* Nat Med, 2001. **7**(9): p. 987-9.
34. Ando, K., et al., *[Usefulness of Cho/Cr ratio in proton MR spectroscopy for differentiating residual/recurrent glioma from non-neoplastic lesions]*. Nihon Igaku Hoshasen Gakkai Zasshi, 2004. **64**(3): p. 121-6.
35. Dowling, C., et al., *Preoperative proton MR spectroscopic imaging of brain tumors: correlation with histopathologic analysis of resection specimens.* AJNR Am J Neuroradiol, 2001. **22**(4): p. 604-12.
36. Rock, J.P., et al., *Associations among magnetic resonance spectroscopy, apparent diffusion coefficients, and image-guided histopathology with special attention to radiation necrosis.* Neurosurgery, 2004. **54**(5): p. 1111-1117.
37. Zeng, Q.S., et al., *Multivoxel 3D proton MR spectroscopy in the distinction of recurrent glioma from radiation injury.* Journal of Neuro-Oncology, 2007. **84**(1): p. 63-69.
38. Sundgren, P.C., et al., *Differentiation of recurrent brain tumor versus radiation injury using diffusion tensor imaging in patients with new contrast-enhancing lesions.* Magnetic Resonance Imaging, 2006. **24**(9): p. 1131-1142.
39. Schlemmer, H.P., et al., *Proton MR spectroscopic evaluation of suspicious brain lesions after stereotactic radiotherapy.* American Journal of Neuroradiology, 2001. **22**(7): p. 1316-1324.
40. Chong, V.F.H., et al., *Temporal lobe changes following radiation therapy: imaging and proton MR spectroscopic findings.* European Radiology, 2001. **11**(2): p. 317-324.
41. Zhou, J.Y., et al., *Differentiation between glioma and radiation necrosis using molecular magnetic resonance imaging of endogenous proteins and peptides.* Nature Medicine, 2011. **17**(1): p. 130-U308.
42. Alexiou, G.A., et al., *Glioma recurrence versus radiation necrosis: accuracy of current imaging modalities.* J Neurooncol, 2009. **95**(1): p. 1-11.
43. Brismar, J., G.H. Roberson, and K.R. Davis, *Radiation necrosis of the brain. Neuroradiological considerations with computed tomography.* Neuroradiology, 1976. **12**(2): p. 109-13.
44. Mikhael, M.A., *Radiation Necrosis of the Brain - Correlation between Patterns on Computed-Tomography and Dose of Radiation.* Journal of Computer Assisted Tomography, 1979. **3**(2): p. 241-250.
45. Ogawa, T., et al., *Delayed radiation necrosis of brain evaluated positron emission tomography.* Tohoku J Exp Med, 1988. **155**(3): p. 247-60.
46. Black, K.L., et al., *Use of thallium-201 SPECT to quantitate malignancy grade of gliomas.* J Neurosurg, 1989. **71**(3): p. 342-6.
47. Kline, J.L., R.B. Noto, and M. Glantz, *Single-photon emission CT in the evaluation of recurrent brain tumor in patients treated with gamma knife radiosurgery or conventional radiation therapy.* AJNR Am J Neuroradiol, 1996. **17**(9): p. 1681-6.
48. Yoshii, Y., et al., *Cerebral radiation necrosis with accumulation of thallium 201 on single-photon emission CT.* AJNR Am J Neuroradiol, 1996. **17**(9): p. 1773-6.

49. Moody, E.B., et al., *Thallium-avid cerebral radiation necrosis.* Clin Nucl Med, 1994. **19**(7): p. 611-3.
50. Doyle, W.K., et al., *Differentiation of cerebral radiation necrosis from tumor recurrence by [18F]FDG and 82Rb positron emission tomography.* J Comput Assist Tomogr, 1987. **11**(4): p. 563-70.
51. Di Chiro, G., et al., *Cerebral necrosis after radiotherapy and/or intraarterial chemotherapy for brain tumors: PET and neuropathologic studies.* AJR Am J Roentgenol, 1988. **150**(1): p. 189-97.
52. Glantz, M.J., et al., *Identification of early recurrence of primary central nervous system tumors by [18F]fluorodeoxyglucose positron emission tomography.* Ann Neurol, 1991. **29**(4): p. 347-55.
53. Kim, E.E., et al., *Differentiation of residual or recurrent tumors from post-treatment changes with F-18 FDG PET.* Radiographics, 1992. **12**(2): p. 269-79.
54. Ogawa, T., et al., *Clinical value of PET with 18F-fluorodeoxyglucose and L-methyl-11C-methionine for diagnosis of recurrent brain tumor and radiation injury.* Acta Radiol, 1991. **32**(3): p. 197-202.
55. Shaw, P.J. and D. Bates, *Conservative Treatment of Delayed Cerebral Radiation Necrosis.* Journal of Neurology Neurosurgery and Psychiatry, 1984. **47**(12): p. 1338-1341.
56. Siu, A., et al., *Radiation necrosis following treatment of high grade glioma-a review of the literature and current understanding.* Acta Neurochirurgica, 2012. **154**(2): p. 191-201.
57. But, Q.C., et al., *The efficacy of hyperbaric oxygen therapy in the treatment of radiation-induced late side effects.* International Journal of Radiation Oncology Biology Physics, 2004. **60**(3): p. 871-878.
58. Kohshi, K., et al., *Successful treatment of radiation-induced brain necrosis by hyperbaric oxygen therapy.* Journal of the Neurological Sciences, 2003. **209**(1-2): p. 115-117.
59. Tibbles, P.M. and J.S. Edelsberg, *Medical progress - Hyperbaric-oxygen therapy.* New England Journal of Medicine, 1996. **334**(25): p. 1642-1648.
60. Ferrara, N., K.J. Hillan, and W. Novotny, *Bevacizumab (Avastin), a humanized anti-VEGF monoclonal antibody for cancer therapy.* Biochemical and Biophysical Research Communications, 2005. **333**(2): p. 328-335.
61. Gonzalez, J., et al., *Effect of bevacizumab on radiation necrosis of the brain.* International Journal of Radiation Oncology Biology Physics, 2007. **67**(2): p. 323-326.
62. Jeyaretna, D.S., et al., *Exacerbation of Cerebral Radiation Necrosis by Bevacizumab.* Journal of Clinical Oncology, 2011. **29**(7): p. E159-E162.
63. Torcuator, R., et al., *Initial experience with bevacizumab treatment for biopsy-confirmed cerebral radiation necrosis.* Neuro-Oncology, 2007. **9**(4): p. 580-581.
64. Levin, V.A., et al., *Randomized Double-Blind Placebo-Controlled Trial of Bevacizumab Therapy for Radiation Necrosis of the Central Nervous System.* International Journal of Radiation Oncology Biology Physics, 2011. **79**(5): p. 1487-1495.
65. Rahmathulla, G., et al., *Laser interstitial thermal therapy for focal cerebral radiation necrosis: a case report and literature review.* Stereotact Funct Neurosurg. **90**(3): p. 192-200.
66. Levitt, M.H., *Spin dynamics : basics of nuclear magnetic resonance*. 2nd ed. 2008, Chichester, England ; Hoboken, NJ: John Wiley & Sons. xxv, 714 p., [7] p. of plates.
67. Bernstein, M.A., K.F. King, and Z.J. Zhou, *Handbook of MRI pulse sequences*. 2004, Amsterdam ; Boston: Academic Press. xxii,1017 p.
68. Caravan, P., et al., *Gadolinium(III) chelates as MRI contrast agents: Structure, dynamics, and applications.* Chemical Reviews, 1999. **99**(9): p. 2293-2352.
69. Botta, M., *Second coordination sphere water molecules and relaxivity of gadolinium(III) complexes: Implications for MRI contrast agents.* European Journal of Inorganic Chemistry, 2000(3): p. 399-407.
70. Seltzer, S., A.S. Mark, and S.W. Atlas, *CNS sarcoidosis: evaluation with contrast-enhanced MR imaging.* AJNR Am J Neuroradiol, 1991. **12**(6): p. 1227-33.
71. Yuan, C., et al., *Contrast-enhanced high resolution MRI for atherosclerotic carotid artery tissue characterization.* J Magn Reson Imaging, 2002. **15**(1): p. 62-7.
72. Seki, H., M. Kimura, and K. Sakai, *Myometrial invasion of endometrial carcinoma: assessment with dynamic MR and contrast-enhanced T1-weighted images.* Clin Radiol, 1997. **52**(1): p. 18-23.
73. Rowley, H.A., et al., *Contrast-enhanced MR imaging of brain lesions: a large-scale intraindividual crossover comparison of gadobenate dimeglumine versus gadodiamide.* AJNR Am J Neuroradiol, 2008. **29**(9): p. 1684-91.
74. Herskovits, E.H., R. Itoh, and E.R. Melhem, *Accuracy for detection of simulated lesions: comparison of fluid-attenuated inversion-recovery, proton density--weighted, and T2-weighted synthetic brain MR imaging.* AJR Am J Roentgenol, 2001. **176**(5): p. 1313-8.
75. Arakia, Y., et al., *MR fluid-attenuated inversion recovery imaging as routine brain T2-weighted imaging.*

Eur J Radiol, 1999. **32**(2): p. 136-43.

76. Bartzokis, G., et al., *The incidence of T2-weighted MR imaging signal abnormalities in the brain of cocaine-dependent patients is age-related and region-specific.* AJNR Am J Neuroradiol, 1999. **20**(9): p. 1628-35.
77. Okubo, T., et al., *Detection of brain metastasis: comparison of Turbo-FLAIR imaging, T2-weighted imaging and double-dose gadolinium-enhanced MR imaging.* Radiat Med, 1998. **16**(4): p. 273-81.
78. Hockings, P.D., et al., *Correlation between high-field T2-weighted MR imaging and histology of ischemic lesions in gerbil brain.* J Magn Reson Imaging, 1995. **5**(4): p. 437-42.
79. O'Connor, J.P.B., et al., *DCE-MRI biomarkers in the clinical evaluation of antiangiogenic and vascular disrupting agents.* British Journal of Cancer, 2007. **96**(2): p. 189-195.
80. Tofts, P.S., et al., *Estimating kinetic parameters from dynamic contrast-enhanced T(1)-weighted MRI of a diffusable tracer: Standardized quantities and symbols.* Journal of Magnetic Resonance Imaging, 1999. **10**(3): p. 223-232.
81. Patankar, T.F., et al., *Is volume transfer coefficient (K-trans) related to histologic grade in human gliomas?* American Journal of Neuroradiology, 2005. **26**(10): p. 2455-2465.
82. Yankeelov, T.E., et al., *Quantitative pharmacokinetic analysis of DCE-MRI data without an arterial input function: a reference region model.* Magnetic Resonance Imaging, 2005. **23**(4): p. 519-529.
83. Wang, B., Z.Q. Gao, and X. Yan, *Correlative study of angiogenesis and dynamic contrast-enhanced magnetic resonance imaging features of hepatocellular carcinoma.* Acta Radiol, 2005. **46**(4): p. 353-8.
84. Iadecola, C., *Neurovascular regulation in the normal brain and in Alzheimer's disease.* Nature Reviews Neuroscience, 2004. **5**(5): p. 347-360.
85. Raichle, M.E. and D.A. Gusnard, *Appraising the brain's energy budget.* Proceedings of the National Academy of Sciences of the United States of America, 2002. **99**(16): p. 10237-10239.
86. Derdeyn, C.P., et al., *Variability of cerebral blood volume and oxygen extraction: stages of cerebral haemodynamic impairment revisited.* Brain, 2002. **125**: p. 595-607.
87. Davda, S. and T. Bezabeh, *Advances in methods for assessing tumor hypoxia in vivo: Implications for treatment planning.* Cancer and Metastasis Reviews, 2006. **25**(3): p. 469-480.
88. Tatum, J.L., et al., *Hypoxia: Importance in tumor biology, noninvasive measurement by imaging, and value of its measurement in the management of cancer therapy.* International Journal of Radiation Biology, 2006. **82**(10): p. 699-757.
89. Barajas, R.F., et al., *Distinguishing Recurrent Intra-Axial Metastatic Tumor from Radiation Necrosis Following Gamma Knife Radiosurgery Using Dynamic Susceptibility-Weighted Contrast-Enhanced Perfusion MR Imaging.* American Journal of Neuroradiology, 2009. **30**(2): p. 367-372.
90. Dean, B.L., et al., *Cerebral Hemodynamics and Cerebral Blood-Volume - Mr Assessment Using Gadolinium Contrast Agents and T1-Weighted Turbo-Flash Imaging.* American Journal of Neuroradiology, 1992. **13**(1): p. 39-48.
91. Schwartz, R.B., et al., *Radiation Necrosis Vs High-Grade Recurrent Glioma - Differentiation by Using Dual-Isotope Spect with Tl-201 and Tc-99m-Hmpao.* American Journal of Roentgenology, 1992. **158**(2): p. 399-404.
92. Mintun, M.A., et al., *Brain Oxygen Utilization Measured with O-15 Radiotracers and Positron Emission Tomography.* Journal of Nuclear Medicine, 1984. **25**(2): p. 177-187.
93. Yablonskiy, D.A., *Quantitation of intrinsic magnetic susceptibility-related effects in a tissue matrix. Phantom study.* Magnetic Resonance in Medicine, 1998. **39**(3): p. 417-428.
94. He, X. and D.A. Yablonskiy, *Quantitative BOLD: Mapping of human cerebral deoxygenated blood volume and oxygen extraction fraction: Default state.* Magnetic Resonance in Medicine, 2007. **57**(1): p. 115-126.
95. Fomchenko, E.I. and E.C. Holland, *Mouse models of brain tumors and their applications in preclinical trials.* Clinical Cancer Research, 2006. **12**(18): p. 5288-5297.
96. Miot, E., et al., *Experimental Mr Study of Cerebral Radiation-Injury - Quantitative T2 Changes over Time and Histopathologic Correlation.* American Journal of Neuroradiology, 1995. **16**(1): p. 79-85.
97. Blatt, D.R., et al., *Temporal Characteristics of Radiosurgical Lesions in an Animal-Model.* Journal of Neurosurgery, 1994. **80**(6): p. 1046-1055.
98. Tran, D.K. and R.L. Jensen, *Treatment-related brain tumor imaging changes: So-called "pseudoprogression" vs. tumor progression: Review and future research opportunities.* Surg Neurol Int. **4**(Suppl 3): p. S129-35.
99. Rabinov, J.D., et al., *MR spectroscopic changes in the rat hippocampus following proton radiosurgery.* Stereotactic and Functional Neurosurgery, 2006. **84**(4): p. 147-154.

100. Kondziolka, D., et al., *Radiobiology of Radiosurgery .2. The Rat-C6 Glioma Model.* Neurosurgery, 1992. **31**(2): p. 280-288.
101. Jost, S.C., et al., *A Novel Murine Model for Localized Radiation Necrosis and Its Characterization Using Advanced Magnetic Resonance Imaging.* International Journal of Radiation Oncology Biology Physics, 2009. **75**(2): p. 527-533.
102. Kumar, S., et al., *Development of a novel animal model to differentiate radiation necrosis from tumor recurrence.* Journal of Neuro-Oncology, 2012. **108**(3): p. 411-420.
103. Thames, H.D., Jr., et al., *Changes in early and late radiation responses with altered dose fractionation: implications for dose-survival relationships.* Int J Radiat Oncol Biol Phys, 1982. **8**(2): p. 219-26.
104. Altshuler, B., *Modeling of Dose-Response Relationships.* Environmental Health Perspectives, 1981. **42**(Dec): p. 23-27.
105. Assembly of Life Sciences (U.S.). Committee on the Biological Effects of Ionizing Radiations., *The Effects on populations of exposure to low levels of ionizing radiation, 1980*. 1980, Washington, D.C.: National Academy Press. xv, 524 p.
106. National Research Council (U.S.). Advisory Committee on the Biological Effects of Ionizing Radiations., United States. Environmental Protection Agency. Radiation Office., and National Academy of Sciences Washington D.C., *The effects on populations of exposure to low levels of ionizing radiation; report*. 1972, Washington,: National Academy of Sciences - National Research Council. xiii, 217 p.
107. National Research Council (U.S.). Advisory Committee on the Biological Effects of Ionizing Radiations., *The effects on populations of exposure to low levels of ionizing radiation*. 1976, Washington, D.C.: Division of Medical Sciences, National Academy of Sciences, National Research Council. xiii, 216 p.
108. Schollnberger, H., et al., *Explanation of protective effects of low doses of gamma-radiation with a mechanistic radiobiological model.* International Journal of Radiation Biology, 2002. **78**(12): p. 1159-1173.
109. Donnet, A., D. Valade, and J. Regis, *Gamma knife treatment for refractory cluster headache: prospective open trial.* J Neurol Neurosurg Psychiatry, 2005. **76**(2): p. 218-21.
110. Herman, J.M., et al., *Repeat gamma knife radiosurgery for refractory or recurrent trigeminal neuralgia: treatment outcomes and quality-of-life assessment.* Int J Radiat Oncol Biol Phys, 2004. **59**(1): p. 112-6.
111. Crowley, R.W., N. Pouratian, and J.P. Sheehan, *Gamma knife surgery for glioblastoma multiforme.* Neurosurg Focus, 2006. **20**(4): p. E17.
112. Stupp, R., W.P. Mason, and M.J. van den Beuf, *Radiotherapy plus concomitant and adjuvant temozolomide for newly diagnosed glioblastoma (vol 352, pg 19, 2005).* Annals of Oncology, 2005. **16**(6): p. 949-949.
113. Tsuyuguchi, N., et al., *Methionine positron emission tomography for differentiation of recurrent brain tumor and radiation necrosis after stereotactic radiosurgery - In malignant glioma.* Annals of Nuclear Medicine, 2004. **18**(4): p. 291-296.
114. Rachinger, W., et al., *Positron emission tomography with O-(2-[F-18]fluoroethyl)-L-tyrosine versus magnetic resonance imaging in the diagnosis of recurrent gliomas.* Neurosurgery, 2005. **57**(3): p. 505-511.
115. Kumar, A.J., et al., *Malignant gliomas: MR imaging spectrum of radiation therapy- and chemotherapy-induced necrosis of the brain after treatment.* Radiology, 2000. **217**(2): p. 377-84.
116. Rahmathulla, G., N.F. Marko, and R.J. Weil, *Cerebral radiation necrosis: A review of the pathobiology, diagnosis and management considerations.* Journal of Clinical Neuroscience, 2013. **20**(4): p. 485-502.
117. Mergenthaler, P., U. Dirnagl, and A. Meisel, *Pathophysiology of stroke: lessons from animal models.* Metab Brain Dis, 2004. **19**(3-4): p. 151-67.
118. van der Worp, H.B., et al., *Hypothermia in animal models of acute ischaemic stroke: a systematic review and meta-analysis.* Brain, 2007. **130**(Pt 12): p. 3063-74.
119. Clarke, M.F., et al., *Cancer stem cells--perspectives on current status and future directions: AACR Workshop on cancer stem cells.* Cancer Res, 2006. **66**(19): p. 9339-44.
120. Jiang, X., et al., *Anti-VEGF antibodies mitigate the development of radiation necrosis in mouse brain.* Clinical Cancer Research, 2013: p. in revision.
121. Conover, W.J., *Practical nonparametric statistics*. 3rd ed. Wiley series in probability and statistics. Applied probability and statistics section. 1999, New York: Wiley. viii, 584 p.
122. Schollnberger, H., et al., *Explanation of protective effects of low doses of gamma-radiation with a mechanistic radiobiological model.* Int J Radiat Biol, 2002. **78**(12): p. 1159-73.
123. Rahmathulla, G., N.F. Marko, and R.J. Weil, *Cerebral radiation necrosis: A review of the pathobiology, diagnosis and management considerations.* Journal of clinical neuroscience : official journal of the Neurosurgical Society of Australasia, 2013. **20**(4): p. 485-502.
124. Remler, M.P., W.H. Marcussen, and J. Tiller-Borsich, *The late effects of radiation on the blood brain*

barrier. International journal of radiation oncology, biology, physics, 1986. **12**(11): p. 1965-9.

125. Norden, A.D., J. Drappatz, and P.Y. Wen, *Antiangiogenic therapies for high-grade glioma.* Nature reviews. Neurology, 2009. **5**(11): p. 610-20.
126. Jain, R.K., *Normalization of tumor vasculature: An emerging concept in antiangiogenic therapy.* Science, 2005. **307**(5706): p. 58-62.
127. Dings, R.P.M., et al., *Scheduling of radiation with angiogenesis inhibitors anginex and avastin improves therapeutic outcome via vessel normalization.* Clinical Cancer Research, 2007. **13**(11): p. 3395-3402.
128. Ananthnarayan, S., et al., *Time course of imaging changes of GBM during extended bevacizumab treatment.* Journal of Neuro-Oncology, 2008. **88**(3): p. 339-347.
129. Laird, N.M. and J.H. Ware, *Random-effects models for longitudinal data.* Biometrics, 1982. **38**(4): p. 963-74.
130. Shawler, D.L., et al., *Human Immune-Response to Multiple Injections of Murine Monoclonal Igg.* Journal of Immunology, 1985. **135**(2): p. 1530-1535.
131. Herlyn, D., et al., *Specific Detection of Anti-Idiotypic Immune-Responses in Cancer-Patients Treated with Murine Monoclonal-Antibody.* Journal of Immunological Methods, 1985. **85**(1): p. 27-38.
132. Fagerberg, J., et al., *Humoral anti-idiotypic and anti-anti-idiotypic immune response in cancer patients treated with monoclonal antibody 17-1A.* Cancer Immunology Immunotherapy, 1996. **42**(2): p. 81-87.
133. Yu, L.L., et al., *Interaction between bevacizumab and murine VEGF-A: A reassessment.* Investigative Ophthalmology & Visual Science, 2008. **49**(2): p. 522-527.
134. Xu, Q.W., T. Qaum, and A.P. Adamis, *Sensitive blood-retinal barrier breakdown quantitation using Evans blue.* Investigative Ophthalmology & Visual Science, 2001. **42**(3): p. 789-794.
135. de Groot, J.F., et al., *Tumor invasion after treatment of glioblastoma with bevacizumab: radiographic and pathologic correlation in humans and mice.* Neuro-Oncology, 2010. **12**(3): p. 233-242.
136. Ferrara, N., et al., *Discovery and development of bevacizumab, an anti-VEGF antibody for treating cancer.* Nature Reviews Drug Discovery, 2004. **3**(5): p. 391-400.
137. Brandsma, D., et al., *Clinical features, mechanisms, and management of pseudoprogression in malignant gliomas.* Lancet Oncol, 2008. **9**(5): p. 453-61.
138. Ruben, J.D., et al., *Cerebral radiation necrosis: incidence, outcomes, and risk factors with emphasis on radiation parameters and chemotherapy.* Int J Radiat Oncol Biol Phys, 2006. **65**(2): p. 499-508.
139. Shi, L., et al., *Maintenance of white matter integrity in a rat model of radiation-induced cognitive impairment.* Journal of the Neurological Sciences, 2009. **285**(1-2): p. 178-184.
140. Zhou, H., et al., *Fractionated Radiation-Induced Acute Encephalopathy in a Young Rat Model: Cognitive Dysfunction and Histologic Findings.* American Journal of Neuroradiology, 2011. **32**(10): p. 1795-1800.
141. Wilson, C.M., et al., *Radiation-Induced Astrogliosis and Blood-Brain Barrier Damage Can Be Abrogated Using Anti-Tnf Treatment.* International Journal of Radiation Oncology Biology Physics, 2009. **74**(3): p. 934-941.
142. Embi, N., D.B. Rylatt, and P. Cohen, *Glycogen synthase kinase-3 from rabbit skeletal muscle. Separation from cyclic-AMP-dependent protein kinase and phosphorylase kinase.* Eur J Biochem, 1980. **107**(2): p. 519-27.
143. Leroy, K. and J.P. Brion, *Developmental expression and localization of glycogen synthase kinase-3beta in rat brain.* J Chem Neuroanat, 1999. **16**(4): p. 279-93.
144. Watcharasit, P., et al., *Direct, activating interaction between glycogen synthase kinase-3beta and p53 after DNA damage.* Proc Natl Acad Sci U S A, 2002. **99**(12): p. 7951-5.
145. Loberg, R.D., E. Vesely, and F.C. Brosius, 3rd, *Enhanced glycogen synthase kinase-3beta activity mediates hypoxia-induced apoptosis of vascular smooth muscle cells and is prevented by glucose transport and metabolism.* J Biol Chem, 2002. **277**(44): p. 41667-73.
146. Song, L., P. De Sarno, and R.S. Jope, *Central role of glycogen synthase kinase-3beta in endoplasmic reticulum stress-induced caspase-3 activation.* J Biol Chem, 2002. **277**(47): p. 44701-8.
147. Thotala, D.K., D.E. Hallahan, and E.M. Yazlovitskaya, *Inhibition of glycogen synthase kinase 3 beta attenuates neurocognitive dysfunction resulting from cranial irradiation.* Cancer Res, 2008. **68**(14): p. 5859-68.
148. Cross, D.A.E., et al., *Selective small-molecule inhibitors of glycogen synthase kinase-3 activity protect primary neurones from death*. 2001. p. 94-102.
149. Yazlovitskaya, E.M., et al., *Lithium treatment prevents neurocognitive deficit resulting from cranial irradiation.* Cancer Res, 2006. **66**(23): p. 11179-86.
150. Thotala, D.K., et al., *A New Class of Molecular Targeted Radioprotectors: Gsk-3 Beta Inhibitors.*

International Journal of Radiation Oncology Biology Physics, 2010. **76**(2): p. 557-565.

151. Medina, M. and J. Avila, *Glycogen synthase kinase-3 (GSK-3) inhibitors for the treatment of Alzheimer's disease.* Curr Pharm Des, 2010. **16**(25): p. 2790-8.

152. Klamer, G., et al., *Using Small Molecule GSK3 beta Inhibitors to Treat Inflammation.* Current Medicinal Chemistry, 2010. **17**(26): p. 2873-2881.

153. Phukan, S., et al., *GSK3 beta: role in therapeutic landscape and development of modulators.* British Journal of Pharmacology, 2010. **160**(1): p. 1-19.

154. Coghlan, M.P., et al., *Selective small molecule inhibitors of glycogen synthase kinase-3 modulate glycogen metabolism and gene transcription.* Chem Biol, 2000. **7**(10): p. 793-803.

155. Jost, S.C., et al., *In vivo imaging in a murine model of glioblastoma.* Neurosurgery, 2007. **60**(2): p. 360-70; discussion 370-1.

156. Franken, N.A., et al., *Clonogenic assay of cells in vitro.* Nat Protoc, 2006. **1**(5): p. 2315-9.

157. Ogawa, S., et al., *Brain magnetic resonance imaging with contrast dependent on blood oxygenation.* Proc Natl Acad Sci U S A, 1990. **87**(24): p. 9868-72.

158. Derdeyn, C.P., et al., *Variability of cerebral blood volume and oxygen extraction: stages of cerebral haemodynamic impairment revisited.* Brain, 2002. **125**(Pt 3): p. 595-607.

159. Iadecola, C., *Neurovascular regulation in the normal brain and in Alzheimer's disease.* Nat Rev Neurosci, 2004. **5**(5): p. 347-60.

160. Iadecola, C., *Rescuing troubled vessels in Alzheimer disease.* Nat Med, 2005. **11**(9): p. 923-4.

161. Yamauchi, H., et al., *[Cerebral hemodynamics and risk for recurrent stroke in symptomatic internal carotid artery occlusion].* Rinsho Shinkeigaku, 1999. **39**(5): p. 513-9.

162. Derdeyn, C.P., R.L. Grubb, Jr., and W.J. Powers, *Cerebral hemodynamic impairment: methods of measurement and association with stroke risk.* Neurology, 1999. **53**(2): p. 251-9.

163. Yablonskiy, D.A. and E.M. Haacke, *Theory of NMR signal behavior in magnetically inhomogeneous tissues: the static dephasing regime.* Magn Reson Med, 1994. **32**(6): p. 749-63.

164. Valk, P.E. and W.P. Dillon, *Radiation-Injury of the Brain.* American Journal of Roentgenology, 1991. **156**(4): p. 689-706.

165. He, X. and D.A. Yablonskiy, *Quantitative BOLD: mapping of human cerebral deoxygenated blood volume and oxygen extraction fraction: default state.* Magn Reson Med, 2007. **57**(1): p. 115-26.

166. Yablonskiy, D.A., *Quantitation of intrinsic magnetic susceptibility-related effects in a tissue matrix. Phantom study.* Magn Reson Med, 1998. **39**(3): p. 417-28.

167. Kelly, S.E., *Gibbs phenomenon for wavelets.* Applied and Computational Harmonic Analysis, 1996. **3**(1): p. 72-81.

168. Fernandez-Seara, M.A. and F.W. Wehrli, *Postprocessing technique to correct for background gradients in image-based R*(2) measurements.* Magn Reson Med, 2000. **44**(3): p. 358-66.

169. Bashir, A. and D.A. Yablonskiy, *Natural linewidth chemical shift imaging (NL-CSI).* Magn Reson Med, 2006. **56**(1): p. 7-18.

170. Yablonskiy, D.A., et al., *Voxel spread function method for correction of magnetic field inhomogeneity effects in quantitative gradient-echo-based MRI.* Magn Reson Med.

171. Ralchle, M.E. and A.Z. Snyder, *A default mode of brain function: A brief history of an evolving idea.* Neuroimage, 2007. **37**(4): p. 1083-1090.

172. Yamauchi, H., et al., *Significance of increased oxygen extraction fraction in five-year prognosis of major cerebral arterial occlusive diseases.* Journal of Nuclear Medicine, 1999. **40**(12): p. 1992-1998.

173. Diringer, M.N., et al., *No reduction in cerebral metabolism as a result of early moderate hyperventilation following severe traumatic brain injury.* Journal of Neurosurgery, 2000. **92**(1): p. 7-13.

174. Adamczak, J.M., et al., *High field BOLD response to forepaw stimulation in the mouse.* Neuroimage. **51**(2): p. 704-12.

175. Saria, A. and J.M. Lundberg, *Evans Blue Fluorescence - Quantitative and Morphological Evaluation of Vascular-Permeability in Animal-Tissues.* Journal of Neuroscience Methods, 1983. **8**(1): p. 41-49.